

# Dynamical Model of An Oscillating Shelled Microbubble

James Cowley<sup>1</sup>, Anthony J. Mulholland<sup>1</sup>, Iain W. Stewart<sup>1</sup> &  
Anthony Gachagan<sup>2</sup>

<sup>1</sup>Department of Mathematics and Statistics,  
University of Strathclyde,  
26 Richmond Street,  
Glasgow, G1 1XH.

<sup>2</sup>The Centre for Ultrasonic Engineering,  
Department of Electronic and Electrical Engineering,  
University of Strathclyde,  
204 George Street,  
Glasgow, G1 1XH.

## **Abstract**

There is considerable interest at the moment on using shelled microbubbles as a transportation mechanism for localised drug delivery, specifically in the treatment of various cancers. In this report a theoretical model is proposed which predicts the dynamics of an oscillating shelled microbubble. A neo-Hookean, compressible strain energy density function is used to

model the potential energy per unit volume of the shell. The shell is then stressed by applying a series of small radially directed stress steps to the inner surface of the shell whilst setting the outer surface's stress to zero. The spatial profiles of the Cauchy radial and angular (hoop) stresses that are created within the shell during this quasistatic inflationary process are then stored as the shelled microbubble is inflated. The shelled microbubble is then allowed to collapse by setting the stress at the inner surface to zero. The model which results is then used to predict the dynamics of the shelled microbubble as it oscillates about its equilibrium state. A linear approximation is then used to allow analytical insight into both the quasistatic inflationary and oscillating phases of the shelled microbubble. Numerical results from the full nonlinear model are produced which show the influence of the shell's thickness, Poisson ratio and shear modulus on the rate of oscillation of the shelled microbubble and these are compared to the approximate analytical solution. The theoretical model's collapse time is compared to published experimental results.

## Contents

<b>1</b>	<b>Introduction</b>	<b>4</b>
<b>2</b>	<b>The analysis of the collapse of a shelled microbubble</b>	<b>10</b>
<b>3</b>	<b>Stressing a shelled microbubble</b>	<b>11</b>
3.1	Defining the coordinate frames . . . . .	11
3.2	Tensor theory and vector fields . . . . .	13
3.3	The gradient and divergence of a tensor . . . . .	17
3.4	Calculating the grad of the deformation . . . . .	18

3.5	Defining the appropriate strain energy density function . . . . .	21
3.6	Calculating the divergence of the First Piola Kirchoff stress tensor .	24
3.7	Formulating the Cauchy stresses for the radial equation . . . . .	27
<b>4</b>	<b>Nondimensionalising the Quasistatic and collapse phases</b>	<b>30</b>
<b>5</b>	<b>Linearisation of the inflationary process</b>	<b>32</b>
<b>6</b>	<b>Linearisation of the time evolving collapse phase of the shell</b>	<b>37</b>
<b>7</b>	<b>Results for the inflationary phase of the shelled microbubble</b>	<b>46</b>
<b>8</b>	<b>Results for the collapse phase of the shelled microbubble</b>	<b>53</b>
<b>9</b>	<b>Conclusion</b>	<b>59</b>
<b>10</b>	<b>Numerical analysis of the collapse of a shelled microbubble</b>	<b>60</b>
<b>11</b>	<b>Methodology</b>	<b>60</b>
11.1	Forward picture - Inflating the sphere . . . . .	60
11.2	Collapsing the shell of the microbubble . . . . .	62
<b>12</b>	<b>Results and Discussion</b>	<b>66</b>
12.1	Inflation of the shelled microbubble . . . . .	67
12.2	Collapsing the shell . . . . .	84
<b>13</b>	<b>Experimental v theoretical results</b>	<b>102</b>
13.1	Conclusion . . . . .	103

# 1 Introduction

Premanufactured shelled microbubbles are currently licensed in the UK as ultrasound imaging contrast agents [1]. Current research is focussing on using the microbubbles as a transportation mechanism for localised drug delivery specifically in the treatment of various cancers [2, 3, 4, 5, 6, 7]. Ultrasound contrast agents (UCAs) are shelled microbubbles typically composed of a layer or several layers of a protein shell encapsulating a perfluoro gas that helps to stabilise the microbubble when it is injected into the bloodstream [8, 9, 10]. The shelled microbubbles have a typical radius of between 1 and 4  $\mu\text{m}$  allowing them to propagate through the capillaries in the human body and a shell thickness that varies between 4 and 100 nm depending on whether the UCA is a monolipid or polymer variant [11]. A typical shear modulus value for a monolipid UCA is 20MPa with a Poisson ratio of  $\nu = 0.48$  [12, 13]. UCAs resonate with typical frequencies in the range of 1 to 10 MHz producing nonlinear, multiple harmonic signals that enhance the quality of the medical imaging process [14]. There has been a research momentum growing in recent years to use the UCAs as localised drug delivery agents [15]. The outer shell of the microbubbles will be coated with chemical receptors which act as a targeting mechanism for cancerous tumours and encapsulated within the shell will be cancer treating drugs [16]. The practitioners have laid out a vision wherein will be microbubbles injected into the bloodstream where the blood pressure and the blood flow will pump them around the body [17]. The region of the body which possesses the tumour is then subjected to ultrasound chirps typically in the range of 3 - 7 MHz [11]. Acoustic microstreaming generated by shelled microbubbles near the cellular walls will result in the formation of cavitation bubbles that collapse rapidly to produce shock waves that create pores in the capillary walls. This enhancement of the porosity of the capillaries is known as sonoporation [18]. The

pores provide a doorway to the surface of the tumour where the chemical receptors will guide the shelled microbubbles onto the surface of the tumour where will be burst by a further high power ultrasound pulse in a controlled and highly localised manner. This procedure aims to minimise the pernicious side effects associated with current conventional chemotherapy treatments. It is worth emphasising that there are competitor technologies being proposed and, for example, some studies have focussed on exploiting the photothermal properties of gold and silver coated bubbles to kill the cancer cells [19]. At present the mathematical modelling behind sonoporation is still in its infancy with only a handful of articles attempting to quantify the physical mechanisms behind sonoporation [20, 21]. In vitro experiments performed on phantoms have shown that high frequency chirps significantly enhance the sonoporation procedure when used along with shelled microbubbles [22, 23, 18, 24, 11, 4]. This is because the microbubble populations have a spread of radii and therefore a distribution of resonant frequencies. Since maximum sonoporation will occur when each microbubble shears against the capillary wall at its resonance, then it is no surprise that the chirp containing a range of frequencies performs better. Fundamental to the sonoporation efficiency is the material parameters of the shell which can include the thickness of the shell, its stiffness (shear modulus) and its Poisson ratio. Much progress has been made but much remains to be done before this can be deployed routinely in patients [25]. Hence there is a need to develop virtual simulation tools to better understand the challenges [26]. This report contributes to this effort by identifying how the material parameters of the shell influence the dynamics and collapse time of the shell.

Most current shelled microbubble models are based on the Rayleigh-Plesset equation for a free gas bubble, which is derived by applying pressure balances to the

inner surface of the shelled microbubble with those acting on the outside of the shelled bubble's surface and the surrounding liquid. The Rayleigh-Plesset equation assumes that the bubble oscillations are purely radial and that the surrounding liquid is incompressible [27, 28]. The gas in the shelled bubble is assumed to behave adiabatically despite its polytropic index being relatively close to one which is associated with isothermal behaviour [29]. The damping contributors are the liquid viscosity that surrounds the bubble, thermal damping between the gas and the surrounding liquid, and damping associated with liquid compressibility via the external acoustic energy. The thermal damping can be accounted for by selecting the appropriate value for the polytropic index,  $\kappa$  [29]. The Rayleigh-Plesset equation can be modified to take account of the compressible nature of the surrounding liquid [29]. There are then two approaches to modelling shelled microbubbles based on this model. The first approach is empirical and incorporates additional terms into the Rayleigh-Plesset equation determined purely on the basis of experimental observations. The second and more rigorous approach is to derive the stresses and viscosities associated with the shell from first principles. Marmottant et al followed the former approach and modelled lipid shelled microbubbles using a Rayleigh-Plesset equation [30]. which assumes that when the bubble oscillates, the elastic region holds only for a small range of radii. However this model is capable of describing nonlinear effects particularly the compression only behaviour observed in the analysis of certain monolipid shelled microbubbles [30]. This work was the first to propose a model for the surface tension of the shell which varies during various stages of its oscillatory motion. They achieved this by expressing the surface tension as a piecewise function dependent on the shell's area density with the shell experiencing a smaller surface tension during contraction. This is due to the area per molecule decreasing during contraction resulting in a

smaller number of molecular interactions and therefore a smaller surface tension. Paul et al also used empirical means to develop a Rayleigh-Plesset model using an effective surface tension that incorporated a dilatational elasticity term which was a function of the surface area change [31]. The dilatational elasticity term was modelled using both quadratic and exponential terms with each approach giving similar results and predicting the subharmonic response with a reasonable level of accuracy. Both of these approaches are empirical in nature and rely heavily on experimental observations for one particular type of UCA. Church followed the second approach and developed a model for an encapsulated shelled bubble incorporating both the inner and outer radii and the interfacial surface tension [32]. This approach was developed from first principles rather than by exploiting an empirical based methodology. Church assumed that the incompressible spherical encapsulated gas bubble was surrounded by an unbounded incompressible liquid and experienced radial oscillations when it was subjected to an external acoustic pressure. Church's model uses two surface tension expressions; a surface tension for the outer shell/liquid interface and an interfacial surface tension between the shell's inner radius and the gas layer. Church exploited the Rayleigh-Plesset equation and assumed that the shell material behaved as a viscoelastic solid obeying the Kelvin-Voigt constitutive equation [32]. Experimental evidence indicates that the Church model is more suited to albumin shelled bubbles with shell thicknesses of the order of 15 to 20 nm [29].

Doinikov and Dayton suggested a first principles model model for lipid encapsulated bubbles where the shell is treated as a viscoelastic fluid that obeys the Maxwell constitutive equation [33]. The Maxwell model developed by them helped to explain some of the experimental data that contradicted previous assumptions

that the lipid shell behaves as a viscoelastic solid. The Maxwell model predicts that the resonance frequency of a bubble possessing a viscoelastic fluid shell can have both higher and lower resonance frequencies than that of a free bubble. This depends on the choice of the shell parameters [29, 33].

Doinikov et al proposed a modification to their model where the shell's viscous constant was replaced by a function of the shell's shear rate [34]. They introduced this approach to attempt to solve the dependency of the shell viscosity on the initial bubble's radius [33]. Despite numerous Rayleigh-Plesset models existing for UCAs, experimental observations have been made that challenge the current, existing models. The experimental observations of compression only behaviour for monolipid coated UCAs is highlighted by the asymmetrical oscillation curves that are experimentally observed and that were subsequently modelled empirically by Marmottant who separated the shell elastic behaviour into three different regions [30]. According to current models, the shell's material parameters such as viscosity and elasticity, display a dependency on the initial radius of the bubble. However, large bubbles possess a greater mass and surface area yet should still have the same viscosity and elasticity for the same type of material. This highlights a current flaw in the modelling of the rheological properties of monolipid UCAs which clearly requires a more fundamental and mathematically rigorous treatment [29].

There currently exists very little literature pertaining specifically to UCA modelling using nonlinear elasticity; which is the standard approach for modelling large deformations of elastic materials and in particular soft materials such as in biological settings [35, 36, 37, 38, 39, 40]. There are however, numerous publications relating to the dynamics of spherical bodies using nonlinear elasticity [41]. A recent



paper by Efthymium and Tsigliffis uses constitutive laws from nonlinear elasticity alongside the Kelvin-Voigt viscoelastic model to study the physical behaviour of various UCA types ranging from monolipids to polymers [42]. They reported that the polymer based UCAs were consistent with the neo-Hookean model whereas monolipid UCAs were consistent with the Mooney-Rivlin constitutive law due to the presence of strain softening behaviour. Strain softening behaviour occurs due to the area density of the monolipid decreasing as the material stretches radially outwards. This behaviour has been observed in monolipids typically used in UCA shells such as Sonovue [29, 43].

This report will focus on the use of a nonlinear elasticity model of a UCA to explore the role that the shell material properties and stress have on the UCA's dynamics. The stress will be calculated by using a compressible strain energy density function and by applying a series of stress steps at the inner surface of the shell from an initial reference configuration (stress free). The spatial profiles for the Cauchy radial and hoop stresses will be used along with the conservation of mass and energy to model the subsequent collapse of the shelled microbubble when a stress free boundary condition is instantaneously applied to the inner surface. The nonlinear dynamical equations are then linearised to enable some analytical insight. This leads to a simple harmonic motion description of the bubble dynamics where the relaxation time can be expressed in terms of the material parameters. These material parameters are then adjusted to determine their influence on the time taken for the stressed shell to collapse back to its stress free equilibrium position.

## 2 The analysis of the collapse of a shelled microbubble

In this section a theoretical model is proposed to predict the dynamics of an oscillating shelled microbubble. A compressible, neo-Hookean [35] strain energy density function is used to model the potential energy per unit volume of the shell. A stress is applied to the shell by applying a series of radially directed small stress steps to the inner surface of the shell and setting the outer surface's stress normal to the surface to zero. This stressing process is quasistatic and is thus independent of both time. The spatial profiles of the Cauchy radial and angular (hoop) stresses that are created within the shell during this process are evaluated using an asymptotic expansion. A stress is applied to inflate the shell commensurate with typical values used in sonoporation and works out to be around 1% of the stiffness of a 20MPa shell [18, 44]. This small stress load facilitates the use of an asymptotic expansion. Once the commensurate radial displacement is reached, the stress load at the inner radius is switched off causing the shell to collapse and oscillate about its equilibrium (stress free) position. It is assumed that the switching off of the stress load at the inner radius neither adds to or subtracts from the total potential energy of the shell, namely that there is no external impulse applied by the switching off procedure. The inflated value is used as an initial condition to model the time evolving collapse phase of the shell. The radial and hoop stresses acting on the shell are made compressive in nature order thus providing the restoring force necessary to cause the shell to collapse. The collapse phase is modelled by applying the conservation of energy and mass alongside an asymptotic expansion to predict the dynamics of the collapsing, oscillating shelled microbubble. Results are produced from the model to show the influence of the

shell's thickness, its Poisson ratio and the shear modulus on the collapse times of the oscillating shell.

### 3 Stressing a shelled microbubble

#### 3.1 Defining the coordinate frames

Consider the reference configuration of a stress free, fully formed spherical shell with an inner and outer radii of  $R_I$  and  $R_O$  respectively ([45],p63). Figure 1 illustrates such a scenario.

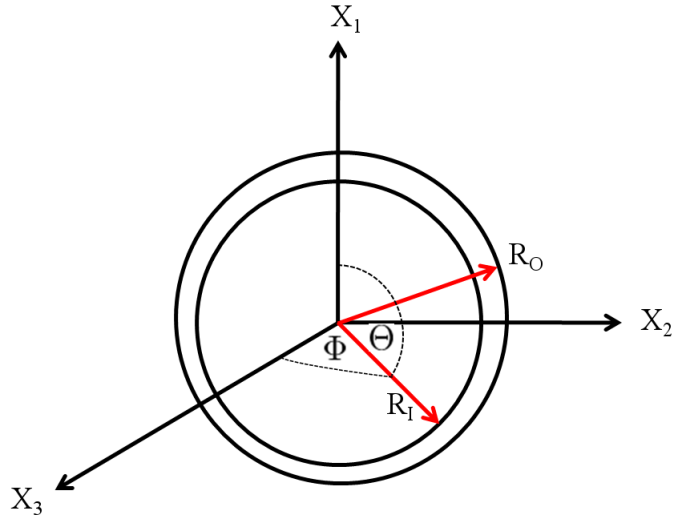


Figure 1: Reference configuration for a stress free spherical shell.

The reference configuration of the system is a spherical shell possessing no stress. A spherical polar coordinate system with coordinates  $(X^1, X^2, X^3) = (R, \Theta, \Phi)$  has the coordinate transformation (cartesian coordinates)  $(X_1, X_2, X_3) = (R \sin \Theta \cos \Phi, R \sin \Theta \sin \Phi, R \cos \Theta)$ . The reference configuration basis vectors  $e_R, e_\Theta$  and  $e_\Phi$  can be written in terms of the Cartesian basis vectors  $e_1, e_2, e_3$

to give

$$e_R = \sin \Theta \cos \Phi e_1 + \sin \Theta \sin \Phi e_2 + \cos \Theta e_3, \quad (1)$$

$$e_\Theta = \cos \Theta \cos \Phi e_1 + \cos \Theta \sin \Phi e_2 - \sin \Theta e_3, \text{ and} \quad (2)$$

$$e_\Phi = -\sin \Phi e_1 + \cos \Phi e_2. \quad (3)$$

The following relationships for the basis vectors hold

$$\frac{\partial e_R}{\partial \Theta} = \cos \Theta \cos \Phi e_1 + \cos \Theta \sin \Phi e_2 - \sin \Theta e_3 = e_\Theta, \quad (4)$$

$$\frac{\partial e_R}{\partial \Phi} = -\sin \Theta \sin \Phi e_1 + \sin \Theta \cos \Phi e_2 = \sin \Theta e_\Phi, \quad (5)$$

$$\frac{\partial e_\Theta}{\partial \Theta} = -\sin \Theta \cos \Phi e_1 - \sin \Theta \sin \Phi e_2 - \cos \Theta e_3 = -e_R, \quad (6)$$

$$\frac{\partial e_\Theta}{\partial \Phi} = -\cos \Theta \sin \Phi e_1 + \cos \Theta \cos \Phi e_2 = \cos \Theta e_\Phi, \quad (7)$$

$$\frac{\partial e_\Phi}{\partial \Theta} = 0, \text{ and} \quad (8)$$

$$\frac{\partial e_\Phi}{\partial \Phi} = -\cos \Phi e_1 - \sin \Phi e_2 = -\sin \Theta e_R - \cos \Theta e_\Theta. \quad (9)$$

The current configuration is an inflated spherical shell possessing a stress. Let the current configuration basis vectors be represented by  $e_r$ ,  $e_\theta$  and  $e_\phi$  where  $e_1$ ,  $e_2$  and  $e_3$  are the standard Cartesian basis vectors, and so

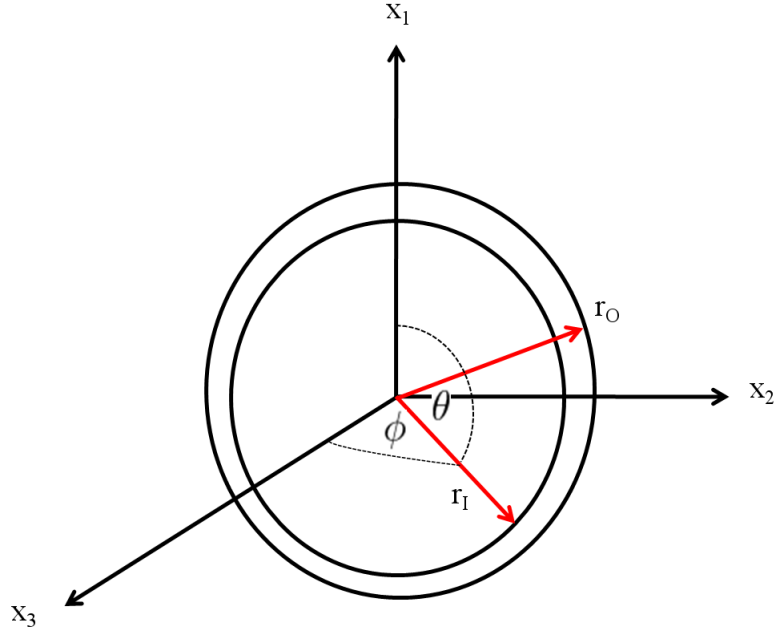


Figure 2: Current configuration for a stressed spherical shell.

$$e_r = \sin \theta \cos \phi e_1 + \sin \theta \sin \phi e_2 + \cos \theta e_3, \quad (10)$$

$$e_\theta = \cos \theta \cos \phi e_1 + \cos \theta \sin \phi e_2 - \sin \theta e_3, \text{ and} \quad (11)$$

$$e_\phi = -\sin \phi e_1 + \cos \phi e_2. \quad (12)$$

### 3.2 Tensor theory and vector fields

Consider the following discussion from Ogden ([45],p55) regarding curvilinear coordinates. Let  $\psi : \mathcal{D} \rightarrow \mathbb{R}^3$  represent a one-to-one continuous mapping whose inverse  $\psi^{-1}$  is also continuous. If  $x \in \mathcal{D}$  then

$$\psi(x) = (x^1, x^2, x^3), \text{ and } x = \psi^{-1}(x^1, x^2, x^3). \quad (13)$$

Assuming that  $\psi$  and  $\psi^{-1}$  have continuous derivatives up to infinity, given  $\psi$  and  $\mathcal{D}$ , there are three scalar fields  $\psi^i : \mathcal{D} \rightarrow \mathbb{R}$ , such that

$$\psi(x) = (\psi^1(x), \psi^2(x), \psi^3(x)), \quad x \in \mathcal{D}. \quad (14)$$

The fields  $\psi^i$  are the coordinate functions of  $\psi$  on  $\mathcal{D}$ ,  $\psi$  is a coordinate system on  $\mathcal{D}$  which is a coordinate neighbourhood. The coordinates of  $x^i$  of the point  $x$  in the coordinate system  $\psi$  are given by

$$x^i = \psi^i(x). \quad (15)$$

They are called the curvilinear coordinates covering  $\mathcal{D}$  where  $x^i$  represents the curvilinear coordinates and  $x_i$  denote the Cartesian coordinates [45]. Equation (15) can be used to define a subset of  $\mathcal{D}$  called an  $x^i$ -coordinate surface of  $\psi$  in  $\mathcal{D}$  such that

$$x^i \equiv \psi^i(x) = \text{constant}. \quad (16)$$

The natural basis of  $\psi$  at  $x$  is written as

$$g_i(x) = \frac{\partial x}{\partial x^i} \quad (i = 1, 2, 3), \quad (17)$$

where  $g_i$  is a vector field on  $\mathcal{D}$  and  $g_i$  is a tangent to the  $x^i$ -coordinate curve of  $\psi$ .

A reciprocal basis  $g^i$  of  $g_i$  at each point  $x$  of  $\mathcal{D}$  may be defined such that

$$g^i(x) \cdot g_j(x) = \delta_j^i \quad (18)$$

and where  $\{g_i\}_{i \in \{1,2,3\}}$  represents a fixed set of general basis vectors whose elements are assumed to be non-zero and non-parallel to each other. The general basis

vectors are linearly independent [39]. The reciprocal general basis vectors are defined as

$$g^i(x) = \text{grad } \psi^i(x). \quad (19)$$

From (18)

$$\mathbf{I} = g^i(x) \otimes g_i(x) = g_i(x) \otimes g^i(x), \quad (20)$$

for each  $x$  in  $\mathcal{D}$ . The contravariant and covariant components of  $I$  are denoted by  $g^{ij}(x)$  and  $g_{ij}(x)$  respectively, where

$$\begin{aligned} g^{ij}(x) &= g^i(x) \cdot g^j(x), & g_{ij}(x) &= g_i(x) \cdot g_j(x), \\ g^i(x) &= g^{ij}(x) \cdot g_j(x), & g_i(x) &= g_{ij}(x) \cdot g^j(x), \end{aligned} \quad (21)$$

and the mixed components are  $\delta_j^i$ . From equation (17)

$$\frac{\partial g_i(x)}{\partial x^j} = \frac{\partial^2 x}{\partial x^i \partial x^j} = \frac{\partial g_j}{\partial x^i}. \quad (22)$$

To distinguish between the reference and current vector fields, we employ an uppercase ( $G$ ) for the reference configuration and a lowercase ( $g$ ) for the current configuration. Using equations (17) and (18), the vector fields for the reference

configuration are

$$G_1 = e_R, \quad (23)$$

$$G^1 = e_R, \quad (24)$$

$$G_2 = R \cos \Theta \cos \Phi e_1 + R \cos \Theta \sin \Phi e_2 - R \sin \Theta e_3 = R e_\Theta, \quad (25)$$

$$G^2 = \frac{1}{R} e_\Theta, \quad (26)$$

$$G_3 = -R \sin \Theta \sin \Phi e_1 + R \sin \Theta \cos \Phi e_2 = R \sin \Theta e_\Phi, \text{ and} \quad (27)$$

$$G^3 = \frac{1}{R \sin \Theta} e_\Phi. \quad (28)$$

Similarly, for the current configuration

$$g_1 = e_r, \quad (29)$$

$$g^1 = e_r, \quad (30)$$

$$g_2 = r \cos \theta \cos \phi e_1 + r \cos \theta \sin \phi e_2 - r \sin \theta e_3 = r e_\theta, \quad (31)$$

$$g^2 = \frac{1}{r} e_\theta, \quad (32)$$

$$g_3 = -r \sin \theta \sin \phi e_1 + r \sin \theta \cos \phi e_2 = r \sin \theta e_\phi, \text{ and} \quad (33)$$

$$g^3 = \frac{1}{r \sin \theta} e_\phi. \quad (34)$$

Using the identities from equation (21) the reference and current configurations can be written as

$$G_{ij} = \begin{pmatrix} 1 & 0 & 0 \\ 0 & R^2 & 0 \\ 0 & 0 & R^2 \sin^2 \Theta \end{pmatrix},$$

and



$$g_{ij} = \begin{pmatrix} 1 & 0 & 0 \\ 0 & r^2 & 0 \\ 0 & 0 & r^2 \sin^2 \theta \end{pmatrix}.$$

The  $g_{ij}$  and  $g^{ij}$  are commonly referred to as the metric coefficients and determine the geometrical characteristics of a given basis [39].

### 3.3 The gradient and divergence of a tensor

For a tensor field  $T$  of order  $n$ ,  $\text{grad } T$  is written as  $\nabla \otimes T$  and represents a tensor field of order  $n + 1$ . If  $v$  is a vector field, the scalar field  $\nabla \cdot v$  (the divergence of  $v$ ), is defined as

$$\text{div } v \equiv \nabla \cdot v = \text{tr}(\nabla \otimes v), \quad (35)$$

where  $\text{tr}$  represents the trace which is defined as the sum  $(\nabla \otimes v)_{ii}$ . The divergence operation is the contraction of the second order tensor field  $\nabla \otimes v$ .

Consider the vector field  $v$ , then

$$\text{grad } v(x) \equiv \nabla \otimes v(x) = \frac{\partial v(x)}{\partial x_j} \otimes e_j, \quad (36)$$

where  $v = v_i e_i$ . Contraction of equation (36) gives the component expression for  $\text{div } v$ . Hence

$$\nabla \cdot v(x) = \frac{\partial v_i(x)}{\partial x_i}. \quad (37)$$

For a vector field  $v$  where  $v = v_k g^k$  then it follows that ([45], p65)

$$\nabla \otimes v = \left( \frac{\partial v_k}{\partial x^j} - \Gamma_{kj}^i v_i \right) g^k \otimes g^j, \quad (38)$$

(note that  $\Gamma_{kj}^i = \Gamma_{jk}^i$ ) where ([45], p58)

$$\Gamma_{kj}^i = -g_k \cdot \frac{\partial g^i}{\partial x^j} \quad (39)$$

For a tensor field  $T$  of order  $n$ , equation (36) generalises to

$$\begin{aligned} \nabla \otimes T &= \frac{\partial T}{\partial x_i} \otimes e_i, \\ \nabla \otimes T &= \frac{\partial T_{i_1 i_2 \dots i_n}}{\partial x_i} \otimes e_{i_1} \otimes e_{i_2} \otimes \dots \otimes e_{i_n} \otimes e_i, \end{aligned} \quad (40)$$

where the components  $T_{i_1 i_2 \dots i_n}$  are scalar fields. For a second order tensor ([45], p65)

$$T = T_{ij} g^i \otimes g^j. \quad (41)$$

### 3.4 Calculating the grad of the deformation

The applied stress is due to a stress load that is applied to the interior surface of the microbubble's shell. The deformation gradient  $F$  is a two point tensor (mixed tensorial basis) with a deformation,  $\chi = \chi_i g^i$ , where the gradient of the deformation is defined as  $F = \nabla \otimes \chi$ , then from equations (38) and (39) we get

$$\begin{aligned} \nabla \otimes \chi &= \frac{\partial}{\partial X^j} (\chi_i g^i) \otimes G^j = \left( \frac{\partial \chi_i}{\partial X^j} g^i + \chi_i \frac{\partial g^i}{\partial X^j} \right) \otimes G^j, \\ &= \left( \frac{\partial \chi_i}{\partial X^j} g^i + \chi_n \frac{\partial g^n}{\partial X^j} \cdot g_i g^i \right) \otimes G^j, \\ &= \left( \frac{\partial \chi_i}{\partial X^j} + \chi_n \frac{\partial g^n}{\partial X^j} \cdot g_i \right) g^i \otimes G^j. \end{aligned} \quad (42)$$

Note that using a mixed tensorial basis requires abandoning the routine use of Christoffel symbols represented by  $\Gamma_{kj}^i$  illustrated in equation (39) and is instead represented by  $\partial g^n / \partial X^j$  as illustrated in equation (42). In spherical polar coordinates the current configuration can be transformed into physical components ([45],p64) to give  $\chi_1 g^1 = \chi_1 e_r = \chi_r e_r$  resulting in  $\chi_1 = \chi_r$ . The  $\chi_\theta$  term is  $\chi_2 g^2 = \chi_2 e_\theta / r = \chi_\theta e_\theta$  resulting in  $\chi_2 = r \chi_\theta$ . The  $\chi_\phi$  term is  $\chi_3 g^3 = \chi_3 e_\phi / (r \sin \theta) = \chi_\phi e_\phi$  where  $\chi_3 = r \sin \theta \chi_\phi$ . Using equation (42) we can determine the gradient of the deformation where the deformation is defined by  $\chi_1 = r(R)$ , and  $\chi_2 = \chi_3 = 0$ . Assuming  $\theta(\Theta) = \Theta$  and  $\phi(\Phi) = \Phi$ , the terms for equation (42) are

$$(\nabla \otimes \chi)_{11} = \left( \frac{\partial \chi_1}{\partial X^1} + \chi_1 \frac{\partial g^1}{\partial X^1} \cdot g_1 \right) g^1 \otimes G^1 = \left( \frac{\partial r}{\partial R} + r \frac{\partial e_r}{\partial R} \cdot e_r \right) e_r \otimes e_R = r' e_r \otimes e_R, \quad (43)$$

$$(\nabla \otimes \chi)_{12} = \left( \frac{\partial \chi_1}{\partial X^2} + \chi_1 \frac{\partial g^1}{\partial X^2} \cdot g_1 \right) g^1 \otimes G^2 = (r e_\theta \theta' \cdot e_r) \frac{e_r \otimes e_\theta}{R} = 0, \quad (44)$$

$$(\nabla \otimes \chi)_{13} = \left( \frac{\partial \chi_1}{\partial X^3} + \chi_1 \frac{\partial g^1}{\partial X^3} \cdot g_1 \right) g^1 \otimes G^3 = \left( r \frac{\partial e_r}{\partial \Phi} \cdot e_r \right) \frac{e_r \otimes e_\Phi}{R \sin \Phi} = (r \sin \theta e_\phi \phi' \cdot e_r) \frac{e_r \otimes e_\Phi}{R \sin \Theta} = 0, \quad (45)$$

$$(\nabla \otimes \chi)_{21} = \left( \frac{\partial \chi_2}{\partial X^1} + \chi_1 \frac{\partial g^1}{\partial X^1} \cdot g_2 \right) g^2 \otimes G^1 = \left( r \frac{\partial e_r}{\partial R} \cdot r e_\theta \right) \frac{e_\theta \otimes e_R}{r} = 0, \quad (46)$$

$$\begin{aligned}
(\nabla \otimes \chi)_{22} &= \left( \frac{\partial \chi_2}{\partial X^2} + \chi_1 \frac{\partial g^1}{\partial X^2} \cdot g_2 \right) g^2 \otimes G^2 = \left( \chi_1 \frac{\partial g^1}{\partial X^2} \cdot g_2 \right) \frac{e_\theta \otimes e_\Theta}{rR} \\
&= \left( r \frac{\partial e_r}{\partial \Theta} \cdot r e_\theta \right) \frac{e_\theta \otimes e_\Theta}{rR} = \left( \frac{r}{R} \theta' \right) e_\theta \otimes e_\Theta, \tag{47}
\end{aligned}$$

$$\begin{aligned}
(\nabla \otimes \chi)_{23} &= \left( \frac{\partial \chi_2}{\partial X^3} + \chi_1 \frac{\partial g^1}{\partial X^3} \cdot g_2 \right) g^2 \otimes G^3 = \left( r \frac{\partial e_r}{\partial \Phi} \cdot r e_\theta \right) \frac{e_\theta \otimes e_\Phi}{rR \sin \Theta} \\
&= (r \sin \theta e_\phi \phi' \cdot r e_\theta) \frac{e_\theta \otimes e_\Phi}{rR \sin \Theta} = 0, \tag{48}
\end{aligned}$$

$$\begin{aligned}
(\nabla \otimes \chi)_{31} &= \left( \frac{\partial \chi_3}{\partial X^1} + \chi_1 \frac{\partial g^1}{\partial X^1} \cdot g_3 \right) g^3 \otimes G^1 = \left( r \frac{\partial e_r}{\partial R} \cdot r \sin \theta e_\phi \right) \frac{e_\phi \otimes e_R}{r \sin \theta} = 0, \tag{49}
\end{aligned}$$

$$\begin{aligned}
(\nabla \otimes \chi)_{32} &= \left( \frac{\partial \chi_3}{\partial X^2} + \chi_1 \frac{\partial g^1}{\partial X^2} \cdot g_3 \right) g^3 \otimes G^2 = \left( r e_\theta \frac{\partial \theta}{\partial \Theta} \cdot r \sin \theta e_\phi \right) \frac{e_\phi \otimes e_\Theta}{rR \sin \theta} = 0, \text{ and} \tag{50}
\end{aligned}$$

$$\begin{aligned}
(\nabla \otimes \chi)_{33} &= \left( \frac{\partial \chi_3}{\partial X^3} + \chi_1 \frac{\partial g^1}{\partial X^3} \cdot g_3 \right) g^3 \otimes G^3 = \left( r \frac{\partial e_r}{\partial \Phi} \cdot r \sin \theta e_\phi \right) \frac{e_\phi \otimes e_\Phi}{rR \sin \theta \sin \Theta} \\
&= \left( \frac{r \sin \theta}{R \sin \Theta} \phi' \right) e_\phi \otimes e_\Phi. \tag{51}
\end{aligned}$$

The gradient of this deformation is a two point tensor, given by  $F = \nabla \otimes \chi$ , where

$$F = \begin{pmatrix} r' & 0 & 0 \\ 0 & \frac{r\theta'}{R} & 0 \\ 0 & 0 & \frac{r \sin \theta}{R \sin \Theta} \phi' \end{pmatrix}. \quad (52)$$

If  $\theta = \Theta$  and  $\phi = \Phi$ , then

$$F = \begin{pmatrix} r' & 0 & 0 \\ 0 & \frac{r}{R} & 0 \\ 0 & 0 & \frac{r}{R} \end{pmatrix}. \quad (53)$$

### 3.5 Defining the appropriate strain energy density function

If we assume that the shell material is hyperelastic then there exists a strain energy density function expressing the potential energy per unit volume. The strain energy density function that will be used here to model the microbubble shell is a neo-Hookean strain energy density function [39, 35, 46],  $W(F)$ , which includes a compressible term that is used to model the change in volume of the shell of the microbubble as it is inflated. The determinant of the gradient of the deformation of  $F$ , gives a measure of how the volume of the spherical shell changes as it maps from the stress free, reference configuration to the stressed, current configuration. The determinant is denoted by

$$J = \frac{r' r^2}{R^2}. \quad (54)$$

The Neo-Hookean strain energy density function is ([35], equation(5)), where

$$W(F) = \frac{\mu}{2} (\text{tr}(FF^T) - 3) + \frac{\mu}{2\beta} (J^{-2\beta} - 1), \quad (55)$$

and  $FF^T$  is defined as the left Cauchy-Green deformation tensor ([39],p81),  $\mu$  is the shear modulus,  $\nu$  is Poisson's ratio and  $\beta = \nu/(1 - 2\nu)$ . Consider the following trace properties

$$\begin{aligned}
\frac{\partial}{\partial F_{mn}} (\det F) &= \frac{\partial}{\partial F_{mn}} \left( \frac{1}{6} \epsilon_{ijk} \epsilon_{pqr} F_{ip} F_{jq} F_{kr} \right), \\
&= \frac{1}{6} \epsilon_{ijk} \epsilon_{pqr} (\delta_{im} \delta_{pn} F_{jq} F_{kr} + F_{ip} \delta_{jm} \delta_{qn} F_{kr} + F_{ip} F_{jq} \delta_{km} \delta_{rn}), \\
&= \frac{1}{6} (\epsilon_{mjk} \epsilon_{nqr} F_{jq} F_{kr} + \epsilon_{imk} \epsilon_{pnr} F_{ip} F_{kr} + \epsilon_{ijm} \epsilon_{pqn} F_{ip} F_{jq}), \\
&= \frac{1}{6} (\epsilon_{mjk} \epsilon_{nqr} F_{jq} F_{kr} + \epsilon_{mik} \epsilon_{npr} F_{ip} F_{kr} + \epsilon_{mij} \epsilon_{npq} F_{ip} F_{jq}), \\
&= \frac{1}{2} \epsilon_{mjk} \epsilon_{nqr} F_{jq} F_{kr},
\end{aligned} \tag{56}$$

and premultiplying equation (56) by  $F_{pn}$  leads to

$$\begin{aligned}
F_{pn} \frac{\partial}{\partial F_{mn}} (\det F) &= \frac{1}{2} \epsilon_{mjk} \epsilon_{nqr} F_{pn} F_{jq} F_{kr}, \\
&= \frac{1}{2} \epsilon_{mjk} (\det F) \epsilon_{pjk}, \\
&= \frac{1}{2} \epsilon_{mjk} \epsilon_{pjk} (\det F), \\
&= \frac{1}{2} (2\delta_{mp}) (\det F), \\
&= (\det F) \delta_{mp}.
\end{aligned} \tag{57}$$

Multiplying equation (57) through by  $(F^{-1})_{qp}$  results in

$$\begin{aligned}
\delta_{qn} \frac{\partial}{\partial F_{mn}} (\det F) &= (\det F) (F^{-1})_{qm}, \\
\frac{\partial}{\partial F_{mq}} (\det F) &= (\det F) (F^{-1})_{qm},
\end{aligned} \tag{58}$$

and so the following can be shown to be true

$$\frac{\partial J}{\partial F} = |F|(F^{-1})^T = JF^{-T}. \quad (59)$$

Similarly for the trace where  $\text{tr}(FF^T) = (FF^T)_{ii} = F_{ij}F_{ji}$ , the derivative with respect to  $F$  gives

$$\frac{\partial}{\partial F_{ij}} (F_{ij}F_{ji}) = 2F_{ij}, \quad (60)$$

where

$$\frac{\partial(\text{tr}(FF^T))}{\partial F} = 2F. \quad (61)$$

The stresses can be described using the first Piola-Kirchhoff stress tensor which is the transpose of the nominal stress tensor, relating the force in the current configuration to the area in the reference configuration [35]. The Cauchy stresses relate the force in the current configuration to the area in the current configuration. The first Piola-Kirchhoff stress tensor,  $S(F)$ , is given using equation (59) and equation (61) along with equation (55), to give ([35], equation(5)),

$$\begin{aligned} S(F) &= \frac{\partial W}{\partial F} = \frac{\mu}{2} (2F) + \frac{\mu}{2\beta} \left( -2\beta J^{-2\beta-1} \frac{\partial J}{\partial F} \right) \\ &= \mu \left( -J^{-2\beta} F^{-T} + F \right). \end{aligned} \quad (62)$$

Substituting equation (53) into equation (62) gives

$$\begin{aligned} S &= \mu \left( -J^{-2\beta} \frac{1}{r'} + r' \right) e_r \otimes e_R + \mu \left( -J^{-2\beta} \frac{R}{r} + \frac{r}{R} \right) e_\theta \otimes e_\Theta \\ &\quad + \mu \left( -J^{-2\beta} \frac{R}{r} + \frac{r}{R} \right) e_\phi \otimes e_\Phi. \end{aligned} \quad (63)$$

### 3.6 Calculating the divergence of the First Piola Kirchoff stress tensor

The author is unaware of any published formal derivation of the divergence of the First Piola Kirchoff stress tensor for a sphere. For the static solution of a stressed sphere the divergence of the first Piola-Kirchhoff stress tensor will be equal to zero. To determine  $\nabla \cdot S = 0$ , we need to be able to relate the physical coordinates for the mixed tensorial basis to the general basis vectors represented by the components  $g_i$  and  $G_i$  where  $i \in \{1, 2, 3\}$ . The first Piola-Kirchhoff stress tensor is represented by [[45],p34],  $S = S_i^j g^i \otimes G_j$  where  $S_i^j$  are the left-covariant components of  $S$ . Converting into physical coordinates using equations (4) to (28) and equations (29) to (34)

$$S_1^1 g^1 \otimes G_1 = S_1^1 e_r \otimes e_R = S_{rR} e_r \otimes e_R,$$

and

$$S_1^1 = S_{rR} = \mu \left( -J^{-2\beta} \frac{1}{r'} + r' \right), \quad (64)$$

$$S_2^2 g^2 \otimes G_2 = S_2^2 \frac{R}{r} e_\theta \otimes e_\Theta = S_{\theta\Theta} e_\theta \otimes e_\Theta,$$

thus

$$S_2^2 = \frac{r}{R} S_{\theta\Theta} = \mu \left( -J^{-2\beta} + \frac{r^2}{R^2} \right), \quad (65)$$

and

$$S_3^3 g^3 \otimes G_3 = S_3^3 \frac{e_\phi}{r \sin \theta} \otimes R \sin \Theta e_\Phi = S_{\phi\Phi} e_\phi \otimes e_\Phi,$$



where  $\theta = \Theta$ , results in

$$S_3^3 = \frac{r}{R} S_{\phi\Phi} = \mu \left( -J^{-2\beta} + \frac{r^2}{R^2} \right). \quad (66)$$

Calculating the divergence of  $S$  using equations (38), (39) and (41) results in

$$\nabla \cdot S = \frac{\partial}{\partial X^k} (S_i^j g^i \otimes G_j) \cdot G^k. \quad (67)$$

Only  $S_1^1, S_2^2$  and  $S_3^3$  need to be evaluated because the off-diagonal elements such as  $S_1^2$  are all equal to zero. Calculating each of the terms in  $\nabla \cdot S$  using equation (67) and equations (23) to (34), gives

$$\frac{\partial}{\partial X^1} (S_1^1 g^1 \otimes G_1) \cdot G^1 = \frac{\partial S_1^1}{\partial R} (e_r \otimes e_R) \cdot e_R = \frac{\partial S_1^1}{\partial R} e_r. \quad (68)$$

Similarly we get

$$\begin{aligned} \frac{\partial}{\partial X^1} (S_2^2 g^2 \otimes G_2) \cdot G^1 &= \frac{\partial}{\partial R} \left( S_2^2 \frac{e_\theta}{r} \otimes R e_\Theta \right) \cdot e_R \\ &= \frac{\partial}{\partial R} \left( S_2^2 \frac{R}{r} \right) (e_\theta \otimes e_\Theta) \cdot e_R = 0, \end{aligned} \quad (69)$$

since  $(e_\theta \otimes e_\Theta) \cdot e_R = 0$  and both  $e_\theta$  and  $e_\Theta$  have no dependency on  $R$ . The following gives

$$\begin{aligned} \frac{\partial}{\partial X^1} (S_3^3 g^3 \otimes G_3) \cdot G^1 &= \frac{\partial}{\partial R} \left( S_3^3 \frac{e_\phi}{r \sin \theta} \otimes R \sin \Theta e_\Phi \right) \cdot e_R \\ &= \frac{\partial}{\partial R} \left( S_3^3 \frac{R \sin \Theta}{r \sin \theta} \right) (e_\phi \otimes e_\Phi) \cdot e_R = 0, \end{aligned} \quad (70)$$

since  $(e_\phi \otimes e_\Phi) \cdot e_R = 0$  and both  $e_\phi$  and  $e_\Phi$  have no dependency on  $R$ . Additionally

$$\frac{\partial}{\partial X^2} (S_2^2 g^2 \otimes G_2) \cdot G^2 = \frac{\partial}{\partial \Theta} \left( S_2^2 \frac{e_\theta}{r} \otimes R e_\Theta \right) \cdot \frac{e_\Theta}{R} = \frac{S_2^2}{r} \frac{\partial}{\partial \Theta} (e_\theta \otimes e_\Theta) \cdot e_\Theta$$

$$= \frac{S_2^2}{r} \left( \frac{\partial e_\theta}{\partial \Theta} \otimes e_\Theta + e_\theta \otimes \frac{\partial e_\Theta}{\partial \Theta} \right) \cdot e_\Theta = \frac{S_2^2}{r} \left( \frac{\partial e_\theta}{\partial \theta} \theta' \otimes e_\Theta \right) \cdot e_\Theta = -\frac{S_2^2}{r} e_r, \quad (71)$$

since  $\theta' = 1$  and  $S_2^2$  depends solely on  $r, r'$  and  $R$ . Similarly

$$\begin{aligned} \frac{\partial}{\partial X^2} (S_1^1 g^1 \otimes G_1) \cdot G^2 &= \frac{\partial}{\partial \Theta} (S_1^1 e_r \otimes e_R) \cdot \frac{e_\Theta}{R} \\ &= \frac{S_1^1}{R} (\theta' e_\theta \otimes e_R + e_r \otimes e_\Theta) \cdot e_\Theta = \frac{S_1^1}{R} (e_r \otimes e_\Theta) \cdot e_\Theta = \frac{S_1^1}{R} e_r, \end{aligned} \quad (72)$$

since  $(e_\theta \otimes e_R) \cdot e_\Theta = 0$ . The following gives

$$\begin{aligned} \frac{\partial}{\partial X^2} (S_3^3 g^3 \otimes G_3) \cdot G^2 &= \frac{\partial}{\partial \Theta} \left( S_3^3 e_\phi \otimes e_\Phi \frac{R \sin \Theta}{r \sin \theta} \right) \cdot \frac{e_\Theta}{R} \\ &= \frac{S_3^3}{R} \left( \frac{e_\phi}{\partial \Theta} \otimes e_\Phi \frac{\sin \Theta}{\sin \theta} + e_\phi \otimes \frac{\partial e_\Phi}{\partial \Theta} \left( \frac{\sin \Theta}{\sin \theta} \right) + e_\phi \otimes e_\Phi \frac{\partial}{\partial \Theta} \left( \frac{\sin \Theta}{\sin \theta} \right) \right) \cdot e_\Theta = 0, \end{aligned} \quad (73)$$

similarly

$$\begin{aligned} \frac{\partial}{\partial X^3} (S_1^1 g^1 \otimes G_1) \cdot G^3 &= \frac{\partial}{\partial \Phi} (S_1^1 e_r \otimes e_R) \cdot \frac{e_\Phi}{R \sin \Theta} = \frac{S_1^1}{R \sin \Theta} \left( \frac{\partial e_r}{\partial \Phi} \otimes e_R + e_r \otimes \frac{\partial e_R}{\partial \Phi} \right) \cdot e_\Phi \\ &= \frac{S_1^1}{R \sin \Theta} (\sin \theta \phi' e_\phi \otimes e_R + e_r \otimes \sin \Theta e_\Phi) \cdot e_\Phi = \frac{S_1^1}{R} (e_r \otimes e_\Phi) \cdot e_\Phi = \frac{S_1^1 e_r}{R}. \end{aligned} \quad (74)$$

Other terms are

$$\begin{aligned} \frac{\partial}{\partial X^3} (S_2^2 g^2 \otimes G_2) \cdot G^3 &= \frac{\partial}{\partial \Phi} \left( S_2^2 \frac{R}{r} e_\theta \otimes e_\Theta \right) \cdot \frac{e_\Phi}{R \sin \Theta} = \frac{S_2^2}{r \sin \Theta} \frac{\partial}{\partial \Phi} (e_\theta \otimes e_\Theta) \cdot e_\Phi \\ &= \frac{S_2^2}{r \sin \Theta} \left( \frac{\partial e_\theta}{\partial \Phi} \otimes e_\Theta + e_\theta \otimes \frac{\partial e_\Theta}{\partial \Phi} \right) \cdot e_\Phi = \frac{S_2^2}{r \sin \Theta} (\phi' \cos \phi e_\phi \otimes e_\Theta + e_\theta \otimes e_\Phi \cos \Theta) \cdot e_\Phi \\ &= \frac{S_2^2 \cot \Theta}{r} e_\theta, \end{aligned} \quad (75)$$

additionally

$$\begin{aligned}
\frac{\partial}{\partial X^3} (S_3^3 g^3 \otimes G_3) \cdot G^3 &= \frac{\partial}{\partial \Phi} \left( S_3^3 \frac{R \sin \Theta}{r \sin \theta} e_\phi \otimes e_\Phi \right) \cdot \frac{e_\Phi}{R \sin \Theta} = \frac{S_3^3}{r \sin \theta} \frac{\partial}{\partial \Phi} (e_\phi \otimes e_\Phi) \cdot e_\Phi \\
&= \frac{S_3^3}{r \sin \theta} \left( \frac{\partial e_\phi}{\partial \Phi} \otimes e_\Phi + e_\phi \otimes \frac{\partial e_\Phi}{\partial \Phi} \right) \cdot e_\Phi = \frac{S_3^3}{r \sin \theta} (-\phi' \sin \theta e_r \otimes e_\Phi - \phi' \cos \theta e_\theta \otimes e_\Phi) \cdot e_\Phi \\
&= -\frac{S_3^3 \phi'}{r} e_r - \frac{S_3^3 \phi' \cot \theta}{r} e_\theta = -\frac{S_3^3}{r} e_r - \frac{S_3^3 \cot \theta}{r} e_\theta.
\end{aligned} \tag{76}$$

Gathering together equations (68) to (76) inclusive and substituting into  $\nabla \cdot S = 0$  gives the following radial and angular equations

$$\frac{\partial S_1^1}{\partial R} + \frac{2S_1^1}{R} - \frac{1}{r} (S_2^2 + S_3^3) = 0, \tag{77}$$

$$\frac{S_2^2 \cot \Theta}{r} - \frac{S_3^3 \cot \theta}{r} = 0, \tag{78}$$

where  $\theta = \Theta$ , resulting in  $S_2^2 = S_3^3$ . Equation (77) is consistent with Daniel et al [47]. The relationship  $S_2^2 = S_3^3$  is consistent with a spherically symmetric, purely radial deformation. This implies that both the zenith and azimuthal stresses have the same dependency on the radial displacement.

### 3.7 Formulating the Cauchy stresses for the radial equation

To formulate the Cauchy stresses the radial differential equation (77) has to be rewritten in terms of the physical coordinates. Calculating the various terms in

equation (77) using equations (64),(65) and(66) gives, from equation (54),

$$\frac{\partial J}{\partial R} = \frac{r''r^2}{R^2} + \frac{2(r')^2r}{R^2} - \frac{2r'r^2}{R^3} = J \left( \frac{r''}{r'} + \frac{2r'}{r} - \frac{2}{R} \right), \quad (79)$$

$$\begin{aligned} \frac{\partial S_1^1}{\partial R} &= \frac{\partial}{\partial R} \left( \mu \left( -J^{-2\beta} \frac{1}{r'} + r' \right) \right) = \mu \left( 2\beta J^{-2\beta-1} \frac{\partial J}{\partial R} \frac{1}{r'} + J^{-2\beta} \left( \frac{1}{r'} \right)^2 r'' + r'' \right) \\ &= \mu \left( r'' \left( 1 + \frac{(2\beta+1)J^{-2\beta}}{(r')^2} \right) + J^{-2\beta} \left( \frac{4\beta}{r} - \frac{4\beta}{Rr'} \right) \right), \quad (80) \end{aligned}$$

$$\frac{2S_1^1}{R} = \mu \left( \frac{-2J^{-2\beta}}{r'R} + \frac{2r'}{R} \right), \quad (81)$$

$$\frac{-S_2^2}{r} = \mu \left( \frac{J^{-2\beta}}{r} - \frac{r}{R^2} \right), \quad (82)$$

$$\text{and, } \frac{-S_3^3}{r} = \mu \left( \frac{J^{-2\beta}}{r} - \frac{r}{R^2} \right). \quad (83)$$

Substituting equations (80) to (83) into equation (77) and dividing throughout by  $\mu$  gives

$$r'' \left( 1 + \frac{(2\beta+1)J^{-2\beta}}{(r')^2} \right) + J^{-2\beta} \left( \frac{4\beta}{r} - \frac{4\beta}{Rr'} - \frac{2}{r'R} + \frac{2}{r} \right) + \frac{2r'}{R} - \frac{2r}{R^2} = 0,$$

and rearranging

$$r'' \left( (r')^2 J^{2\beta} + 1 + 2\beta \right) = \left( \frac{4\beta r'}{R} - \frac{4\beta (r')^2}{r} + \frac{2r'}{R} - \frac{2(r')^2}{r} \right) + J^{2\beta} \left( \frac{2r(r')^2}{R^2} - \frac{2(r')^3}{R} \right). \quad (84)$$

To determine the Cauchy stresses in the radial and angular directions, equation

(84) is solved for the inner surface of the shell being subjected to a load stress and the outer shell's surface being stress free. Using equation (64), at  $R = R_I$  (the inner radius), this inner boundary condition is

$$S_{rR} = -pJF^{-T}. \quad (85)$$

Hence from equations (53) and (54)

$$S_{rR} = \frac{-pr^2}{R^2}, \quad (86)$$

where  $p$  represents the stress load on the inner shell. From equation (64)

$$\mu \left( -J^{-2\beta} \frac{1}{r'} + r' \right) = \frac{-pr^2}{R^2}.$$

Hence

$$\mu \left( \frac{r'r^2}{R^2} \right)^{-2\beta} - \frac{pr^2r'}{R^2} - \mu(r')^2 = 0. \quad (87)$$

Calculating the boundary condition for the outer shell's radius  $R = R_O$  gives

$$S_{rR} = 0.$$

Hence,

$$-J^{-2\beta} \frac{1}{r'} + r' = 0,$$

and so

$$\left( \frac{r'r^2}{R^2} \right)^{2\beta} = \left( \frac{1}{r'} \right)^2.$$

Rearranging gives the following boundary condition for  $R = R_O$ ,

$$r' = \left(\frac{R}{r}\right)^{2\beta/(\beta+1)}. \quad (88)$$

Equation (84) can now be solved subject to the boundary conditions given by equations (87) and (88). The Cauchy stresses represented by  $\tau$  [[39],p111] are then obtained from the first Piola-Kirchhoff stress tensor given by equation (62)

$$S = \frac{\partial W}{\partial F} = J\tau F^{-T}. \quad (89)$$

and rearranging gives

$$\tau = \frac{1}{J}SF^T. \quad (90)$$

The radial and angular stresses are evaluated using equations (53) and (63)

$$\tau_{rr} = \frac{\mu}{J} (-J^{-2\beta} + (r')^2), \quad (91)$$

$$\tau_{\theta\theta} = \frac{\mu}{J} \left(-J^{-2\beta} + \left(\frac{r}{R}\right)^2\right), \text{ and} \quad (92)$$

$$\tau_{\phi\phi} = \frac{\mu}{J} \left(-J^{-2\beta} + \left(\frac{r}{R}\right)^2\right). \quad (93)$$

## 4 Nondimensionalising the Quasistatic and collapse phases

In this section we will nondimensionalise the theoretical model. Nondimensionalisation is used to assist in solving the quasistatic and collapse phases of the shelled microbubble. This is achieved by using the reference configuration's inner radius,

$R_I$ . This leads to

$$Y = \frac{R}{R_I}, \quad (94)$$

$$\text{and, } y(Y) = \frac{r(R)}{R_I}, \quad (95)$$

where  $Y_I = R_I/R_I = 1$  and  $Y_O = R_O/R_I$ . This results in

$$\frac{\partial r}{\partial R} = \frac{\partial y}{\partial Y}, \quad (96)$$

$$\text{and, } \frac{\partial^2 r}{\partial R^2} = \frac{1}{R_I} \left( \frac{\partial^2 y}{\partial Y^2} \right). \quad (97)$$

Nondimensionalising the Jacobian given by equation (54) results in

$$J = \frac{r'r^2}{R^2} = \frac{y'y^2}{Y^2}, \quad (98)$$

which on substituting into equation (84) leads to

$$y'' \left( (y')^2 \left( \frac{y'y^2}{Y^2} \right)^{2\beta} + 1 + 2\beta \right) = \left( \frac{4\beta y'}{Y} - \frac{4\beta(y')^2}{y} + \frac{2y'}{Y} - \frac{2(y')^2}{y} \right) + \left( \frac{y'y^2}{Y^2} \right)^{2\beta} \left( \frac{2y(y')^2}{Y^2} - \frac{2(y')^3}{Y} \right). \quad (99)$$

Nondimensionalising the boundary condition at the inner radius given by equation (87) and rearranging gives

$$\left( \frac{y'y^2}{Y_I^2} \right)^{-2\beta} - \hat{p} \left( \frac{y'y^2}{Y_I^2} \right) - (y')^2 = 0, \quad (100)$$

where  $y = y(Y_I)$ ,  $y' = y'(Y_I)$  and  $\hat{p} = p/\mu$ . Similarly, nondimensionalising the boundary condition at the outer radius represented by equation (88) leads to

$$y'(Y_O) = \left( \frac{Y_O}{y(Y_O)} \right)^{2\beta/(\beta+1)}. \quad (101)$$

## 5 Linearisation of the inflationary process

In this section we will linearise the inflationary process. The inflationary process, which is purely radially dependent, applies a small stress to the inner radius, with a stress of the order of 1% of the shear modulus of the shell. Applying such a small stress allows us to linearise the model for the inflationary process by assuming that the stress is a small perturbation where  $\epsilon = \hat{p}$ . This implies that the shell will be displaced by a small amount denoted by  $\epsilon f(Y)$  about its equilibrium position which is represented by  $Y$ . Using linearisation

$$y(Y) = Y + \epsilon f(Y),$$

$$y'(Y) = 1 + \epsilon f'(Y), \quad (102)$$

$$y''(Y) = \epsilon f''(Y). \quad (103)$$

The Jacobian given as  $J = y'y^2/Y^2$  is linearised, resulting in

$$J = \frac{y'y^2}{Y^2},$$

$$\approx 1 + \epsilon \left( f' + \frac{2f}{Y} \right). \quad (104)$$



Determining  $J^{2\beta}$  using equation (104) where  $\beta$  is related to Poisson's ratio gives

$$\begin{aligned} J^{2\beta} &= \left(1 + \epsilon \left(f' + \frac{2f}{Y}\right)\right)^{2\beta}, \\ &\approx 1 + 2\beta\epsilon f' + \frac{4\beta\epsilon f}{Y}. \end{aligned} \quad (105)$$

Using equations (102), (103), (104), and (105) and substituting into the first term in equation (84) leads to

$$y'' \left( (y')^2 J^{2\beta} + 1 + 2\beta \right) \approx \epsilon f'' (2\beta + 2). \quad (106)$$

Considering the linearisation process for various terms in equation (84)

$$\frac{4\beta y'}{Y} \approx \frac{4\beta}{Y} + \frac{4\beta\epsilon f'}{Y}, \quad (107)$$

$$\begin{aligned} \frac{-4\beta(y')^2}{y} &= \frac{-4\beta(1 + \epsilon f')^2}{Y + \epsilon f}, \\ &\approx \frac{-4\beta}{Y} + \frac{4\beta\epsilon f}{Y^2} - \frac{8\beta\epsilon f'}{Y}, \end{aligned} \quad (108)$$

$$\begin{aligned} \frac{2y'}{Y} &= \frac{2(1 + \epsilon f')}{Y}, \\ &\approx \frac{2}{Y} + \frac{2\epsilon f'}{Y}, \end{aligned} \quad (109)$$

$$\begin{aligned} \frac{-2(y')^2}{y} &= \frac{-2(1 + \epsilon f')^2}{Y + \epsilon f}, \\ &\approx \frac{-2}{Y} - \frac{4\epsilon f'}{Y} + \frac{2\epsilon f}{Y^2}, \end{aligned} \quad (110)$$

$$\begin{aligned}\frac{2y(y')^2}{Y^2} &= \frac{2(Y + \epsilon f)(1 + \epsilon f')^2}{Y^2}, \\ &= \frac{2}{Y} + \frac{2\epsilon f}{Y^2} + \frac{4\epsilon f'}{Y},\end{aligned}\tag{111}$$

and

$$\begin{aligned}\frac{-2(y')^3}{Y} &= \frac{-2(1 + \epsilon f')^3}{Y}, \\ &\approx \frac{-2}{Y} - \frac{6\epsilon f'}{Y}.\end{aligned}\tag{112}$$

Using equations (105), (111) and (112) leads to

$$J^{2\beta} \left( \frac{2y(y')^2}{Y^2} - \frac{2(y')^3}{Y} \right) \approx \frac{2\epsilon f}{Y^2} - \frac{2\epsilon f'}{Y},\tag{113}$$

and combining equations (107), (108), (109), (110), (113) and substituting into (84) and rearranging results in

$$(2\beta + 2) f'' + \frac{(4\beta + 4)f'}{Y} - \frac{(4\beta + 4)f}{Y^2} = 0,$$

which simplifies to give

$$Y^2 f'' + 2Y f' - 2f = 0.\tag{114}$$

The second order differential equation given by equation (114) is solved by using the algebraic substitution  $f(Y) = Yq(Y)$  leading to

$$f' = Yq' + q,\tag{115}$$

$$f'' = Yq'' + 2q',\tag{116}$$

which, on substituting into equation (114) reduces to

$$Y^3 q'' + 4Y^2 q' = 0. \quad (117)$$

Equation (117) is solved using separation of variables to give

$$q(Y) = \frac{A}{Y^3} + B, \quad (118)$$

where  $A$  and  $B$  are parameters determined using the boundary conditions of the physical system. Substituting equation (118) into  $f(Y) = Yq(Y)$  and combining this with  $y(Y) = Y + \epsilon f(Y)$  yields

$$y(Y) = Y + \epsilon \left( \frac{A}{Y^2} + BY \right), \quad (119)$$

where  $f(Y) = A/Y^2 + BY$  and  $A$  and  $B$  are determined using the boundary conditions represented by equations (100) and (101) where the Cauchy radial stress,  $\tau_{rr}$  is given by equation (91). Linearising the Cauchy radial stress results in

$$\begin{aligned} \hat{\tau}_{yy} &= \frac{\tau_{yy}}{\mu} = \frac{1}{J} \left( -J^{-2\beta} + (y')^2 \right), \\ &\approx \epsilon \left( \frac{4\beta f}{Y} + (2\beta + 2) f' \right). \end{aligned} \quad (120)$$

Linearising the Cauchy hoop stresses represented by  $\tau_{\theta\theta}$  and  $\tau_{\phi\phi}$  given by equations (92) and (93) leads to

$$\begin{aligned} \hat{\tau}_{\theta\theta} = \hat{\tau}_{\phi\phi} &= \frac{1}{J} \left( -J^{-2\beta} + \left( \frac{y}{Y} \right)^2 \right), \\ &\approx \epsilon \left( \frac{(4\beta + 2)f}{Y} + 2\beta f' \right). \end{aligned} \quad (121)$$

Considering the boundary condition at the inner radius, where a stress is applied, and linearising using equation (91), gives

$$\begin{aligned}\hat{\tau}_{yy}(Y_I) &= -\hat{p}, \\ (2\beta + 2) f'(Y_I) + \frac{4\beta f(Y_I)}{Y_I} + 1 &= 0.\end{aligned}\tag{122}$$

Linearising the boundary condition at the outer radius using equation (120) and the boundary condition given by equation (101) yields

$$\begin{aligned}y'(Y_O) &= \left(\frac{Y}{y(Y_O)}\right)^{\frac{2\beta}{\beta+1}}, \\ f'(Y_O) &= \frac{-2\beta}{(\beta+1)} \left(\frac{f(Y_O)}{Y_O}\right).\end{aligned}\tag{123}$$

Substituting  $f(Y)$  from equation (119) into the boundary condition given by equation (123) leads to the relationship

$$A = \frac{Y_O^3}{2} (3\beta + 1) B.\tag{124}$$

Using equation (124) along with the linearised boundary condition for the inner radius given by equation (122) and  $f(Y)$  gives the following expressions for the parameters  $A$  and  $B$

$$A = \frac{Y_O^3}{4Y_O^3/Y_I^3 - 4},\tag{125}$$

$$\text{and } B = \frac{1}{(6\beta + 2)Y_O^3/Y_I^3 - (6\beta + 2)}.\tag{126}$$

The radial displacement  $y(Y)$  is given using equations (119), (125) and (126) resulting in

$$\begin{aligned} y(Y) &= Y + \epsilon f(Y), \\ &= Y + \epsilon \left( \frac{Y_O^3}{Y^2 (4Y_O^3/Y_I^3 - 4)} + \frac{Y}{(6\beta + 2)Y_O^3/Y_I^3 - (6\beta + 2)} \right). \end{aligned} \quad (127)$$

Substituting equations (125) and (126) into equations (120) and (121) for the Cauchy radial and hoop stresses where  $\hat{\tau}_{\theta\theta} = \hat{\tau}_{\phi\phi}$ , respectively gives

$$\begin{aligned} \hat{\tau}_{yy} &= \epsilon \left( \frac{4\beta f}{Y} + (2\beta + 2) f' \right), \\ &= \epsilon \left( \frac{Y^3 - Y_O^3}{Y^3 (Y_O^3/Y_I^3 - 1)} \right), \end{aligned} \quad (128)$$

$$\begin{aligned} \text{and, } \hat{\tau}_{\theta\theta} &= \epsilon \left( (4\beta + 2) \frac{f}{Y} + 2\beta f' \right), \\ &= \epsilon \left( \frac{Y_O^3}{Y^3 (2Y_O^3/Y_I^3 - 2)} + \frac{1}{Y_O^3/Y_I^3 - 1} \right). \end{aligned} \quad (129)$$

## 6 Linearisation of the time evolving collapse phase of the shell

In this section we will linearise the collapse phase of the shell. Applying the conservation of linear momentum ([45],p143-p145) where  $\rho_o$  denotes the density in the reference configuration,  $v$  represents the velocity and  $t$  denotes the time leads to

$$\rho_o \frac{Dv}{Dt} = \nabla_R \cdot S, \quad (130)$$

where the radial material derivative is given by  $Dv_r/Dt = \partial v_r/\partial t + (v \cdot \nabla)v_r - v_\theta^2/r - v_\phi^2/r$  ([45],p143-p145). Writing equation (130) in terms of the Cauchy stress leads to

$$\rho \frac{Dv}{Dt} = \nabla_r \cdot \tau \quad (131)$$

where  $|v| = v_r$ ,  $v_\phi = 0$  and  $v_\theta = 0$  (radial dependency only) ([48], p354-p355). To collapse the shell a change in the boundary conditions has to be applied to the inner radius of the shell. In the inflationary picture there is a stress applied at the inner radius, directed radially outwards, but to collapse the shell the stress at the inner radius is “switched off” under the assumption that the switching off procedure does not add to or subtract from the potential energy of the inflated shell. This switching off procedure will cause the shell to collapse inwardly resulting in an oscillatory characteristic behaviour that is effectively simple harmonic motion. The simple harmonic motion is driven by the unbalanced tensions in the shell due to the stress applied at the inner radius during the inflationary process where the stresses are described by the generic equations given by equations (91), (92) and (93). The momentum of the shell is now no longer zero but is evaluated by considering the unbalanced stresses acting on the shell which are described by equations (91), (92) and (93). To determine  $\tau$  in equation (131) we need to consider the nature of the stresses in the quasistatic (forward) picture. The quasistatic model has a radial component of linear momentum that satisfies

$$\nabla_r \cdot \tau = \left( \frac{\partial \tau_{rr}}{\partial r} + \frac{2}{r} (\tau_{rr} - \tau_{\theta\theta}) \right) e_r = 0, \quad (132)$$

where  $\partial \tau_{rr}/\partial r$  is positive due to the radially outwardly directed stress. To collapse the shell this becomes  $-\partial \tau_{rr}/\partial r$  which represents a compression and results in the

shell collapsing inwards giving a Cauchy stress described by

$$\nabla_r \cdot \tau = \left( -\frac{\partial \tau_{rr}}{\partial r} + \frac{2}{r} (\tau_{rr} - \tau_{\theta\theta}) \right) e_r, \quad (133)$$

where  $\tau_{rr}$  and  $\tau_{\theta\theta}$  are given by equations (91), (92) and (93) and the momentum is no longer zero. Equation (132) describes how the stresses are balanced and represents both stretching and compressive terms during the quasistatic inflationary phase. However their respective signs are adjusted in equation (133) to represent compression terms only for the collapse phase of the shell. Substituting equations (91), (92) and (93) into equation (133) leads to

$$\begin{aligned} \nabla_r \cdot \tau = \frac{\mu}{J} \left( (2\beta + 1) J^{-2\beta} \left( -\frac{\partial^2 r}{\partial R^2} \left( \frac{\partial R}{\partial r} \right)^2 - \frac{2}{r} + \frac{2}{R} \left( \frac{\partial R}{\partial r} \right) \right) \right) e_r \\ + \frac{\mu}{J} \left( -\frac{2}{R} \left( \frac{\partial r}{\partial R} \right) + \frac{4}{r} \left( \frac{\partial r}{\partial R} \right)^2 - \frac{\partial^2 r}{\partial R^2} - \frac{2r}{R^2} \right) e_r. \end{aligned} \quad (134)$$

Equation (131) can be rewritten as

$$\rho_o J \left( \frac{\partial^2 r}{\partial t^2} + \left( \frac{\partial r}{\partial t} \frac{\partial}{\partial r_i} \right) \frac{\partial r}{\partial t} \right) e_r = \nabla_r \cdot \tau, \quad (135)$$

and is nondimensionalised using  $y(Y) = r/R_I$  and  $Y = R/R_I$  where the Jacobian reduces to

$$J = \frac{y^2}{Y^2} \left( \frac{\partial y}{\partial Y} \right). \quad (136)$$

To nondimensionalise the time we use  $t = \gamma \hat{t}$  which results in

$$\begin{aligned} \frac{\partial r}{\partial t} &= \frac{R_I}{\gamma} \left( \frac{\partial y}{\partial \hat{t}} \right), \\ \text{and } \frac{\partial^2 r}{\partial t^2} &= \frac{R_I}{\gamma^2} \frac{\partial^2 y}{\partial \hat{t}^2}, \end{aligned} \quad (137)$$

where the convective derivative reduces to

$$\left(\frac{\partial r}{\partial t} \frac{\partial}{\partial r_i}\right) \frac{\partial r}{\partial t} = \frac{R_I}{\gamma^2} \left(\frac{\partial y}{\partial \hat{t}} \frac{\partial}{\partial y_i}\right) \frac{\partial y}{\partial \hat{t}}.$$

The left hand side of equation (131) gives

$$\rho \frac{Dv}{Dt} = \frac{\rho_o R_I}{\gamma^2} \frac{y^2}{Y^2} \left(\frac{\partial y}{\partial Y}\right) \left(\frac{\partial^2 y}{\partial \hat{t}^2} + \left(\frac{\partial y}{\partial \hat{t}} \frac{\partial}{\partial y_i}\right) \frac{\partial y}{\partial \hat{t}}\right) e_r, \quad (138)$$

with the right hand side of equation (131) reducing to

$$\begin{aligned} \nabla_r \cdot \tau = & \frac{\mu}{R_I J} \left( (2\beta + 1) J^{-2\beta} \left( -\frac{\partial^2 y}{\partial Y^2} \left(\frac{\partial Y}{\partial y}\right)^2 - \frac{2}{y} + \frac{2}{Y} \left(\frac{\partial Y}{\partial y}\right) \right) \right) e_r \\ & + \frac{\mu}{R_I J} \left( -\frac{2}{Y} \left(\frac{\partial y}{\partial Y}\right) + \frac{4}{y} \left(\frac{\partial y}{\partial Y}\right)^2 - \frac{\partial^2 y}{\partial Y^2} - \frac{2y}{Y^2} \right) e_r. \end{aligned} \quad (139)$$

The shear modulus  $\mu$  is related to a nondimensionalised shear modulus  $\mu_r$  where  $\mu_r = \mu/\mu_o$  and  $\mu_o = 20\text{MPa}$  [44]. This allows us to study the influence that the shear modulus has on the collapse time of the shell whilst keeping  $\gamma$  fixed as  $\mu$  is varied. This will result in a nondimensionalised time  $\hat{t}$  which varies as  $\mu$  changes whilst  $\gamma$  remains fixed. Substituting equations (138) and (139) into equation (131) and setting  $\gamma = \sqrt{\rho_o R_I^2 / \mu_o}$  leads to the nondimensionalised linear momentum equation

$$\begin{aligned} & \frac{y^2}{Y^2} \left(\frac{\partial y}{\partial Y}\right) \left(\frac{\partial^2 y}{\partial \hat{t}^2} + \left(\frac{\partial y}{\partial \hat{t}} \cdot \nabla_{y_i}\right) \frac{\partial y}{\partial \hat{t}}\right) \\ & = \mu_r \left( (2\beta + 1) J^{-2\beta-1} \left( -\frac{\partial^2 y}{\partial Y^2} \left(\frac{\partial Y}{\partial y}\right)^2 - \frac{2}{y} + \frac{2}{Y} \left(\frac{\partial Y}{\partial y}\right) \right) \right) \\ & \quad + \frac{\mu_r}{J} \left( -\frac{2}{Y} \left(\frac{\partial y}{\partial Y}\right) + \frac{4}{y} \left(\frac{\partial y}{\partial Y}\right)^2 - \frac{\partial^2 y}{\partial Y^2} - \frac{2y}{Y^2} \right). \end{aligned} \quad (140)$$



Applying the boundary conditions at the inner and outer radii where the stress is set to zero such that  $\tau_{yy}(Y_{I/O}) = 0$  gives

$$\frac{\partial y(Y_I, \hat{t})}{\partial Y} = \left( \frac{y(Y_I, \hat{t})}{Y_I} \right)^{-2\beta/(\beta+1)}, \quad (141)$$

$$\text{and } \frac{\partial y(Y_O, \hat{t})}{\partial Y} = \left( \frac{y(Y_O, \hat{t})}{Y_O} \right)^{-2\beta/(\beta+1)}, \quad (142)$$

where the nondimensionalised initial conditions are given by

$$y(Y, 0) = Y + \epsilon f(Y), \quad (143)$$

$$\text{and } \frac{\partial y(Y, 0)}{\partial \hat{t}} = 0. \quad (144)$$

Linearising where  $\epsilon = \hat{p}$  and the perturbation is denoted by  $\epsilon g(Y, \hat{t})$  and possesses both a space and time dependency results in

$$\begin{aligned} y &= Y + \epsilon g(Y, \hat{t}), \\ \frac{\partial y}{\partial \hat{t}} &= \epsilon \frac{\partial g}{\partial \hat{t}}, \\ \frac{\partial^2 y}{\partial \hat{t}^2} &= \epsilon \frac{\partial^2 g}{\partial \hat{t}^2}. \end{aligned} \quad (145)$$

Linearising the Jacobian given by equation (136) gives

$$\frac{y^2}{Y^2} \left( \frac{\partial y}{\partial Y} \right) \approx 1 + \frac{2\epsilon g}{Y} + \epsilon \frac{\partial g}{\partial Y}, \quad (146)$$

and the convective derivative results in

$$\left( \frac{\partial y}{\partial \hat{t}} \cdot \nabla_{y_i} \right) \frac{\partial y}{\partial \hat{t}} = 0, \quad (147)$$

since it is a higher order  $\epsilon$  term. The left hand side of equation (140) reduces to

$$\frac{y^2}{Y^2} \left( \frac{\partial y}{\partial Y} \right) \left( \frac{\partial^2 y}{\partial \hat{t}^2} + \left( \frac{\partial y}{\partial \hat{t}} \cdot \nabla_{y_i} \right) \frac{\partial y}{\partial \hat{t}} \right) \approx \epsilon \frac{\partial^2 g}{\partial \hat{t}^2}, \quad (148)$$

and the various terms on the right hand side of equation (140) are

$$-\frac{\partial^2 y}{\partial Y^2} \left( \frac{\partial Y}{\partial y} \right)^2 \approx -\epsilon \frac{\partial^2 g}{\partial Y^2}, \quad (149)$$

and

$$-\frac{2}{y} \approx -\frac{2}{Y} + \frac{2\epsilon g}{Y^2}, \quad (150)$$

also

$$\frac{2}{Y} \left( \frac{\partial Y}{\partial y} \right) \approx \frac{2}{Y} - \frac{2\epsilon}{Y} \left( \frac{\partial g}{\partial Y} \right). \quad (151)$$

Combining equations (149), (150) and (151) leads to

$$-\frac{\partial^2 y}{\partial Y^2} \left( \frac{\partial Y}{\partial y} \right)^2 - \frac{2}{y} + \frac{2}{Y} \left( \frac{\partial Y}{\partial y} \right) \approx -\epsilon \frac{\partial^2 g}{\partial Y^2} + \frac{2\epsilon g}{Y^2} - \frac{2\epsilon}{Y} \left( \frac{\partial g}{\partial Y} \right), \quad (152)$$

and

$$J^{-2\beta-1} \approx 1 - (2\beta + 1) \left( \frac{2\epsilon g}{Y} + \epsilon \frac{\partial g}{\partial Y} \right), \quad (153)$$

where

$$(2\beta + 1) J^{-2\beta-1} \left( -\frac{\partial^2 y}{\partial Y^2} \left( \frac{\partial Y}{\partial y} \right)^2 - \frac{2}{y} + \frac{2}{Y} \left( \frac{\partial Y}{\partial y} \right) \right) \approx (2\beta + 1) \left( -\epsilon \frac{\partial^2 g}{\partial Y^2} + \frac{2\epsilon g}{Y^2} - \frac{2\epsilon}{Y} \left( \frac{\partial g}{\partial Y} \right) \right). \quad (154)$$

Other terms on the right hand side of equation (140) linearise resulting in

$$-\frac{2}{Y} \left( \frac{\partial y}{\partial Y} \right) \approx -\frac{2}{Y} - \frac{2\epsilon}{Y} \left( \frac{\partial g}{\partial Y} \right), \quad (155)$$

and

$$\frac{4}{y} \left( \frac{\partial y}{\partial Y} \right)^2 \approx \frac{4}{Y} - \frac{4\epsilon g}{Y^2} + \frac{8\epsilon}{Y} \left( \frac{\partial g}{\partial Y} \right), \quad (156)$$

also

$$-\frac{\partial^2 y}{\partial Y^2} \approx -\epsilon \frac{\partial^2 g}{\partial Y^2}, \quad (157)$$

and

$$-\frac{2y}{Y^2} \approx -\frac{2}{Y} - \frac{2\epsilon g}{Y^2}. \quad (158)$$

Combining equations (155), (156), (157) and (158) leads to

$$-\frac{2}{Y} \left( \frac{\partial y}{\partial Y} \right) + \frac{4}{y} \left( \frac{\partial y}{\partial Y} \right)^2 - \frac{\partial^2 y}{\partial Y^2} - \frac{2y}{Y^2} = \frac{6\epsilon}{Y} \left( \frac{\partial g}{\partial Y} \right) - \frac{6\epsilon g}{Y^2} - \epsilon \frac{\partial^2 g}{\partial Y^2}, \quad (159)$$

and

$$\frac{1}{J} \left( -\frac{2}{Y} \left( \frac{\partial y}{\partial Y} \right) + \frac{4}{y} \left( \frac{\partial y}{\partial Y} \right)^2 - \frac{\partial^2 y}{\partial Y^2} - \frac{2y}{Y^2} \right) \approx \frac{6\epsilon}{Y} \left( \frac{\partial g}{\partial Y} \right) - \frac{6\epsilon g}{Y^2} - \epsilon \frac{\partial^2 g}{\partial Y^2}. \quad (160)$$

Substituting equations (154) and (160) into the momentum equation (140) and cancelling out the small nondimensionalised parameter  $\epsilon$  where  $\epsilon = \hat{p}$  gives us

$$\frac{\partial^2 g}{\partial \hat{t}^2} = \mu_r \left( -(2\beta + 2) \frac{\partial^2 g}{\partial Y^2} - \frac{(4\beta - 4)}{Y} \left( \frac{\partial g}{\partial Y} \right) + (4\beta - 4) \frac{g}{Y^2} \right), \quad (161)$$

which is solved using separation of variables where  $g(Y, \hat{t}) = H(Y)T(\hat{t})$ . Substituting into equation (161) and rearranging results in

$$\frac{\ddot{T}}{T} = \mu_r \left( -(2\beta + 2) \frac{H''}{H} - \frac{(4\beta - 4)}{Y} \left( \frac{H'}{H} \right) + \frac{(4\beta - 4)}{Y^2} \right) = A, \quad (162)$$

where  $A$  is a constant and the general solution is given by

$$T(\hat{t}) = C_1 \exp(\sqrt{A}\hat{t}) + C_2 \exp(-\sqrt{A}\hat{t}), \quad (163)$$

where  $A = -\omega^2$ . Applying the initial condition (143) using the forward picture  $f(Y)$  results in

$$y = Y + \epsilon f(Y), \quad (164)$$

$$y(Y, 0) = Y + \epsilon g(Y, 0), \quad (165)$$

with  $g(Y, 0) = f(Y)$  leading to  $H(Y) = f(Y)/T(0)$ . This initial condition places a restriction on  $H(Y)$  implying that the forward and collapse paths are equivalent implying that there is no hysteresis since there is no viscoelasticity (fluid resistance) incorporated in the physical model. Substituting the initial condition that  $H(Y) = f(Y)/T(0)$  into equation (162) results in the angular frequency  $\omega$  which is given by

$$-\omega^2 = \mu_r \left( -(2\beta + 2) \left( \frac{f''}{f} \right) - \frac{(4\beta - 4)}{Y} \left( \frac{f'}{f} \right) + \frac{(4\beta - 4)}{Y^2} \right). \quad (166)$$

The second initial condition places a restriction on the initial velocity of the shell such that

$$\frac{\partial g(Y, 0)}{\partial \hat{t}} = 0 \quad (167)$$

and the two boundary conditions are such that the Cauchy radial stress  $\tau_{yy}$  is set to zero at both the inner and outer surface of the shell. Setting  $\tau_{yy}(Y_{I/O}) = 0$

leads to

$$g'(Y_I, t) = \frac{-2\beta}{(\beta + 1)} \left( \frac{g(Y_I, t)}{Y_I} \right), \quad (168)$$

$$\text{and, } g'(Y_O, t) = \frac{-2\beta}{(\beta + 1)} \left( \frac{g(Y_O, t)}{Y_O} \right), \quad (169)$$

which, on separating out equations (168) and (169) using the approach of separation of variables given by  $g(Y, \hat{t}) = H(Y)T(\hat{t})$  results in

$$H'(Y_I) = \frac{-2\beta}{(\beta + 1)} \left( \frac{H(Y_I)}{Y_I} \right), \quad (170)$$

$$\text{and, } H'(Y_O) = \frac{-2\beta}{(\beta + 1)} \left( \frac{H(Y_O)}{Y_O} \right). \quad (171)$$

The nondimensionalised time evolutionary phase of the collapsing shell is evaluated by applying the initial condition given by equation (167) with the angular frequency  $\omega$  evaluated using equation (166) which gives

$$y(Y, \hat{t}) = Y + \hat{p} \left( \frac{Y_O^3}{Y^2 (4Y_O^3/Y_I^3 - 4)} + \frac{Y}{(6\beta + 2)Y_O^3/Y_I^3 - (6\beta + 2)} \right) \cos \omega \hat{t}. \quad (172)$$

## 7 Results for the inflationary phase of the shelled microbubble

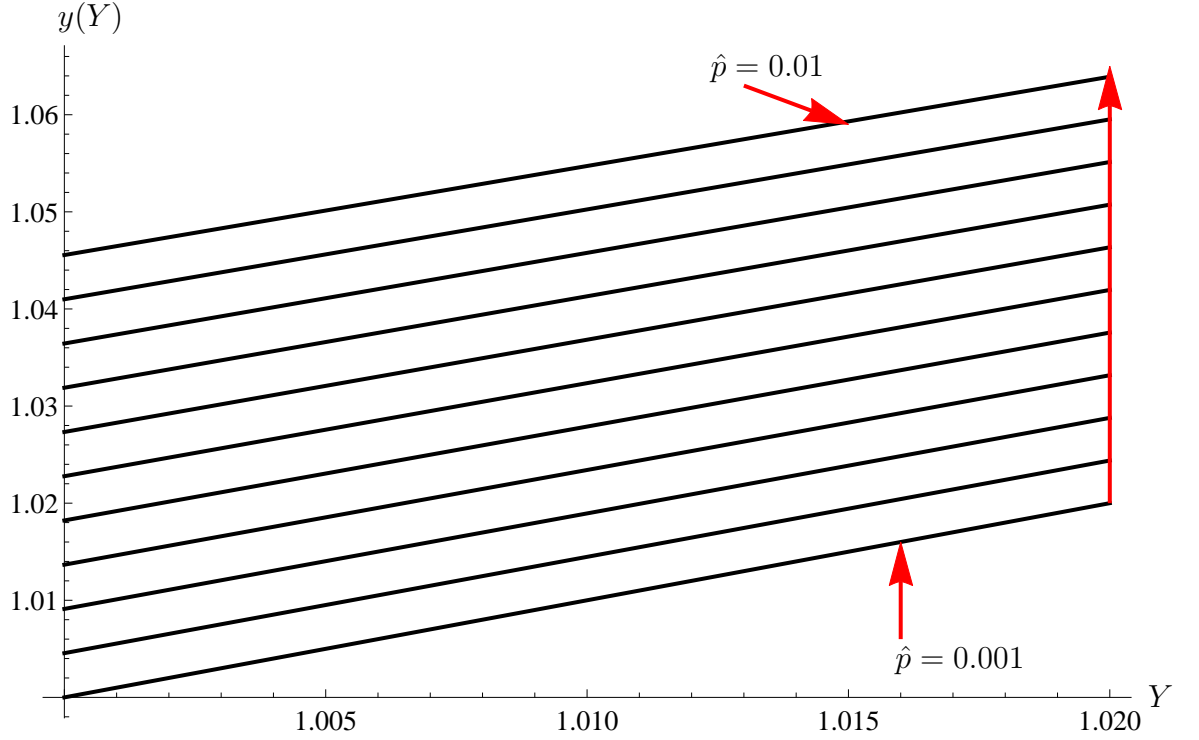


Figure 3: Graph of the nondimensionalised radial displacement versus the nondimensionalised reference configuration's radial coordinates for different nondimensionalised internal stress loads given by  $\hat{p} = 0, 0.001, 0.002, \dots, 0.01$  where  $\nu = 0.48$ ,  $\beta = 12$  and the initial thickness is  $Y_O - Y_I = 0.02$ . This is calculated using equation (127).

Figure 3 illustrates the linear relationship between radial displacement of the inflated shell and the reference configuration (which remains fixed) for a series of stress steps. The red vertical arrow highlights the direction of increasing small stress steps. As the stress steps increase in magnitude the slope of each successive line decreases slightly. This is due to the material being compressed more at the inner radius than the outer radius.

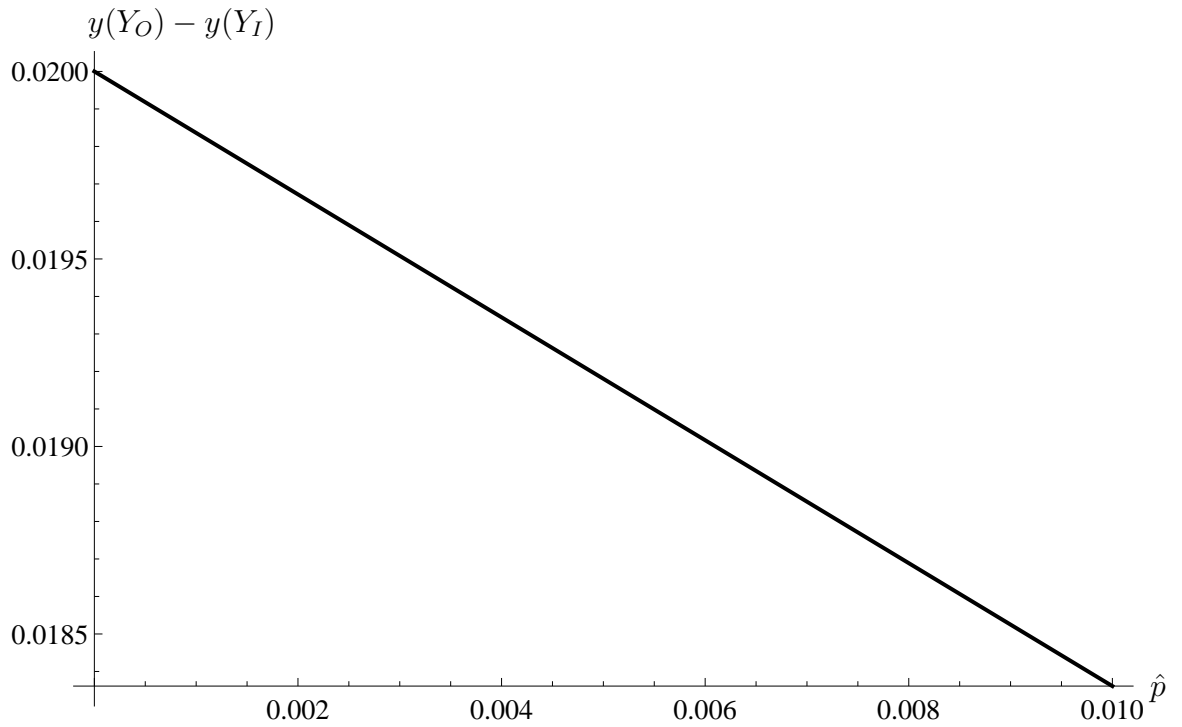


Figure 4: Graph of the nondimensionalised thickness of the shell versus the nondimensionalised stress load where  $\nu = 0.48$ ,  $\beta = 12$  and the initial thickness is  $Y_O - Y_I = 0.02$ . This is calculated using equation (127).

Figure 4 illustrates the linear relationship between the nondimensionalised thickness of the shell and the applied nondimensionalised stress. The negative slope highlights a decreasing shell thickness as the applied stress increases. This is a result of the microsphere expanding radially and the thinning of the shell is indicative of a compressive stress.

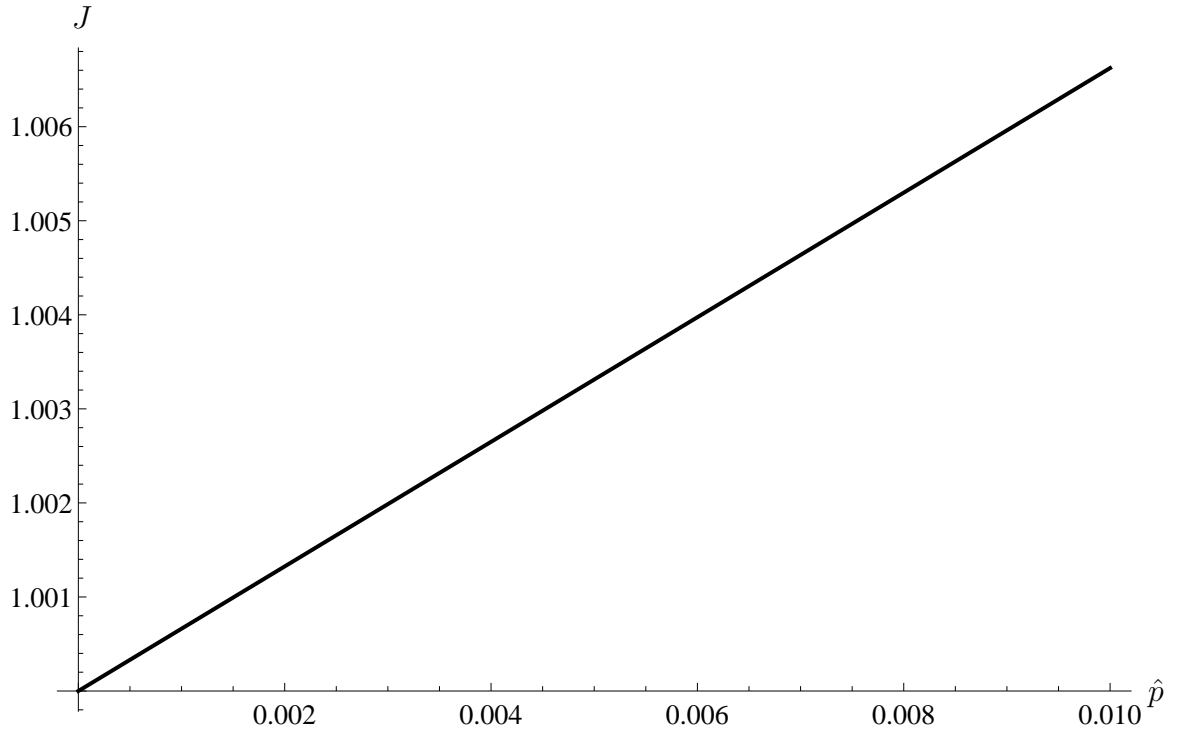


Figure 5: Graph of the Jacobian of the shell versus the nondimensionalised stress load where  $\nu = 0.48$ ,  $\beta = 12$  and the initial thickness is  $Y_O - Y_I = 0.02$ . This is calculated using equations (54), (104) and (127).

Figure 5 shows the linear relationship between the Jacobian of the shell, given by equation (54), versus the stress load. The Jacobian measures the change in the volume of the shell as it inflates and a positive slope highlights that the volume of the shell is increasing. The change in volume at the final stress of  $\hat{p} = 0.01$  is approximately 0.7% of its original volume which is small and very close to the condition of incompressibility. This very small change in the volume of the shell is due in part to the linearisation approximation leading to a slight loss in mass conservation (see Figure 6) and a change in the density of the shell.



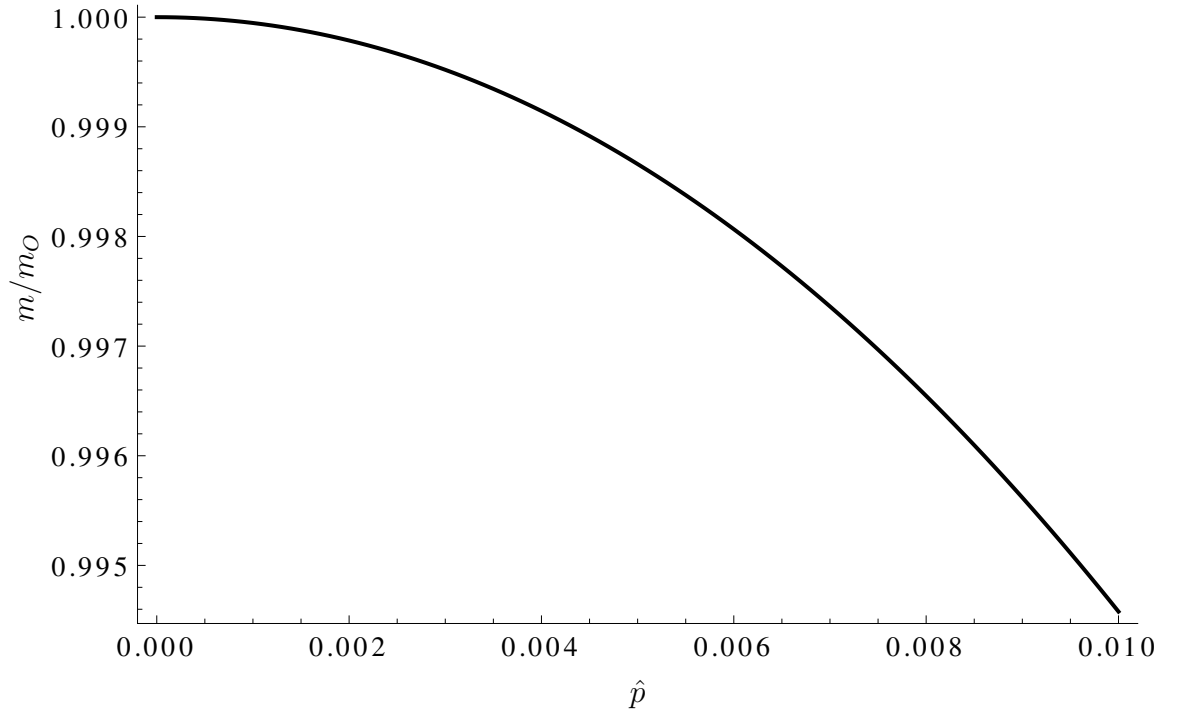


Figure 6: Graph of the normalised mass of the shell versus the nondimensionalised stress load where where  $\nu = 0.48$ ,  $\beta = 12$  and the initial thickness is  $Y_O - Y_I = 0.02$ . This is calculated using  $\rho_0 = \rho J$  alongside equations (54), (104) and (127).

Figure 6 illustrates the normalised mass versus the nondimensionalised stress steps up to a stress of  $\hat{p} = 0.01$ ; the normalised mass is achieved by dividing the mass at each stress step by the mass at the initial stress  $\hat{p} = 0$ . Figure 6 is used to validate the conservation of mass, and whilst the graph is not exactly 1, there is a very small variation in the mass as the stress increases with approximately 0.6% error in the mass conservation at the final stress of  $\hat{p} = 0.01$ . The nonlinear nature of the plot could be a consequence of the linearisation of this nonlinear elastic model.

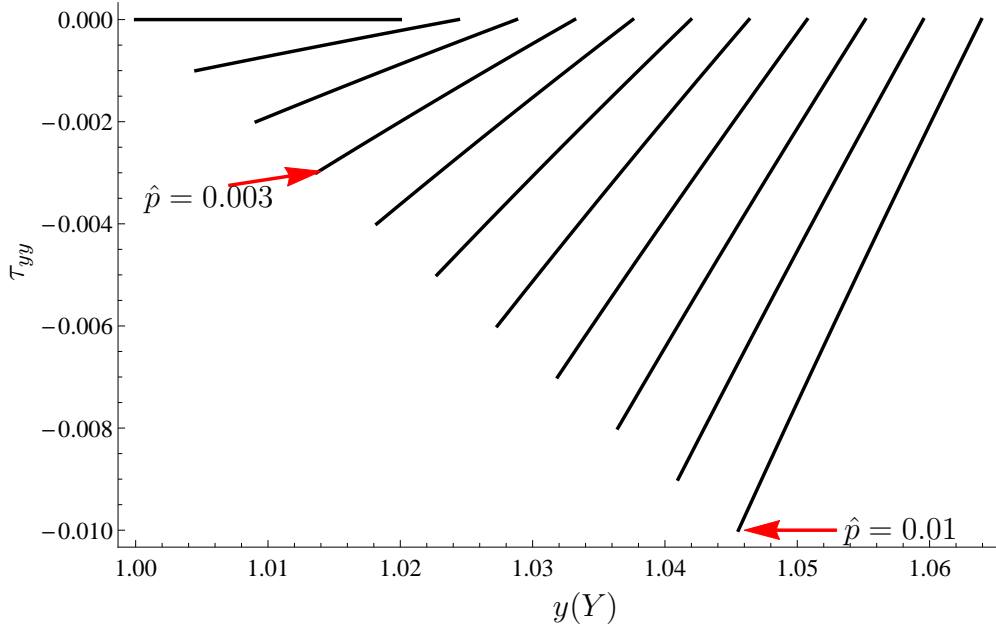


Figure 7: Graph of the nondimensionalised radial Cauchy stress of the shell versus the nondimensionalised radial displacement for various nondimensionalised internal stress loads where  $\hat{p} = 0, 0.001, 0.002, \dots, 0.01$ ,  $\nu = 0.48$ ,  $\beta = 12$  and the initial thickness is  $Y_O - Y_I = 0.02$ . This is calculated using equation (128).

Figure 7 shows the relationship between the nondimensionalised Cauchy radial stress, which is normal to the surface,  $\tau_{yy}$ , and the nondimensionalised radial displacement,  $y(Y)$ , for a series of radially directed stress steps. The Cauchy radial stress is linear in nature and is greater at the inner radius than its value at the outer radius. This is because the stress is zero at the outer radius and nonzero at the inner radius during the inflationary process. Figure 7 illustrates a Cauchy radial stress which is negative, indicating that the stress is compressive. This is a consequence of the shell thinning down during the inflationary process resulting in smaller material particle spacing in the shell. Note that the Cauchy radial stress at the inner radius is equal in magnitude to the applied stress steps that are applied to the inner radius of the shell. This is not surprising since it

merely reflects Newton's third law of motion.

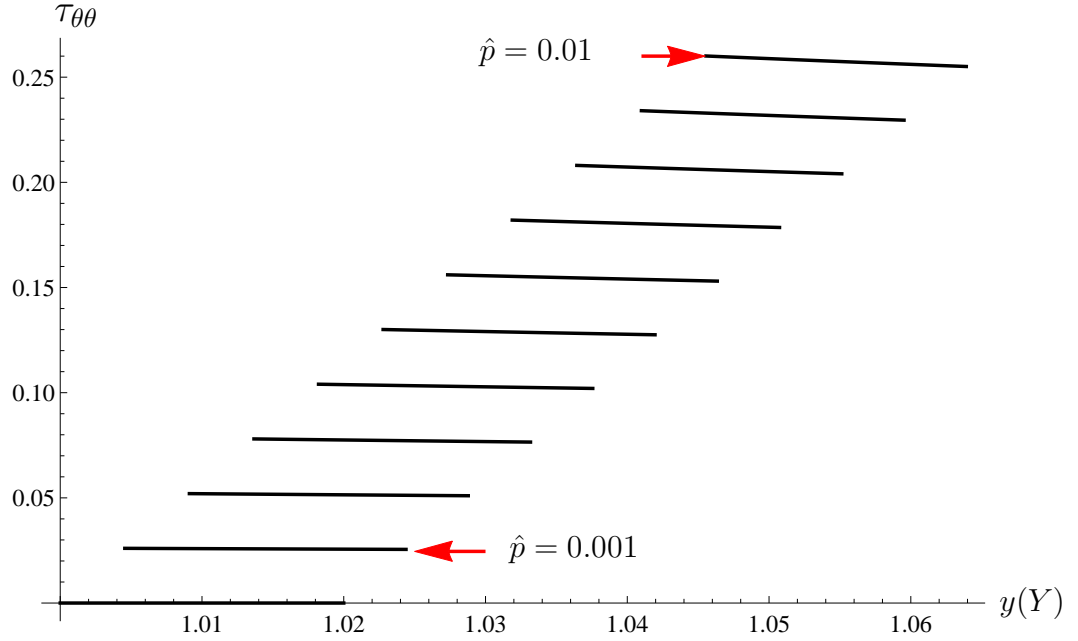


Figure 8: Graph of the normalised Cauchy angular stress (hoop stress) of the shell versus the nondimensionalised radial displacement for various nondimensionalised internal stress loads where  $\hat{p} = 0, 0.001, 0.002, \dots, 0.01$ ,  $\nu = 0.48$ ,  $\beta = 12$  and the initial thickness is  $Y_O - Y_I = 0.02$ . This is calculated using equation (129).

Figure 8 highlights the relationship between the nondimensionalised Cauchy angular stress ( $\tau_{\theta\theta}$ ) versus the nondimensionalised radial displacement for a range of stress steps up to a nondimensionalised inflationary stress of  $\hat{p} = 0.01$ . The graph shows Cauchy hoop stresses that are linear and essentially flat over the range of radial displacements varying from the inner to the outer radii. The Cauchy hoop stress  $\tau_{\theta\theta}$  is equal in magnitude to  $\tau_{\phi\phi}$  due to the spherically directed nature of the radial deformation and is positive indicating a stretching behaviour acting on the material particles that make up the shell. There is a significant increase in the magnitude of the Cauchy angular stresses in comparison to the Cauchy radial stresses which were represented by Figure 7. This would suggest that the hoop

stresses play the key role in dictating the bursting of the shelled microbubble. It is interesting to note that the Cauchy angular stress is very slightly larger at the inner radius than the outer radius which is a result of the material particle spacing in the shell changing radially.

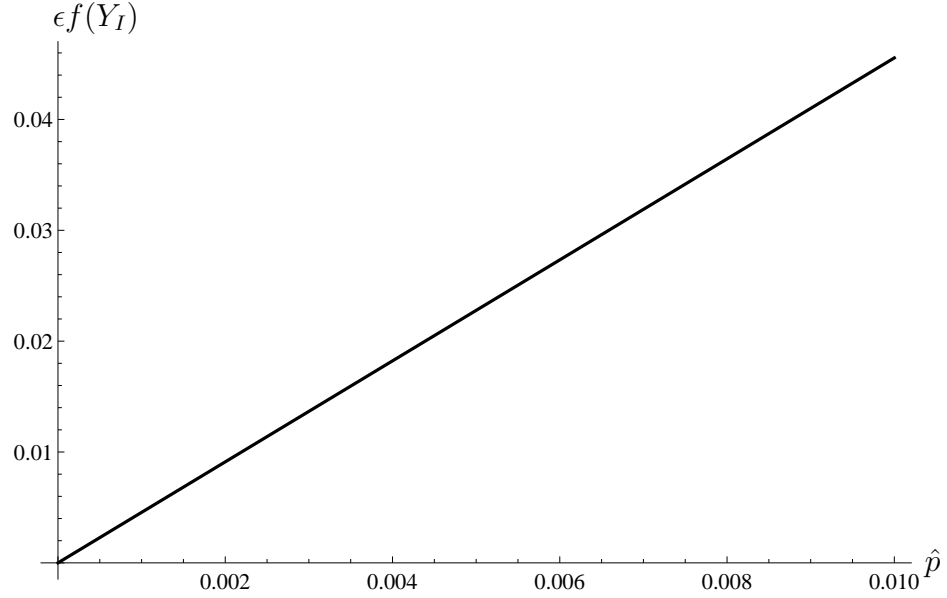


Figure 9: Graph of the normalised radial perturbation of the shell versus the nondimensionalised stress load where  $\nu = 0.48$ ,  $\beta = 12$  and the initial thickness is  $Y_O - Y_I = 0.02$ . This is calculated using equation (127).

Figure 9 illustrates the nondimensionalised radial perturbation at the inner radius of the shell against the nondimensionalised inflationary stress load. Clearly, the relationship between the radial perturbation and the inflationary stress is linear in nature. The linearity is a consequence of the small stress load in relation to the shear modulus of the shell and validates the use of asymptotic expansion in modelling the inflationary process as stated in equation (102). The nondimensionalised radial perturbation at the outer radius is similar.

## 8 Results for the collapse phase of the shelled microbubble

In this section we will analyse the results for the collapse phase of the shell. Having produced results for the inflationary phase of the microbubble's evolution, the stresses that are created within the shell can be used as an initial condition to a collapsing phase. This is achieved by setting the boundary condition on the inner surface of the shell to be stress free.

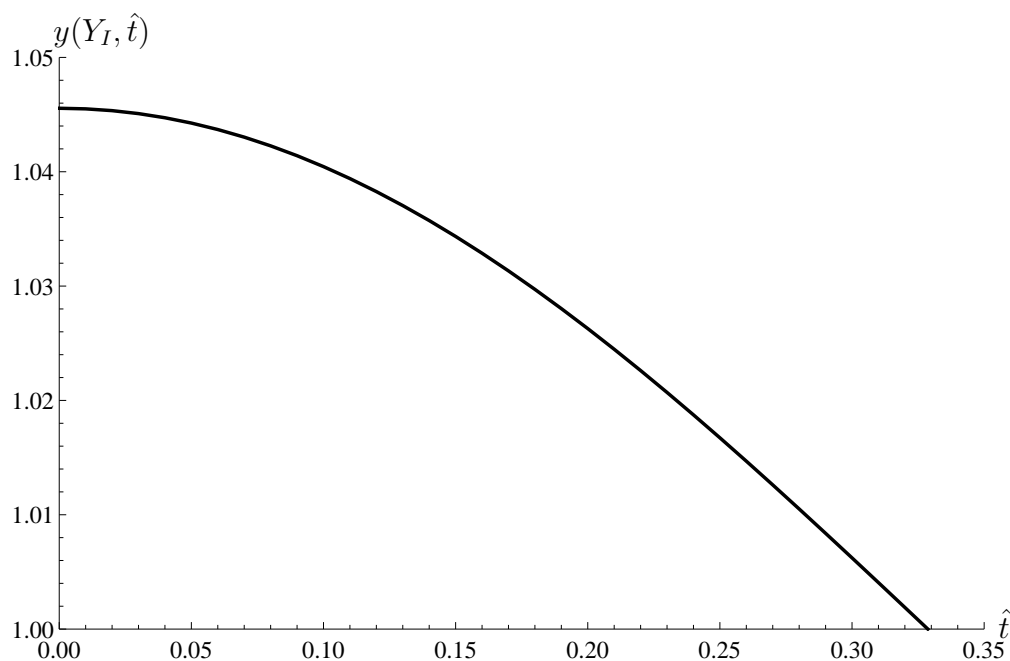


Figure 10: Graph of the nondimensionalised inner radial collapsing shell versus the nondimensionalised time for a nondimensionalised stress load of  $\hat{p} = 0.01$  where  $\nu = 0.48$ ,  $\beta = 12$  and an initial thickness of  $Y_O - Y_I = 0.02$ . This is calculated using equation (172).

Figure 10 illustrates the nondimensionalised inner radius' collapse versus a nondimensionalised time for an initial condition based on an inflationary stress load that is 1% of the shear modulus of the shell ( $\hat{p} = 0.01$ ). The resulting nonlinear trend is a sinusoidal function that is described by equation (172) and

the collapse time,  $\hat{t}^* \approx 0.33$ , denotes the time taken for the stressed shell to reach its stress free, equilibrium position (this is one quarter of the period of a oscillation). Extending the plot in Figure 10 will result in a cosine curve with a regular periodicity and a constant amplitude of oscillation. This is because there are no dissipative, damping terms in the momentum equation that we would normally associate with body forces such as viscoelastic terms connected to the viscosity of the shell and the surrounding fluid. Negating the fluid resistance results in a simple harmonic behaviour with no resulting energy dissipation to the surrounding medium.

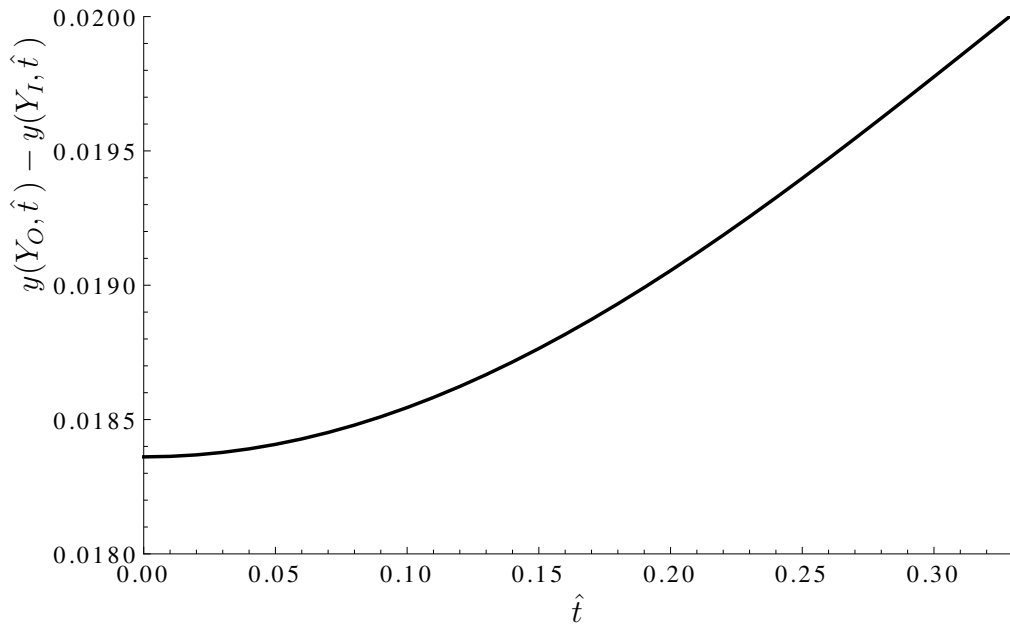


Figure 11: Graph of the nondimensionalised thickness of the collapsing shell versus the nondimensionalised time for an initial nondimensionalised stress load of  $\hat{p} = 0.01$  where  $\nu = 0.48$ ,  $\beta = 12$  and an initial stress free thickness of  $Y_O - Y_I = 0.02$ . This is calculated using equation (172).

Figure 11 illustrates the nonlinear behaviour of the collapsing shell's thickness as it evolves with time. The plot shows the stressed shell collapsing back to its stress free equilibrium position with the shell's thickness increasing until it reaches

its initial stress free thickness of  $Y_O - Y_I = 0.02$ .

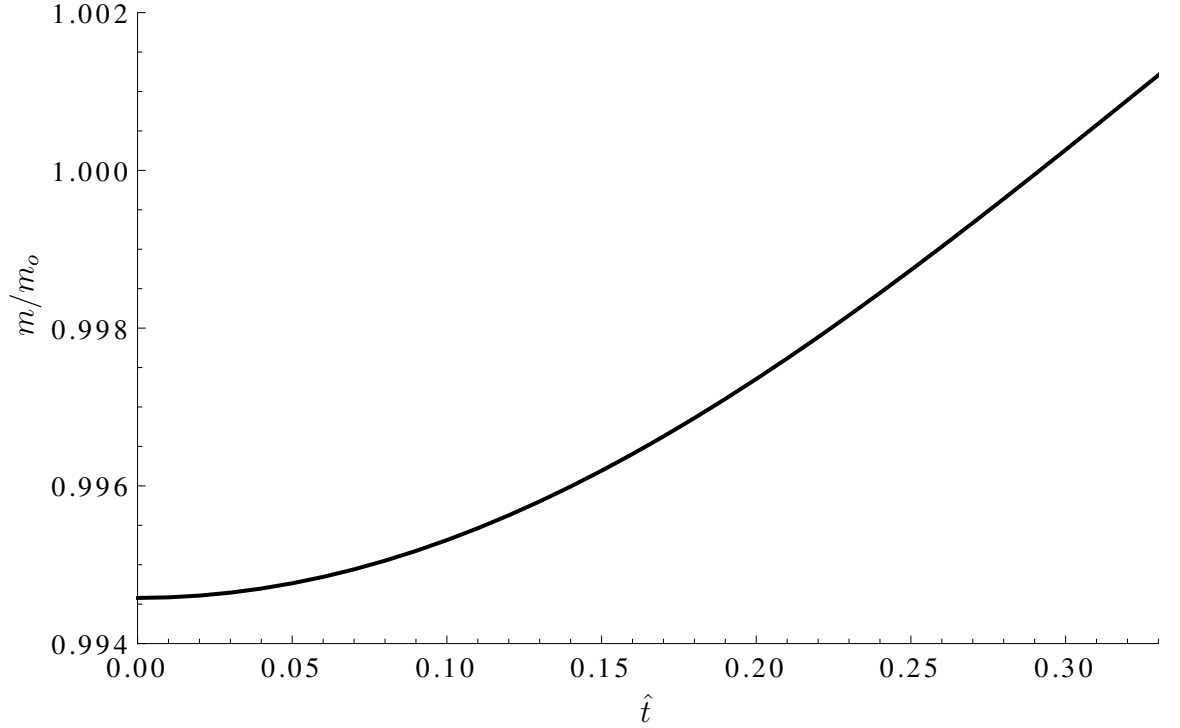


Figure 12: Graph of the normalised mass of the collapsing shell versus the nondimensionalised time for an initial nondimensionalised stress load of  $\hat{p} = 0.01$  where  $\nu = 0.48$ ,  $\beta = 12$  and an initial stress free thickness of  $Y_O - Y_I = 0.02$ . This is calculated using  $\rho_o = \rho J$  and equations (104),(166),(170),(171) and (172).

Figure 12 illustrates the behaviour of the normalised mass of the shell as it evolves with time until it collapses to its stress free equilibrium position. The initial value for the normalised mass is  $\approx 99.4\%$  of its original stress free mass and represents the mass after the shell has been stressed and inflated. As the shell collapses its normalised mass increases very slightly in a nonlinear manner until its stress free position, where the normalised mass is  $\approx 100.2\%$  of its original stress free value. This very small variation in the normalised mass suggests that the principle of conservation of mass has been preserved to some degree despite the use of linearisation.

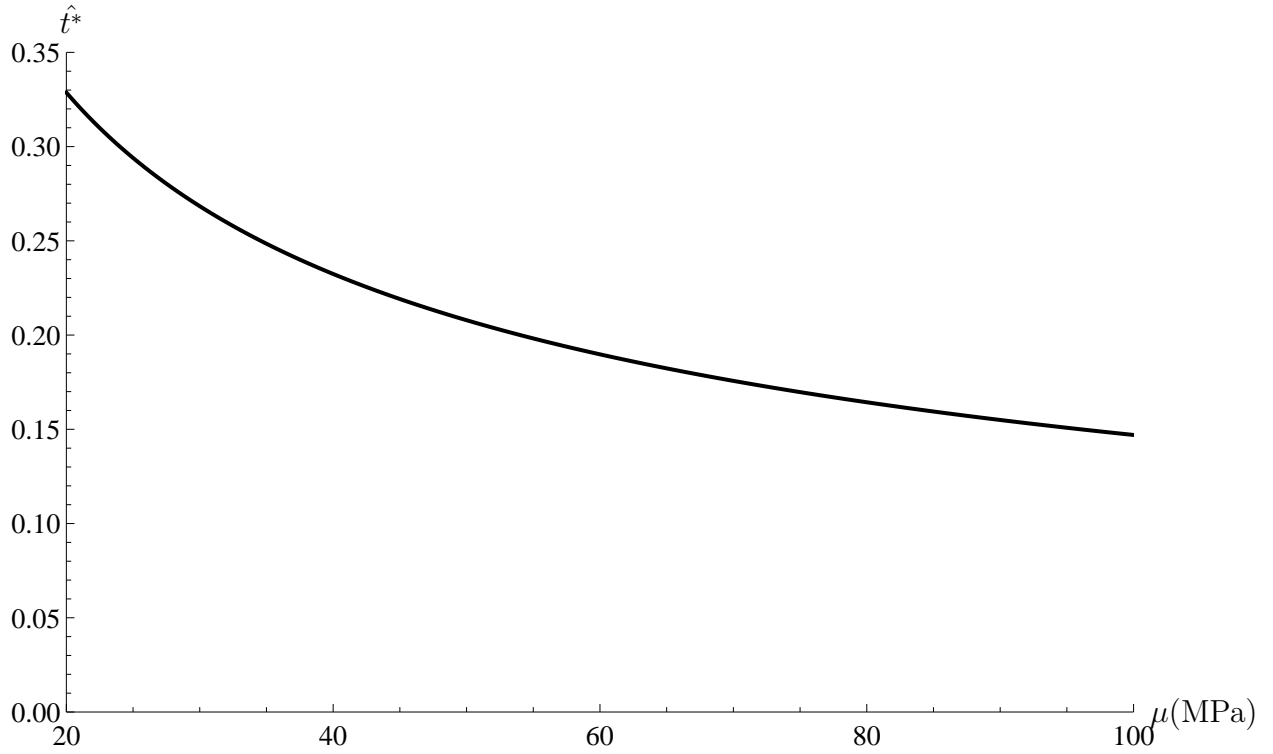


Figure 13: Graph of the normalised collapse time ( $t^*$ ) of the shell versus the shear modulus (stiffness of the shell) for the same stress value of  $p$  where  $\beta = 12$  and an initial stress free thickness of  $Y_O - Y_I = 0.02$ . This is calculated using equations (166),(170),(171) and (172).

Figure 13 highlights the nonlinear relationship between the nondimensionalised collapse time of the shell and its shear modulus. Note that the same magnitude of stress is applied ( $p = 200kPa$ ) to shells with varying shear modulus values resulting in different nondimensionalised values for  $\hat{p}$ . A smaller shear modulus means that the shell is less stiff so, for a fixed initial stress load of  $p$ , shells with a smaller shear modulus will experience larger radial displacements. Shells that have larger radial displacements (for a given fixed initial stress) will take longer to collapse to their initial stress free configurations. Hence as the shear modulus increases there will be a reduction in the radial displacement of the shell resulting



in a faster collapse time.

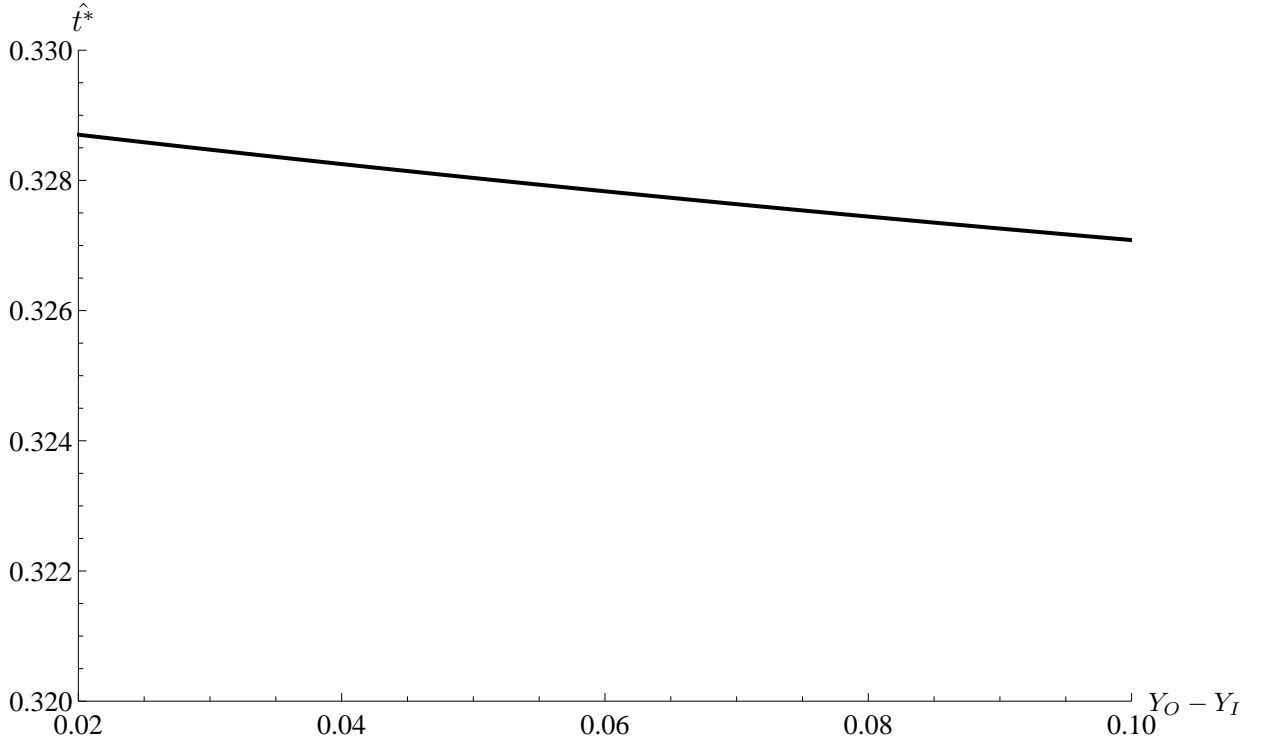


Figure 14: Graph of the normalised collapse time of the shell versus the nondimensionalised original thickness of the shell for an initial nondimensionalised stress load of  $\hat{p} = 0.01$  where  $\beta = 12$  and  $\mu = 20\text{MPa}$ . This is calculated using equations (166),(170),(171) and (172).

Figure 14 shows the nonlinear relationship between the collapse time of the shell and the nondimensionalised original thickness of the shell at its stress free configuration (equilibrium position). Thinner shells will strain more to balance the tensions that they are subjected to which will result in larger radial displacements (this is for a fixed initial stress of  $\hat{p} = 0.01$ ). Larger radial displacements will result in longer collapse times which is highlighted by Figure 14.

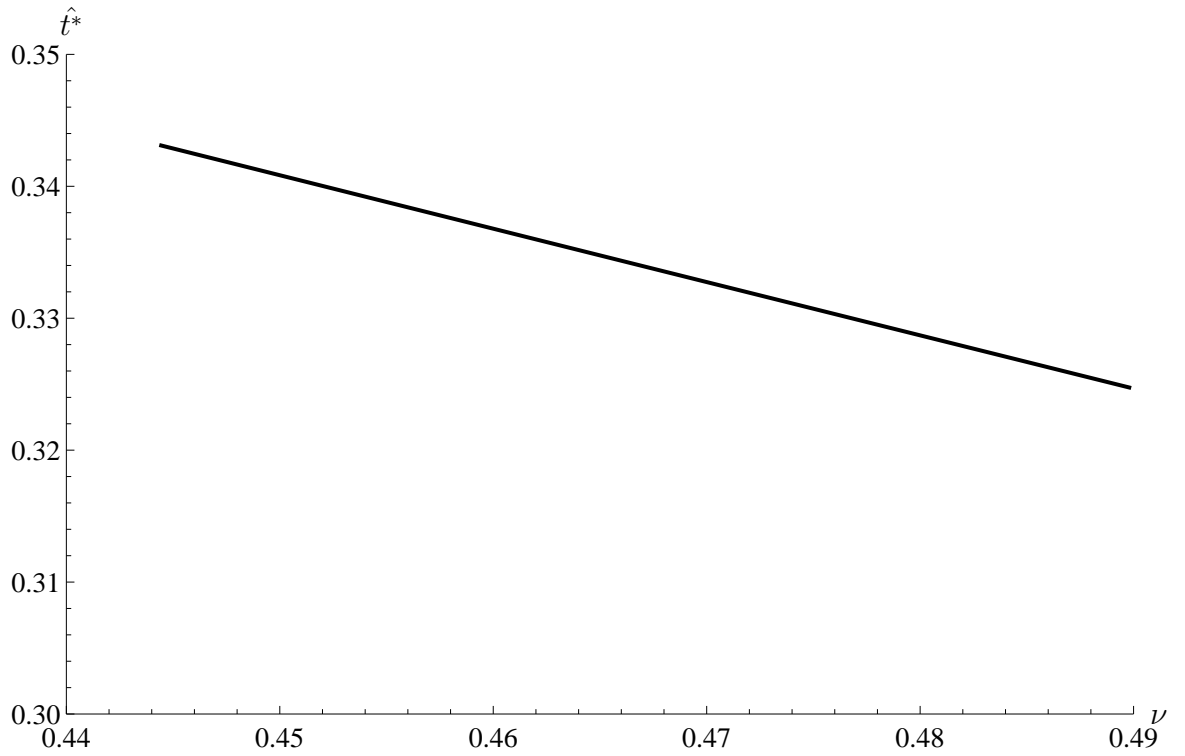


Figure 15: Graph of the normalised collapse time of the shell versus the Poisson ratio of the shell’s material for an initial nondimensionalised stress load of  $\hat{p} = 0.01$  where  $\mu = 20\text{MPa}$  and an initial stress thickness of  $Y_O - Y_I = 0.02$ . This is calculated using equations (166),(170),(171) and (172).

Figure 15 highlights the linear relationship between the nondimensionalised collapse time and Poisson’s ratio for an initial stress of  $\hat{p} = 0.01$ . The Poisson ratio dictates how the material strains in the axial direction relative to the transverse direction [35] and so smaller Poisson ratios will experience larger radial displacements (the shell thins more and by mass conservation the radius increases) for a given initial stress. This in turn results in longer collapse times due to the larger radial displacement. Figure 15 illustrates how the collapse times are lower for an increasing Poisson ratio.

## 9 Conclusion

This section of the study describes an analytical approach to modelling the inflationary process of a shelled microbubble via a quasistatic radially directed stress load applied to its inner surface. The stress load is then switched off (a stress free boundary condition is applied) and the time for the microbubble's shell to collapse back down to its equilibrium position is determined by applying the conservation of momentum and the inflated radial displacement as an initial condition. Key material parameters such as the thickness of the shell, its Poisson ratio and the shell's shear modulus are varied to determine their influence on the collapse phase of the shell. A typical nondimensionalised collapse time for a shell with a shear modulus of  $\mu = 20\text{MPa}$  and a Poisson ratio of  $\nu = 0.48$ , subjected to a nondimensionalised stress load of  $\hat{p} = 0.01$ , is of the order  $\hat{t}^* \approx 0.33$ . Shells with a larger shear modulus possess faster collapse times. As the thickness of the shell increases the collapse time of the shell decreases in a nonlinear manner. Shells with a larger Poisson ratio have smaller initial radial displacements and therefore exhibit faster collapse times. There is a very small error in mass conservation during both the inflationary stage ( $< 0.5\%$ ) and the collapse phase ( $< 0.2\%$ ).

Having used an analytical approach via linearisation to study the collapse of a stressed shelled microbubble then it seems natural to consider a numerical analysis approach.

## 10 Numerical analysis of the collapse of a shelled microbubble

This section discusses the same model of a stressed oscillating shelled microbubble as was discussed in the previously. However, rather than linearising the problem, the full nonlinear equations governing the spatial profiles of the Cauchy radial and angular (hoop) stresses that arise due to the stressing procedure are evaluated numerically by using the technique of finite differences. The history of the microsphere's inflationary path is used to determine the collapse path of the shell as it oscillates about its equilibrium position (stress free configuration). This model assumes that there is no hysteresis in the collapse phase of the shell, which is justified by removing the presence of viscoelastic effects and body forces. By using mass and energy conservation alongside the inflationary history of the shell (the forward picture), a numerical scheme is developed to determine the time taken for the stressed shell to collapse to its stress free configuration. Results are determined from the numerical scheme to show how the shell's thickness, its Poisson ratio and its shear modulus (stiffness of the shell) influences the collapse times of the collapsing shell. This numerical scheme is compared and contrasted with the linearised analytical approach.

## 11 Methodology

### 11.1 Forward picture - Inflating the sphere

The shooting method was used to solve equation (84) ([49],p927). To assist the numerical integration, equations (84),(87) and (88) were nondimensionalised using

the reference configuration's inner radius,  $R_I$ . This was achieved using

$$x(X) = \frac{r(R)}{R_I}, \quad (173)$$

where

$$X = \frac{R}{R_I}, \quad (174)$$

so that

$$X_I = \frac{R_I}{R_I} = 1,$$

and

$$X_O = \frac{R_O}{R_I},$$

such that  $X_I \leq X \leq X_O$ . Calculating the various terms that contribute to (84),

$$r'(R) = \frac{\partial r}{\partial R} = \frac{\partial r}{\partial x} \frac{\partial x}{\partial X} \frac{\partial X}{\partial R} = x'(X), \text{ and} \quad (175)$$

$$\frac{r(R)}{R} = \frac{x(X)}{X}. \quad (176)$$

Calculating the second derivative of the radial displacement gives

$$r''(R) = \frac{\partial}{\partial X} (x'(X)) \frac{\partial X}{\partial R} = \frac{x''(X)}{R_I}. \quad (177)$$

Substituting into equation (84)

$$\begin{aligned} x''(X) \left( (x'(X))^2 \left( \frac{x'(X)x^2(X)}{X^2} \right)^{2\beta} + (1 + 2\beta) \right) = \\ \frac{4\beta x'(X)}{X} - \frac{4\beta (x'(X))^2}{x(X)} + \frac{2x'(X)}{X} - \frac{2(x'(X))^2}{x(X)} \\ + \left( \frac{x'(X)x^2(X)}{X^2} \right)^{2\beta} \left( \frac{2x(X)(x'(X))^2}{X^2} - \frac{2(x'(X))^3}{X} \right). \end{aligned} \quad (178)$$

Nondimensionalising the boundary conditions given by equations (87) and (88) gives

$$(x'(1)(x(1))^2)^{-2\beta} - (x'(1))^2 - \hat{p} (x'(1)(x(1))^2) = 0, \quad \text{since } X_I = 1, \quad (179)$$

and

$$(x'(X_O)) - \left( \frac{X_O}{x(X_O)} \right)^{2\beta/(\beta+1)} = 0, \quad \text{where } \hat{p} = \frac{p}{\mu}. \quad (180)$$

The Cauchy stresses given by equations (91), (92) and (93) are nondimensionalised to give

$$\hat{\tau}_{xx} = \frac{\tau_{xx}}{\mu} = \frac{X^2}{x'(X)x(X)^2} \left( - \left( \frac{x'(X)x(X)^2}{X^2} \right)^{-2\beta} + x'(X)^2 \right), \quad (181)$$

$$\hat{\tau}_{\theta\theta} = \frac{\tau_{\theta\theta}}{\mu} = \frac{X^2}{x'(X)x(X)^2} \left( - \left( \frac{x'(X)x(X)^2}{X^2} \right)^{-2\beta} + \left( \frac{x(X)}{X} \right)^2 \right), \quad \text{and} \quad (182)$$

$$\hat{\tau}_{\phi\phi} = \frac{\tau_{\phi\phi}}{\mu} = \frac{X^2}{x'(X)x(X)^2} \left( - \left( \frac{x'(X)x(X)^2}{X^2} \right)^{-2\beta} + \left( \frac{x(X)}{X} \right)^2 \right). \quad (183)$$

The Cauchy stresses are nondimensionalised using the shear modulus which represents the typical shear modulus of an ultrasound contrast agent. The parameter  $\hat{p}$  allows us to study the influence of the shear modulus on both the inflationary and collapse processes of the shell.

## 11.2 Collapsing the shell of the microbubble

A key component of this study is the influence that the shell material parameters have on the collapse times of the shelled microbubbles. The relevant material parameters include the shear modulus, Poisson's ratio and the reference shell's thickness. The inflationary process maps the behaviour of the Cauchy stresses

and the radial displacement for a given stress applied to the inner surface of the shell. The shell is then collapsed by setting the inner and outer stress loads to zero. The collapsing shell's motion was modelled by applying the linear momentum equation ([45],p149)

$$\rho \frac{\partial v}{\partial t} + \rho (v \cdot \nabla) v = \text{div } \tau, \quad (184)$$

where  $\rho$  represents the density of the shell in the current configuration and  $v$  is the velocity of the shell. Note that (184) here is modelled assuming that there is no viscoelastic effects acting on the shell. The density of the shelled microbubble changes with time due to the compressible nature of the neo-Hookean model (55). The density of the shell at a particular moment in time in the current configuration can be related to its stress free configuration's density,  $\rho_o$ , by  $\rho_o = \rho J$ , where  $J = r'r^2/R^2$  ([45],p87). The Cauchy stresses in the radial and angular directions are dependent solely on the radial displacement, the reference configuration's coordinates, the material parameters and the derivative of the radial displacement with respect to the reference configuration's radial coordinates. The Cauchy stresses exhibit no angular dependency in this model. The radial Cauchy stress is compressive but the Cauchy angular (hoop) stresses represent a stretch in the material. The resulting sign conventions are negative and positive respectively. The divergence of the Cauchy stress is evaluated with respect to the displacement  $r(R)$  and is written as  $\text{div } \tau$ . The Cauchy stress is defined in terms of the current configuration.  $\text{div } \tau$  is nondimensionalised using equation (173) to give a dimensionless stress term that scales with the shear modulus. The stress,  $\text{div } \tau$ , which causes the shell to collapse is evaluated by making all the stresses in the forward picture (132) compressive in nature. This gives

$$\text{div } \tau = \frac{\mu}{R_I} \left( \left( -\frac{\partial \hat{\tau}_{xx}}{\partial X} \right) \frac{1}{(\partial x / \partial X)} + \frac{2}{x} (\hat{\tau}_{xx} - \hat{\tau}_{\theta\theta}) \right) e_r. \quad (185)$$

Nondimensionalising the left hand side of equation (184) gives

$$\begin{aligned} & \rho \frac{\partial v}{\partial t} + \rho (v \cdot \nabla) v \\ &= \left( \frac{\rho_o R_I}{\gamma^2} \left( \frac{X^2}{x^2 (\partial x / \partial X)} \right) \frac{\partial^2 x}{\partial \hat{t}^2} + \frac{\rho_o R_I}{\gamma^2} \left( \frac{X^2}{x^2 (\partial x / \partial X)} \right) \left( \frac{\partial x}{\partial \hat{t}} \frac{\partial}{\partial x_i} \right) \frac{\partial x}{\partial \hat{t}} \right) e_r, \end{aligned} \quad (186)$$

where  $\hat{t}$  is the dimensionless time parameter given by  $t = \gamma \hat{t}$ . Equating equations (185) and (186) via equation (184) gives

$$\begin{aligned} & \frac{\rho_o R_I}{\gamma^2} \left( \frac{X^2}{x^2 (\partial x / \partial X)} \right) \frac{\partial^2 x}{\partial \hat{t}^2} + \frac{\rho_o R_I}{\gamma^2} \left( \frac{X^2}{x^2 (\partial x / \partial X)} \right) \left( \frac{\partial x}{\partial \hat{t}} \frac{\partial}{\partial x_i} \right) \frac{\partial x}{\partial \hat{t}} \\ &= \frac{\mu}{R_I} \left( \left( -\frac{\partial \hat{\tau}_{xx}}{\partial X} \right) \frac{1}{(\partial x / \partial X)} + \frac{2}{x} (\hat{\tau}_{xx} - \hat{\tau}_{\theta\theta}) \right), \end{aligned} \quad (187)$$

where equation (187) gives a definition for  $\gamma$  as

$$\gamma = \sqrt{\frac{\rho_o R_I^2}{\mu}}. \quad (188)$$

This reduces to

$$\frac{\partial^2 x}{\partial \hat{t}^2} + \left( \frac{\partial x}{\partial \hat{t}} \frac{\partial}{\nabla x_i} \right) \frac{\partial x}{\partial \hat{t}} = \left( \frac{x}{X} \right)^2 \left( -\frac{\partial \hat{\tau}_{xx}}{\partial X} \right) + \frac{2x}{X^2} (\hat{\tau}_{xx} - \hat{\tau}_{\theta\theta}) \left( \frac{\partial x}{\partial X} \right). \quad (189)$$

Equations (178) to (183) are solved numerically using Mathematica [49]. The solutions are presented in the form of an interpolating polynomial. This interpolating polynomial is used to determine a table of values for  $\text{div } \hat{\tau}$  incremented between  $x_I$  and  $x_O$  over  $Nx$ . The technique of finite differences is used to solve equation (189). A backward time difference is used to determine the velocity in  $(v \cdot \nabla)v$  and a central difference is used for the spatial domain. Substituting into equation



(184) gives

$$x_j^{(i+1)} = 2x_{(j)}^{(i)} - x_{(j)}^{(i-1)} - (\delta\hat{t})^2 \left(\frac{x}{X}\right)^2 \frac{\partial\hat{\tau}_{xx}}{\partial X} + 2(\delta\hat{t})^2 \left(\frac{x}{X^2}\right) (\hat{\tau}_{xx} - \hat{\tau}_{\theta\theta}) \frac{\partial x}{\partial X} - \frac{1}{2\delta x} \left(x_{(j)}^{(i)} - x_{(j)}^{(i-1)}\right) \left(x_{(j+1)}^{(i)} - x_{(j+1)}^{(i-1)} - x_{(j-1)}^{(i)} + x_{(j-1)}^{(i-1)}\right) \quad (190)$$

where the  $i$  and  $j$  represent the nondimensionalised time and spatial steps respectively and  $\delta\hat{t}$  and  $\delta x$  represent the magnitudes of the time and spatial steps. The initial conditions are given by

$$\frac{\partial x(X, \hat{t})}{\partial \hat{t}} = 0, \text{ at } \hat{t} = 0, \forall \hat{X},$$

which is equivalent to

$$x^{(1)}(X) = x^{(2)}(X), \forall X \in [X_I, X_O] \quad (191)$$

with the other initial condition being

$$x(X) = X, \text{ at } \hat{t} = 0, \forall X$$

which can be rewritten as

$$x^{(1)}(X) = X, \forall X \in [X_I, X_O]. \quad (192)$$

The finite difference equation (190) was solved for the initial conditions given by (191) and (192). The finite difference equation has two boundary conditions that are defined by the Cauchy radial stress at the inner and outer radius of the shell. The Cauchy radial stress is normal to the shell's surface and is equated to zero to collapse the shelled microbubble. The Cauchy angular (hoop) stresses are radially

dependent but are tangential to the surface. Using equation (181) gives

$$\hat{\tau}_{xx} = \frac{X^2}{x'(X)x(X)^2} \left( - \left( \frac{x'(X)x(X)^2}{X^2} \right)^{-2\beta} + x'(X)^2 \right) = 0$$

and rearranging leads to

$$x' = \left( \frac{x}{X} \right)^{-2\beta/(\beta+1)}. \quad (193)$$

Expressing equation (193) in terms of the boundary conditions at the inner and outer radius results in

$$x_{(0)}^{(i)} = x_{(1)}^{(i)} - \delta x \left( \frac{x_{(1)}^{(i)}}{X_{(1)}} \right)^{-2\beta/(\beta+1)}, \quad (194)$$

$$x_{(N+1)}^{(i)} = x_{(N)}^{(i)} + \delta x \left( \frac{x_{(N)}^{(i)}}{X_{(N)}} \right)^{-2\beta/(\beta+1)}, \quad (195)$$

where 1 and  $N$  refer to the spatial steps for the inner and outer radii respectively. Equations (194), (195) are combined with equation (190) to give the finite difference algorithms at the inner and outer radii.

## 12 Results and Discussion

This section focusses on the results for the numerical solution. For the inflationary process (11.1), the Cauchy stresses were plotted against the nondimensionalised radial displacement of the inner shell surface. In addition, the behaviour of the displacement versus the nondimensionalised reference configuration's radial coordinates,  $x$ , was analysed for varying shell thicknesses. Also the shell thickness versus the stress load applied to the inner surface of the shell was considered for various Poisson's ratios. This procedure was carried out on shell thicknesses that were of the order of 0.2% of the shelled microbubble's radius (that is  $x_O = 0.002$ )

which can be typical for ultrasound contrast agents [12]. Analysing how the applied stress load on the inner shell surface evolved with the displacement also enables us to test for the presence of plasticity. This procedure was performed for several different Poisson's ratios. The collapse time was evaluated versus the shear modulus for two different Poisson's ratios and different values of shell thickness. In addition, the collapse time of the shell versus various Poisson's ratios was evaluated for different shell thicknesses.

## 12.1 Inflation of the shelled microbubble

By solving the inflating shelled microbubble equations given by equations (178) to (180) for different internal stress loads ( $\hat{p}$ ), the effect on the shell displacement can be determined.

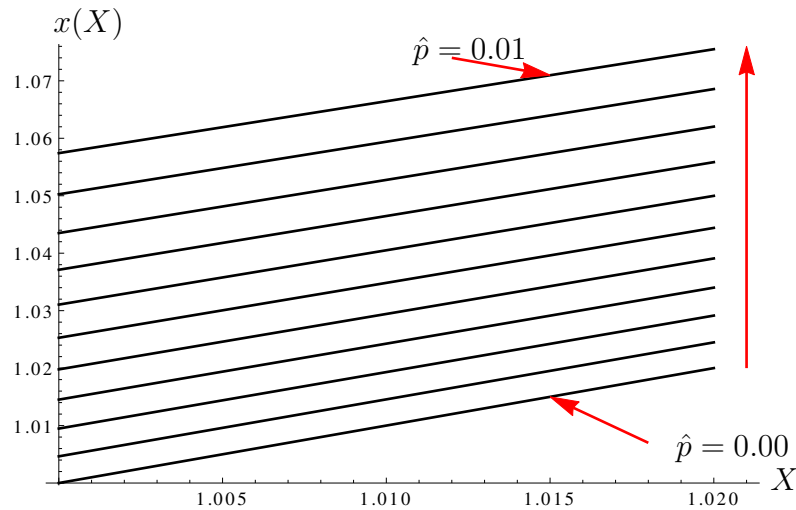


Figure 16: Graph of the nondimensionalised radial displacement versus the nondimensionalised reference configuration's radial coordinates for different internal stress loads  $\hat{p} = 0, 0.001, 0.002, \dots, 0.01$  where  $\nu = 0.48$ ,  $\beta = 12$  and the initial thickness is  $X_O - X_I = 0.02$ . This is calculated using equations (178),(179) and (180)

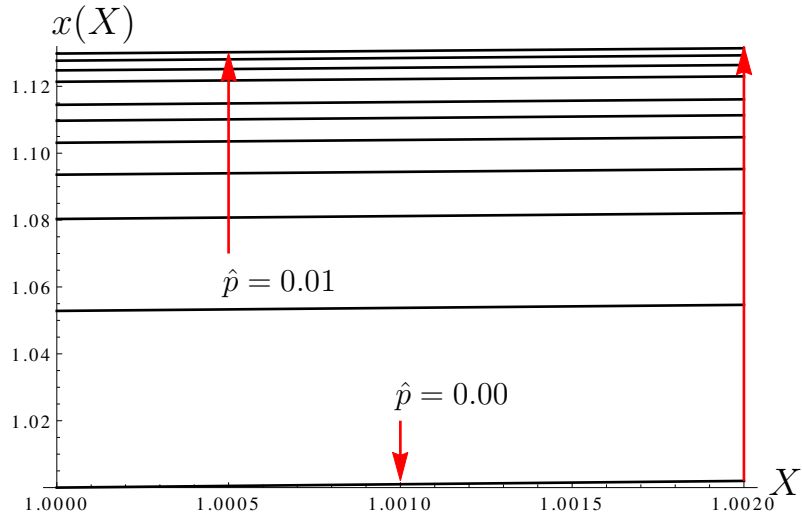


Figure 17: Graph of the nondimensionalised radial displacement versus the nondimensionalised reference configuration's radial coordinates for different internal stress loads  $\hat{p} = 0, 0.001, 0.002, \dots, 0.01$  where  $\nu = 0.48$ ,  $\beta = 12$  and initial thickness  $X_O - X_I = 0.002$ . This is calculated using equations (178),(179) and (180)

Figures 16 and 17 show the effect on the radial displacement of the shell for a series of stress loads with shells of initial thickness  $X_O - X_I = 0.02$  and  $X_O - X_I = 0.002$  respectively. Decreasing the shell's thickness from  $X_O - X_I = 0.02$  to  $X_O - X_I = 0.002$  results in a greater radial displacement for the shelled microbubbles as illustrated by Figures 16 and 17. The greater radial displacement for the thinner shell is due to thinner shells requiring a greater strain in order to achieve the stresses required to balance with the applied stress load. Note that when no stress load is applied ( $\hat{p} = 0$ ) then  $x(X) = X$  which is the trivial solution satisfying equations (178) to (180) as  $x(1) = 1$ ,  $x'(X) = 1$  and  $x(X_O) = X_O$ . The vertical red lines in Figures 16 and 17 highlight the direction of the increasing stress loads  $\hat{p}$ .

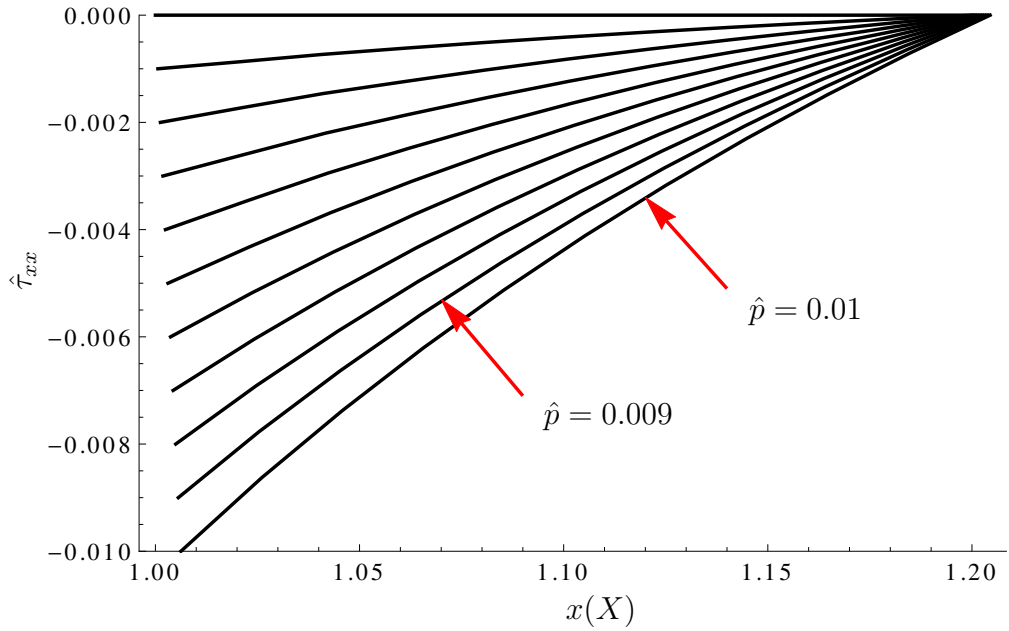


Figure 18: Graph of the nondimensionalised Cauchy radial stresses against their nondimensionalised radial displacement for different internal stress loads  $\hat{p} = 0, 0.001, 0.002, \dots, 0.01$  where  $\nu = 0.48$ ,  $\beta = 12$  and initial thickness  $X_O - X_I = 0.2$ . This is calculated using equations (178),(179),(180) and (181).

Figure 18 illustrates the behaviour of the nondimensionalised Cauchy radial stresses for the spherical inflation of a shelled microbubble. The reference shell's thickness for Figure 18 was chosen because of its visual presentation. Choosing a thinner reference shell would produce a greater radial displacement and, therefore, a less visually appealing image. Note that these curves are stored as interpolating polynomials which greatly assists in their later usage in the deflating shelled microbubble problem. Each curve arises from a specific stress load applied to the inner surface of the shell. The negative values imply that the shell is being compressed as the stress load increases. It can also be seen that the largest compression occurs at the inner surface of the spherical shell. The gradients of the curves are positive and increase in magnitude as the stress load increases. Figure 18 represents a thick shelled microbubble with an initial thickness of  $X_O - X_I = 0.2$ .

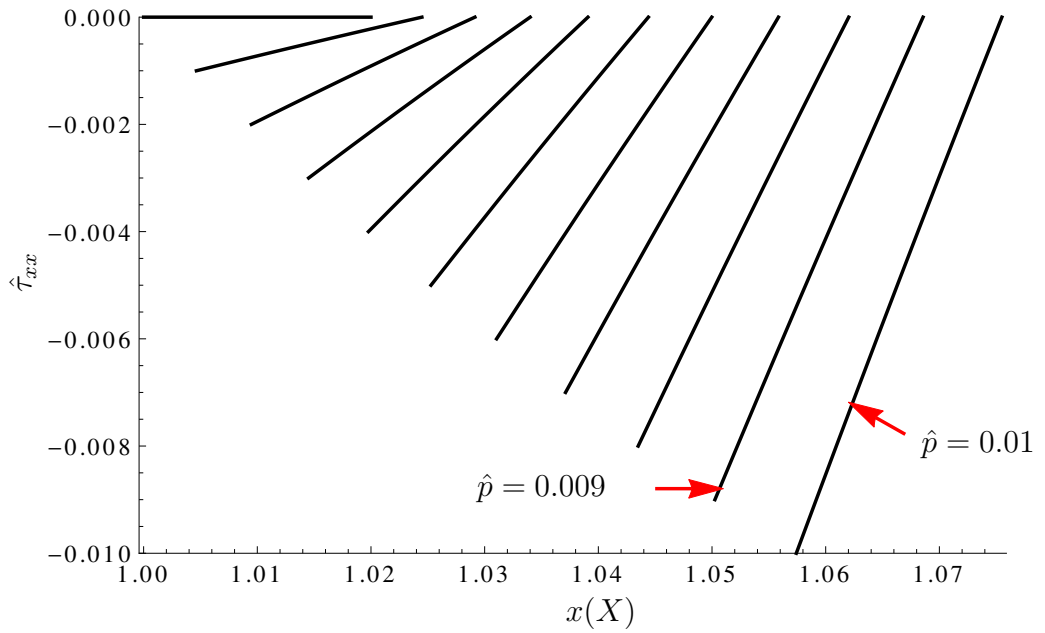


Figure 19: Graph of the nondimensionalised Cauchy radial stresses against their nondimensionalised radial displacement for different internal stress loads  $\hat{p} = 0, 0.001, 0.002, \dots, 0.01$  where  $\nu = 0.48$ ,  $\beta = 12$  and initial thickness  $X_O - X_I = 0.02$ . This is calculated using equations (178),(179),(180) and (181).

Thinning the shell's initial thickness to  $X_O - X_I = 0.02$  results in plots that exhibit steeper positive gradients and greater radial displacements as shown in Figure 19.

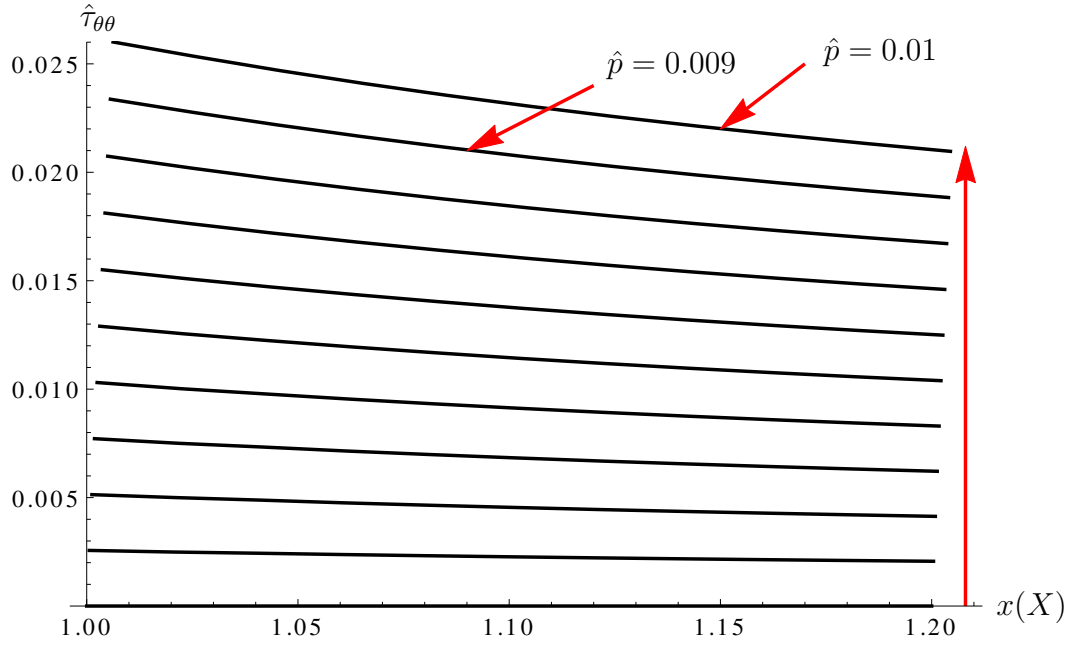


Figure 20: Graph of the nondimensionalised Cauchy angular stresses against their nondimensionalised radial displacement for different internal stress loads  $\hat{p} = 0, 0.001, 0.002, \dots, 0.01$  where  $\nu = 0.48$ ,  $\beta = 12$  and initial thickness  $X_O - X_I = 0.2$ . This is calculated using equations (178),(179),(180) and (182).

Figure 20 illustrates the radial dependence of the Cauchy angular (hoop) stress  $\hat{\tau}_{\theta\theta}$  for an initial shell thickness of  $X_O - X_I = 0.2$ . The graph for the angular stress  $\hat{\tau}_{\phi\phi}$  is identical to Figure 20 since the stress is produced using a spherically symmetric inflationary process. The angular Cauchy stresses are positive in value which means that the material is experiencing a stretching effect in the angular direction. The gradient for each curve is negative with the material at the inner radius possessing a greater Cauchy stress value (stretch) than that at the outer radius. The vertical red line in Figures 20 highlights the direction of the increasing stress steps  $\hat{p}$ .

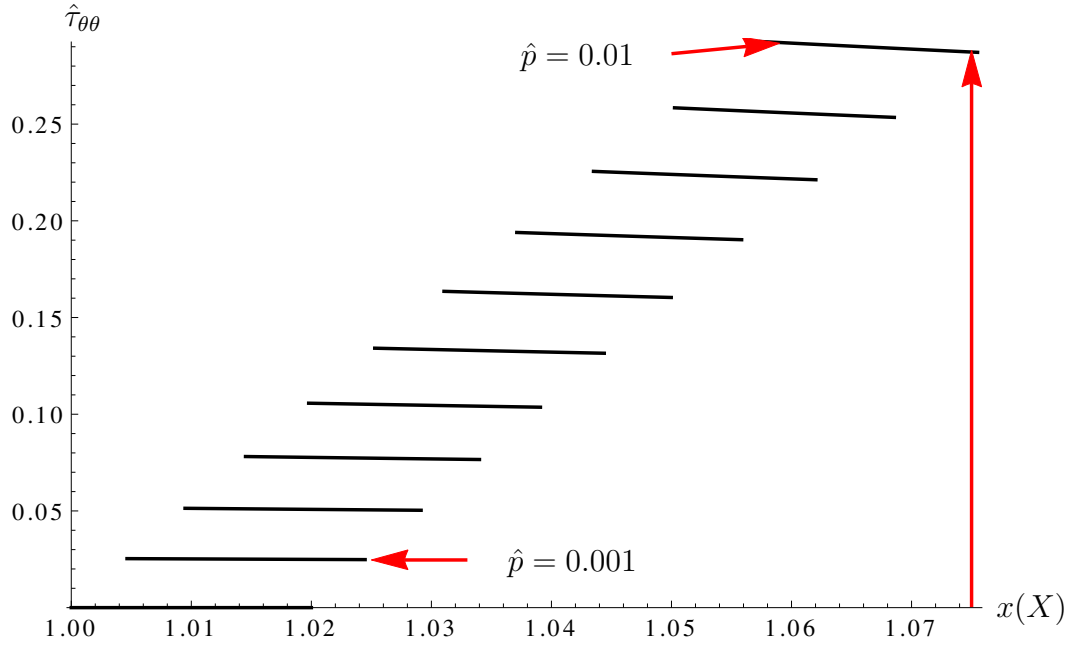
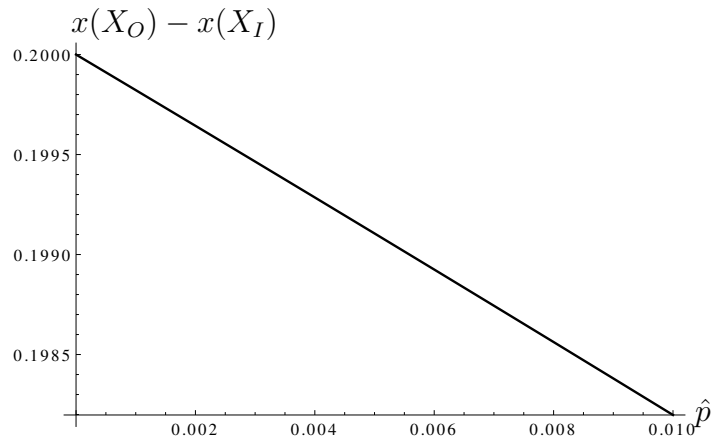


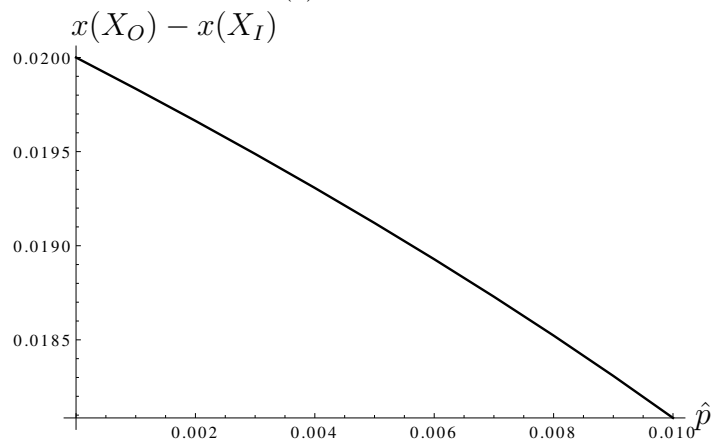
Figure 21: Graph of the nondimensionalised Cauchy angular stresses against their nondimensionalised radial displacement for different internal stress loads  $\hat{p} = 0, 0.001, 0.002, \dots, 0.01$  where  $\nu = 0.48$ ,  $\beta = 12$  and initial thickness  $X_O - X_I = 0.02$ . This is calculated using equations (178),(179),(180) and (182).

Figure 21 shows the nondimensionalised Cauchy angular stress  $\hat{\tau}_{\theta\theta}$  for an initial shell thickness of  $X_O - X_I = 0.02$ . Figure 21 illustrates a nondimensionalised Cauchy angular stress that is positive indicating a stretching behaviour that is similar to Figure 20. The Cauchy angular stress in Figure 21 is larger in size than the Cauchy angular stress in Figure 20. The slope of the nondimensionalised Cauchy angular stress versus the nondimensionalised radial displacement is almost flat, indicating that its gradient is almost zero. Figures 20 and 21 indicate that reducing the thickness of the shell increases the size of the Cauchy angular stresses and the radial displacement of the shelled microbubble. The vertical red line in Figures 21 highlights the direction of the increasing stress steps  $\hat{p}$ .

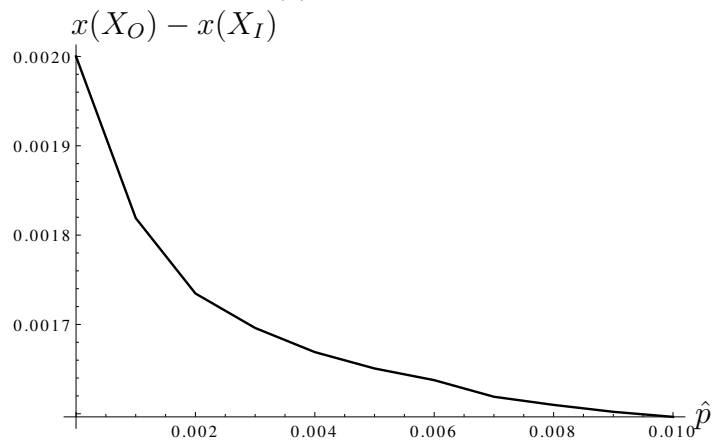




(a)  $X_O = 1.2$



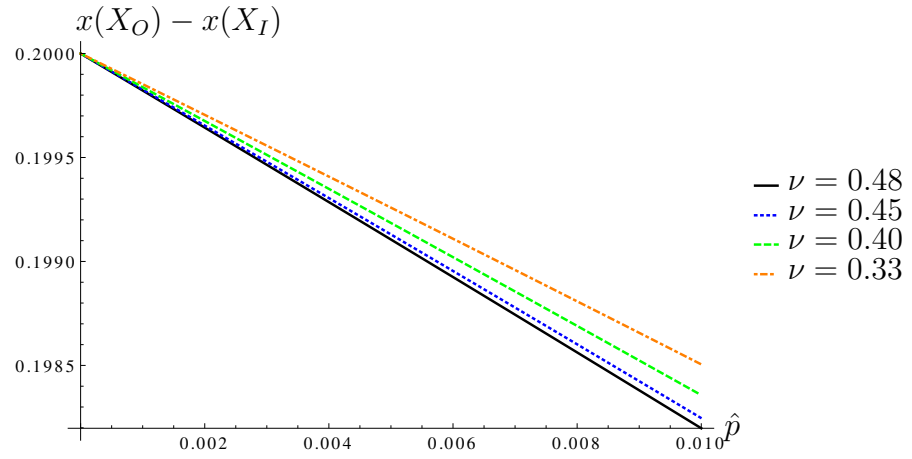
(b)  $X_O = 1.02$



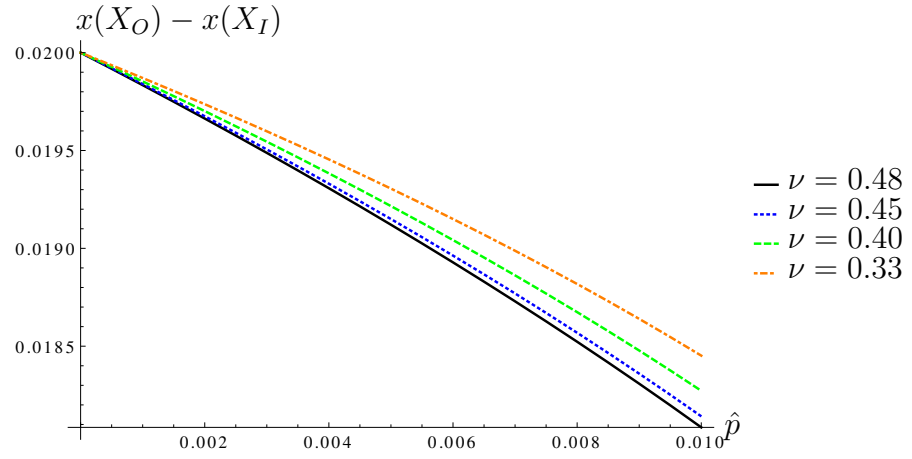
(c)  $X_O = 1.002$

Figure 22: Graph of the shell's nondimensionalised thickness versus the nondimensionalised stress load for different internal stress loads  $\hat{p} = 0, 0.001, 0.002, \dots, 0.01$  where  $\nu = 0.48$ ,  $\beta = 12$  and initial thickness  $X_O - X_I = 0.02$ . This is calculated using equations (178),(179) and (180).

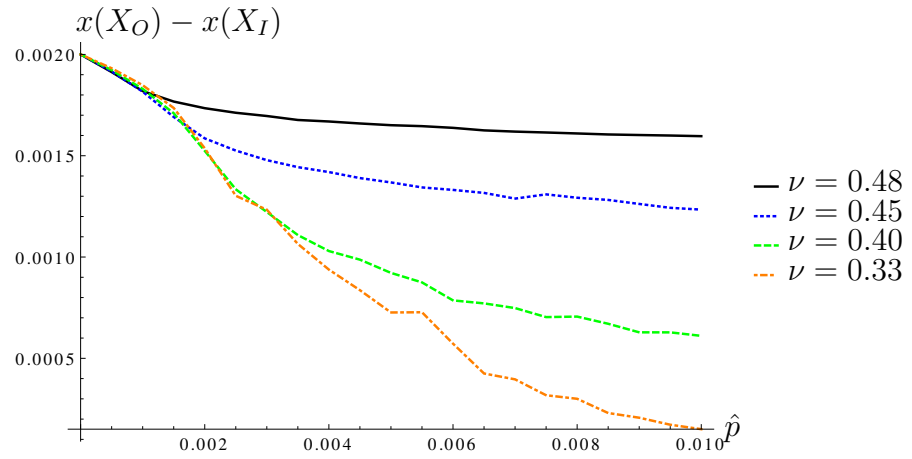
Figure 22(a) illustrates the behaviour of the shell's thickness with increasing stress load. It can be seen that as the load increases the inner radius increases and the thickness of the shell decreases. It can also be observed that the graph for a thick shelled microbubble is linear. Thinning the shell's initial thickness down to  $X_O - X_I = 0.02$  and  $X_O - X_I = 0.002$  results in nonlinear behaviour as illustrated by Figures 22(b) and 22(c) respectively. The reduction in shell thickness is due to the shell being displaced further in the radial direction due to an increasing stress load on its inner surface.



(a)  $X_O = 1.2$



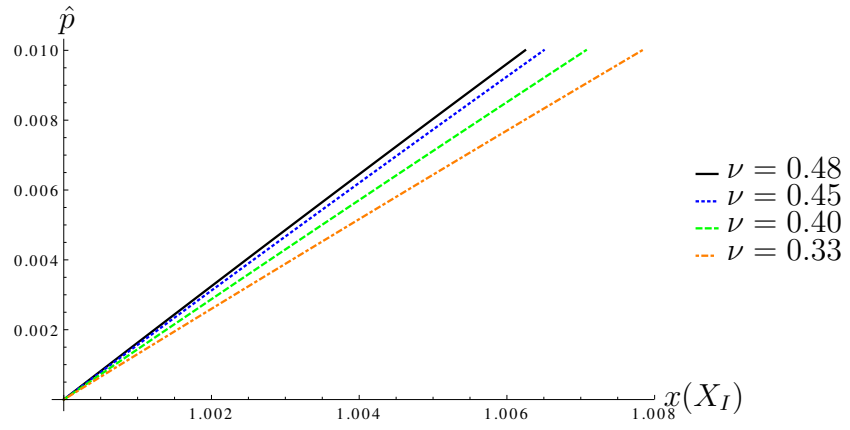
(b)  $X_O = 1.02$



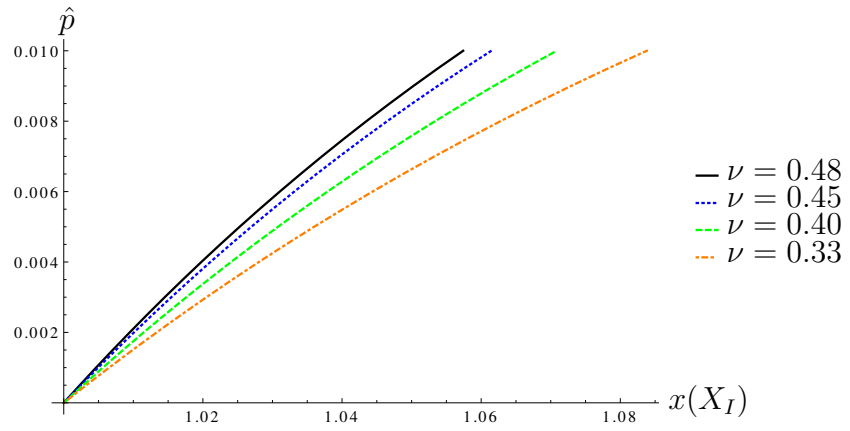
(c)  $X_O = 1.002$

Figure 23: Plots of the nondimensionalised shell thickness versus the nondimensionalised stress load for different internal stress loads  $\hat{p} = 0, 0.001, 0.002, \dots, 0.01$  and various Poisson ratios. This is calculated using equations (178),(179) and (180).

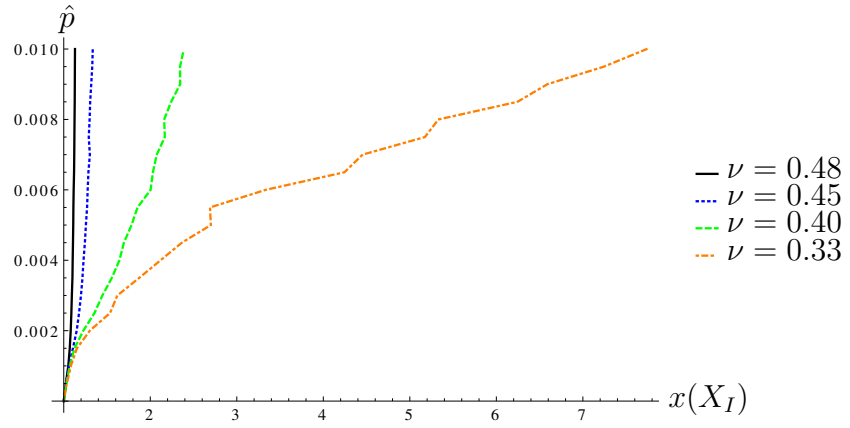
Figure 23 highlights how the thickness of the shell evolves with increasing stress loads applied to the inner radius of the shelled microbubble for several different Poisson ratios. For an initial shell thickness of  $X_O - X_I = 0.2$ , as shown in Figure 23(a), the variation of the shell's thickness with the stress load is linear in nature with the change in Poisson's ratio having a marginal effect. The gradient of the graph is negative because as the stress load increases the shell is displaced radially outwards resulting in a thinner shell. Thin shells illustrated by Figures 23(b) and 23(c) display nonlinear behaviour and a marked dependency on the shell's material parameters. Very thin shelled microbubbles with initial thicknesses of the order of  $X_O - X_I = 0.002$ , experience a more complex and nonlinear trend. For small stress loads the behaviour is essentially linear but at a critical value of this load (dependent on the Poisson's ratio), the shell undergoes a dramatic increase in its radius for only a small rise in the applied stress load.



(a)  $X_O = 1.2$



(b)  $X_O = 1.02$

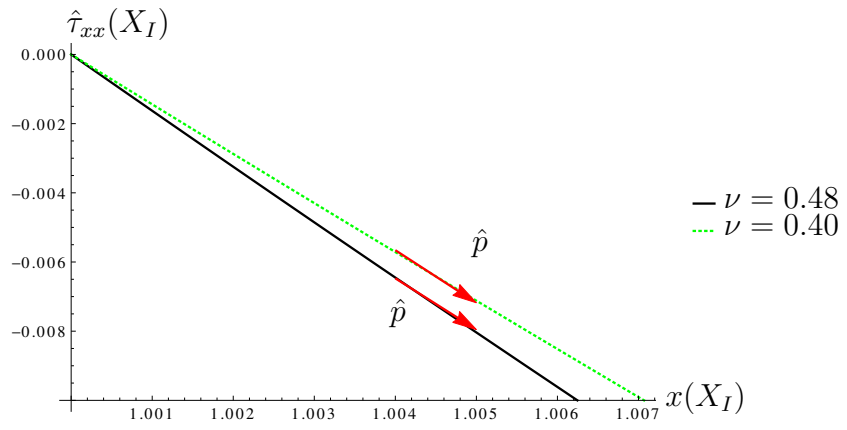


(c)  $X_O = 1.002$

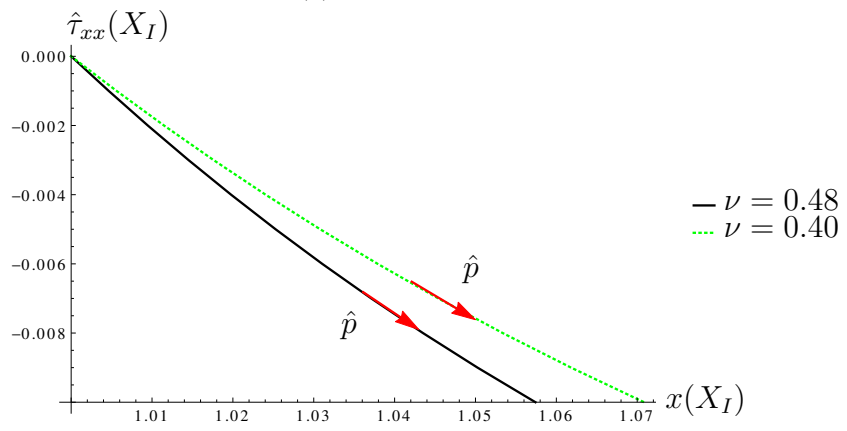
Figure 24: Plots of the nondimensionalised stress load versus the nondimensionalised inner radial displacement for different internal stress loads  $\hat{p} = 0, 0.001, 0.002, \dots, 0.01$  and various Poisson ratios. This is calculated using equations (178),(179) and (180).

To illustrate this further Figure 24 charts the behaviour of the nondimensionalised stress load versus the nondimensionalised inner radius for various shell thicknesses and several different Poisson ratios. The axes are chosen here to aid interpretation as it can be viewed as a stress-strain plot. As before, Figure 24(a) displays linear behaviour whereas Figures 24(b) and 24(c) are nonlinear in nature. For relatively thick shells such as those illustrated by Figures 24(a) and 24(b), shelled microbubbles with greater Poisson's ratio exhibit a steeper positive gradient and hence a reduced magnitude in the radial displacement. As anticipated, the greatest radial displacement is illustrated by Figure 24(c) for very thin shelled microbubbles.

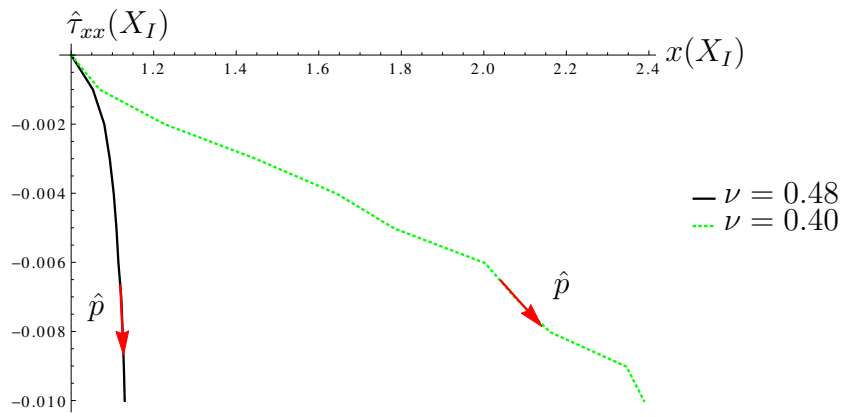
Figure 25(a) highlights how the results above then dictate how the Cauchy stresses within the shell, as given by equations (181) to (183), is affected by changes to the Poisson ratio. The Cauchy radial stress at the inner surface of the shell versus the nondimensionalised inner radius ( $x(X_I)$ ) behaves linearly as the stress load ( $\hat{p}$ ) increases with the change in the Poisson ratio having a marginal effect. Figure 25(b) characterises the behaviour of a microbubble with an intermediate shell thickness of  $X_O - X_I = 0.02$ . The Cauchy radial stress at the inner shell surface begins to display nonlinear behaviour. Figure 25(c) illustrates the case of a thin shelled microbubble ( $X_O - X_I = 0.002$ ) with the typical dimensions of an ultrasound contrast agent [12]. In all cases the smaller Poisson ratio experiences a significantly larger radial displacement. For a large Poisson ratio, the Cauchy radial stress grows more steeply in the negative direction over a much smaller increment in the stress load in comparison to the smaller Poisson ratio. This becomes quite extreme in Figure 25(c) for the thin shelled microbubble.



(a)  $X_O = 1.2$



(b)  $X_O = 1.02$



(c)  $X_O = 1.002$

Figure 25: Plots of the nondimensionalised Cauchy radial stresses at their inner radius versus the nondimensionalised inner radius for different internal stress loads  $\hat{p} = 0, 0.001, 0.002, \dots, 0.01$ . This is calculated using equations (178),(179), (180) and (181).

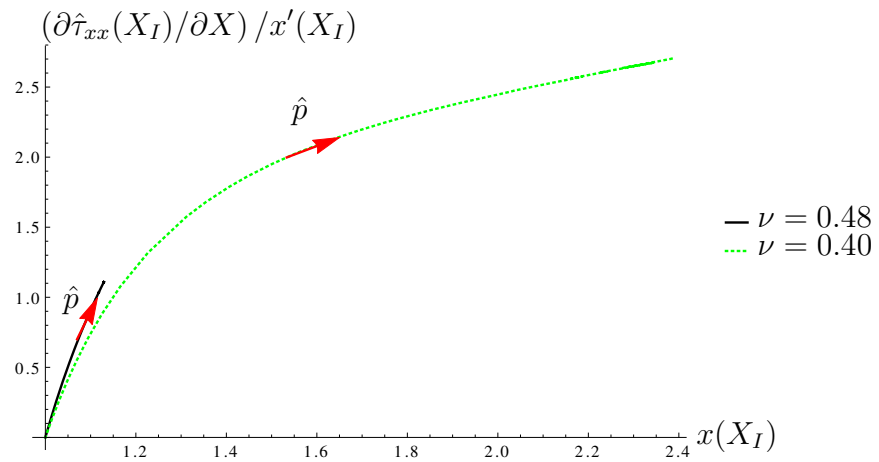
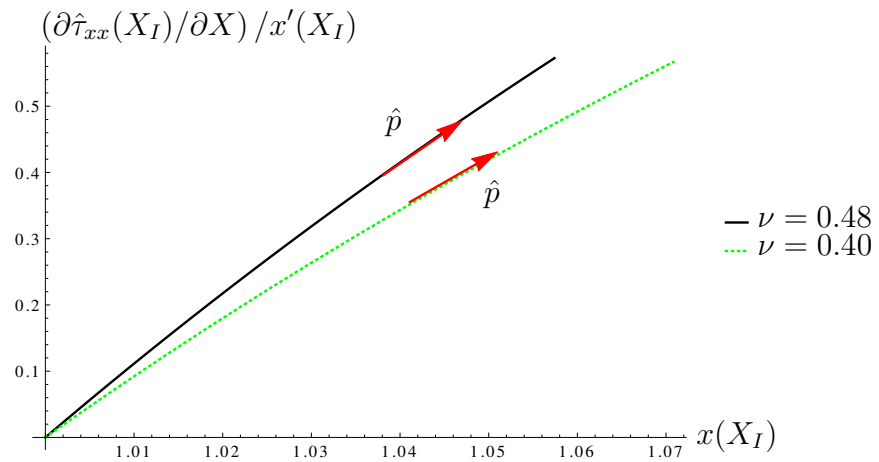
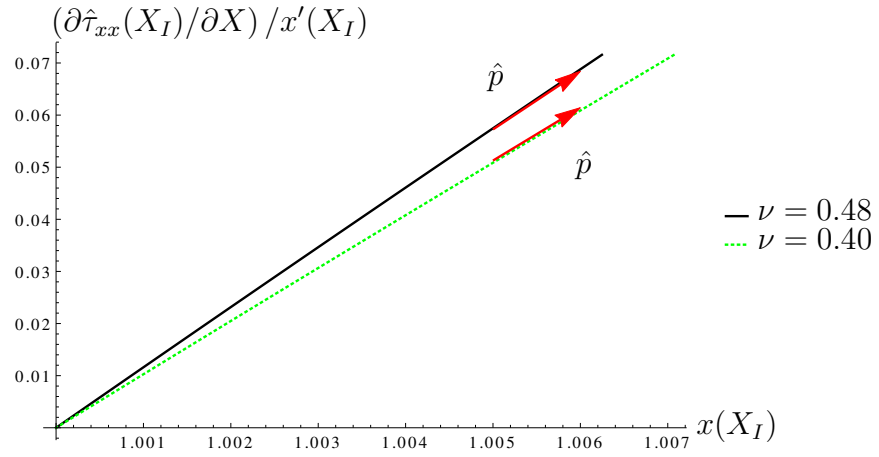


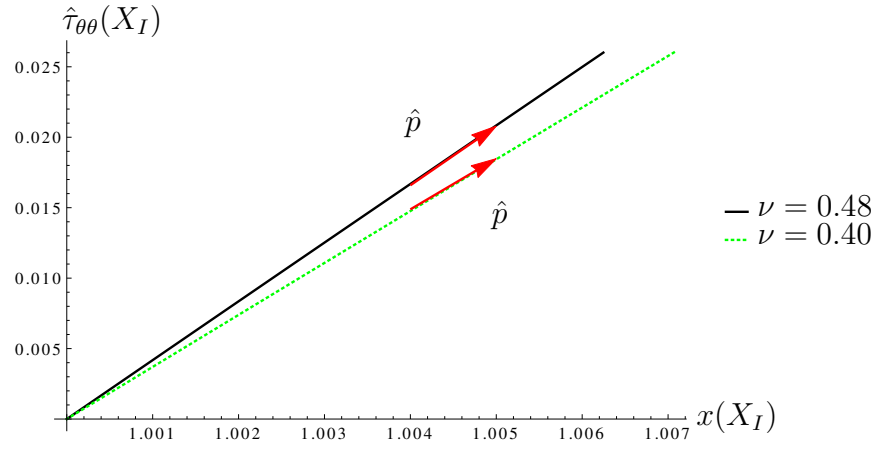
Figure 26: The nondimensionalised derivative of the Cauchy radial stress versus successive nondimensionalised inner radii for different internal stress loads  $\hat{p} = 0, 0.001, 0.002, \dots, 0.01$ . This is calculated using equations (178),(179), (180) and (181).



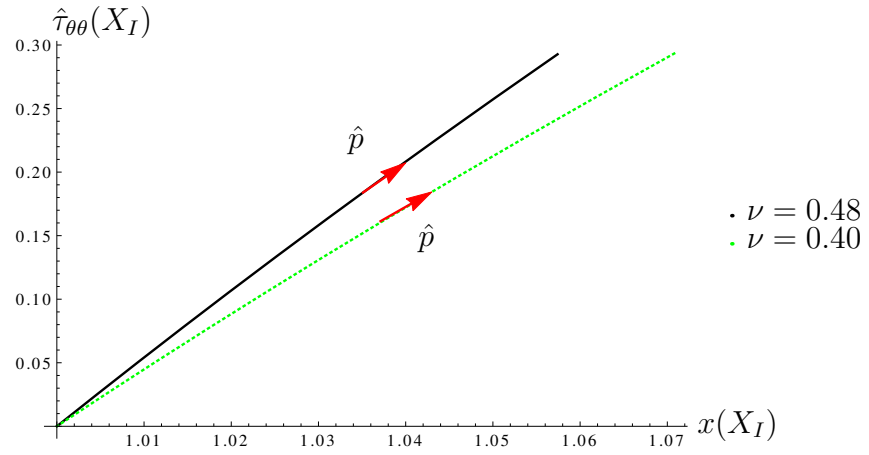
Figure 26 shows how the nondimensionalised derivative of the Cauchy radial stress at the inner surface of the shell behaves in relation to the inner radius for different shell thicknesses. Since the Cauchy stresses are stored as interpolating polynomials then the calculation of these derivatives is straightforward and well-posed. Figure 26(a) shows the linear behaviour of the nondimensionalised derivative of the Cauchy radial stress with the nondimensionalised inner radius for an increasing stress load at the inner surface of the shelled microbubble. The larger Poisson ratio has the larger, positive slope. Figure 26(b) displays nonlinear characteristics, with the larger Poisson ratio possessing the steeper gradient. Figure 26(c) highlights the behaviour of a thin shelled microbubble. A large radial displacement occurs for the smaller Poisson ratio and the derivative of the Cauchy radial stress behaves nonlinearly, growing at a decreasing rate until it reaches a maximum value and then decreasing slowly with increasing inner radius. These derivatives are also stored as interpolating polynomials to ensure that the numerical treatment of the collapsing microbubble, as given by equations (190) to (192), is both straightforward to implement and leads to a well-posed solution method.

A similar treatment can be given to the angular stress. As before, Figure 27(a) illustrates linear behaviour with the larger Poisson ratio possessing the larger increase in Cauchy angular stress. Figures 27(b) and 27(c) illustrate nonlinear behaviour with the larger Poisson ratios exhibiting the greater increase in Cauchy angular stress. The radial displacement for Figure 27(c) for the smaller Poisson ratio is significantly larger than the radial displacement for the larger Poisson ratio value of  $\nu = 0.48$ . For the shelled microbubble to rupture the stresses within its shell must exceed the tensile stress of the shell material. Given the significantly higher stresses exhibited by the angular (hoop) stress, and given that it is a stretch

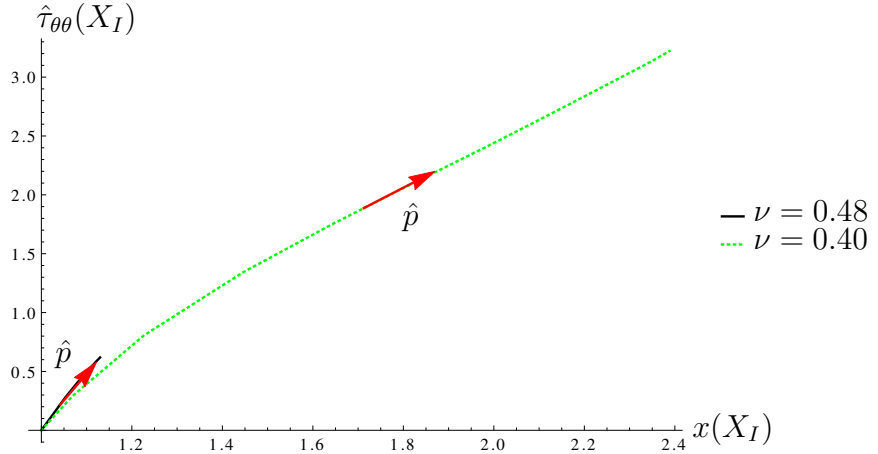
(as opposed to the compressive nature of the radial stress), then it is this stress that will lead to shell rupture (compare the values in Figure 27(c) with those in Figure 25(c)).



(a)  $X_O = 1.2$



(b)  $X_O = 1.02$



(c)  $X_O = 1.002$

Figure 27: Plots of the nondimensionalised Cauchy angular stress versus the nondimensionalised inner radius for different internal stress loads  $\hat{p} = 0, 0.001, 0.002, \dots, 0.01$ . This is calculated using equations (178), (179), (180) and (182).

## 12.2 Collapsing the shell

The stressing of the shell, achieved by applying a radially directed stress load at the inner surface of the shelled microbubble, results in a significant displacement of the shelled microbubble which can be collapsed back to its original stress free configuration by switching off this stress load. This assumes that there is no potential energy dissipated in the stressed shell during this switching off of the stress load. The following model for collapsing the shell assumes that the shell's stresses are given by those calculated above when the shelled microbubble was being inflated. For a given internal stress load the spatial dependency of the Cauchy stresses within the shell were recorded as well as values of the inner and outer radii. As the shelled microbubble collapses the inner and outer radius of its shell are used to interpolate within these Cauchy stress profiles and hence determine the stresses within the shell at that stage in its collapse. The model does not therefore take account of possible alternative histories or hysteresis effects and naively assumes only one possible collapse path. This model that will enable an investigation into the effects of the shell's material parameters on the collapse times. An initially stress free shell is inflated using an applied stress  $\hat{p}$ . The stressed shelled microbubble is collapsed by setting the stress load at the inner radius to zero. This matches the stress load on the outer radius of the shelled microbubble. This stressed shell is then subjected to the stress free model given by equations (178) to (180) and allowed to evolve in time until the original stress free shell is recovered. The stress free configuration is defined as the point where  $\nabla_x \cdot \tau = 0$  which should occur when  $x(X_I, \hat{t}) = 1$ . This will coincide with the shell's inner and outer radii reducing to the original values of  $X_I$  and  $X_O$  provided there is no hysteresis present in the system. Neo-Hookean systems that don't possess viscoelasticity will not exhibit hysteresis effects ([45],p221). Any shortfall

in the final thickness of the shell will be due to rounding and discretisation errors in the finite difference scheme. Note that the forward picture or the inflationary process is a differential equation with no time evolution but the collapse phase is now a partial differential equation due to the dependency of  $x$  on both space and time.

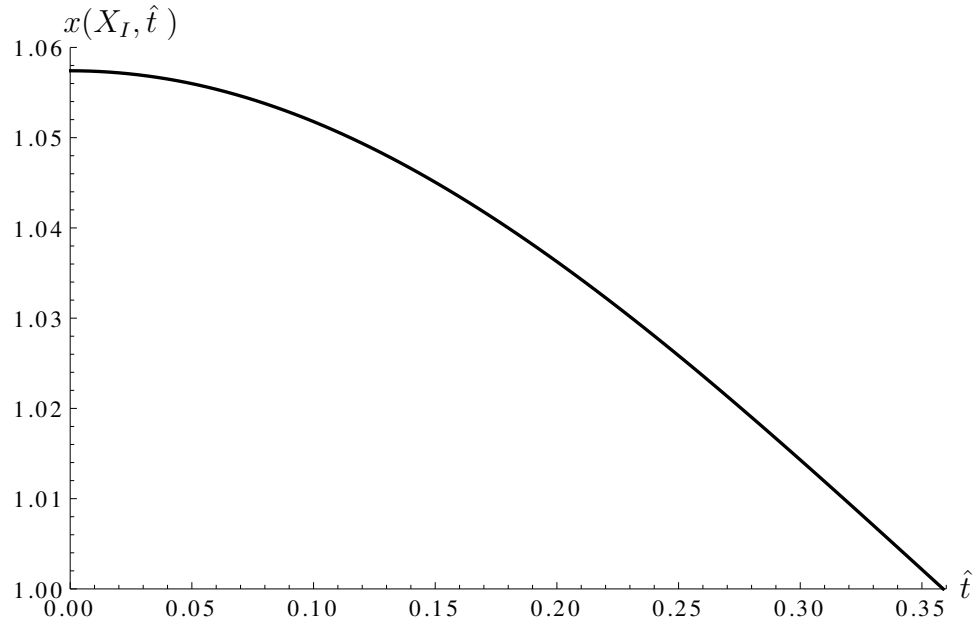


Figure 28: Collapse of the nondimensionalised inner radius versus the nondimensionalised time for an initial configuration with stress free boundary conditions, where  $X_O = 1.02$ ,  $\nu = 0.48$  and  $\hat{p} = 0.01$ . This is calculated using equations (190),(191) and (192).

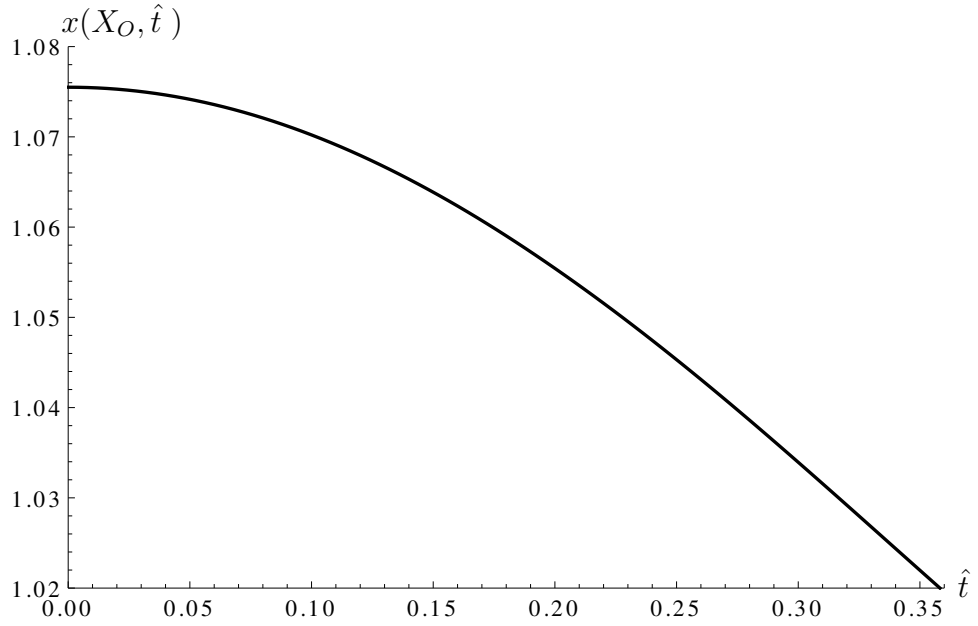


Figure 29: Collapse of the nondimensionalised outer radius versus the nondimensionalised time for  $X_O = 1.02$ ,  $\nu = 0.48$  and  $\hat{p} = 0.01$ . This is calculated using equations (190),(191) and (192).

Figures 28 and 29 show the collapse times for the inner and outer radii of a shelled microbubble with a reference thickness of  $X_O - X_I = 0.02$ . The time evolution of the thickness of the shell is nonlinear in behaviour. The stress free configuration is achieved when  $(-\partial\hat{\tau}_{xx}/\partial x) + (2/x)(\hat{\tau}_{xx} - \hat{\tau}_{\theta\theta}) = 0$  which coincides with  $x(X_I, \hat{t}) = 1$  as illustrated in Figure 28 . The outer radius collapses to its original stress free configuration of  $x(X_O, \hat{t}) = 1.02$  in the same time scale as the inner radius. The collapse phase of the inner and outer radii is sinusoidal in nature with both Figures 28 and 29 representing a section of a cosine waveform which is characteristic of simple harmonic motion. This switching off of the stress load at the inner shell which results in the collapse of the shell produces SHM with the shell oscillating about its equilibrium inner and outer radii. Extending the plots beyond the stress free configuration's location results in a continuous cosine waveform with a consistent maximum amplitude thus implying that the measured

collapse time is effectively 1/4 of a period of oscillation of the shell. At the collapse time, the total stress acting on the shell is zero which indicates a zero acceleration which is consistent with SHM. The maximum amplitude never diminishes since there are no viscoelastic or dissipative forces in the system which would reduce the maximum potential energy of the stressed shell. The collapse time's spatial location is the centre of oscillation of the shell and represents the point where the oscillating shell has a zero acceleration but a maximum velocity.

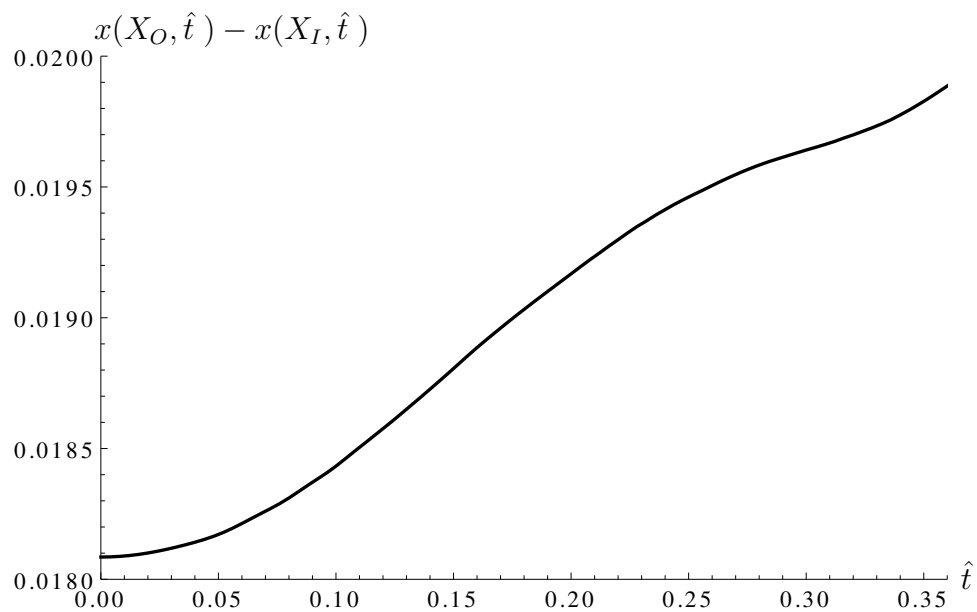


Figure 30: Collapse of the nondimensionalised shell's thickness versus the nondimensionalised time for  $X_O = 1.02$ ,  $\nu = 0.48$  and  $\hat{p} = 0.01$ . This is calculated using equations (190),(191) and (192).

Figure 30 illustrates the thickness of the shell as it evolves with time during the collapse phase of the shell and clearly highlights how the shell thickens up in a nonlinear manner as the shell collapses back to its stress free configuration (equilibrium position). The thickness of the shell at its stress free configuration does not exactly match its original thickness of  $X_O - X_I = 0.02$  possessing a 0.55% error. This slight difference in thickness will be investigated further to show that

the effects are due to rounding and discretization errors in the numerical scheme.

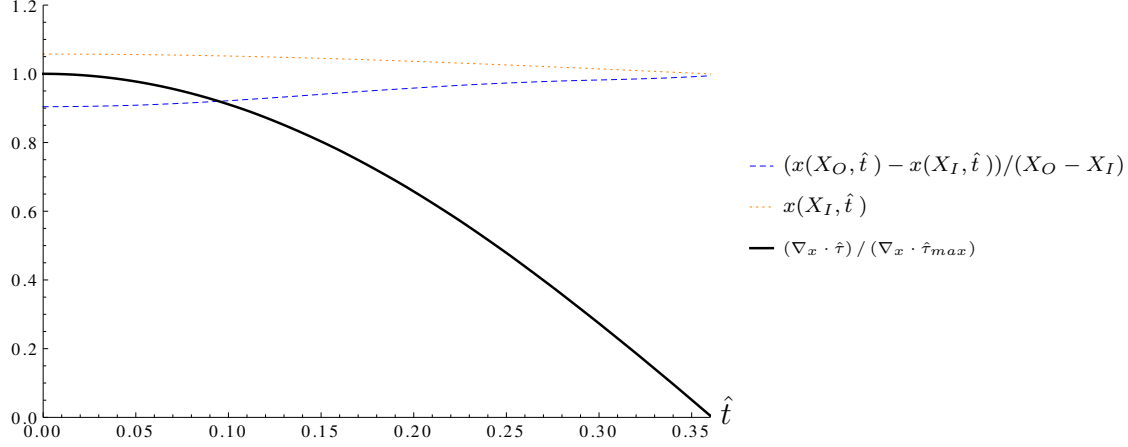


Figure 31: Comparison of the normalised, nondimensionalised shell's inner radius, thickness and  $\nabla_x \cdot \tau$  versus the nondimensionalised time for  $x(X_O, \hat{t}) - x(X_I, \hat{t}) = 0.02$ ,  $\nu = 0.48$  and  $\hat{p} = 0.01$ . This is calculated using equations (190),(191) and (192).

Figure 31 illustrates the behaviour of  $\nabla_x \cdot \hat{\tau} / \nabla_x \cdot \hat{\tau}_{max}$ ,  $x(X_I, \hat{t})$  and  $x(X_O, \hat{t}) - x(X_I, \hat{t})$  during the collapse phase. The shell collapses to its stress free configuration defined by the normalised form of  $\nabla_x \cdot \tau = 0$ , which is represented by the solid curve in Figure 31, in a nondimensionalised time of  $\hat{t}^* \approx 0.36$  which coincides with the inner radius  $x(X_I, \hat{t}) = 1$  shown in Figure 31. Note that  $\nabla_x \cdot \hat{\tau} = 0$  is normalised by dividing it by  $\nabla_x \cdot \hat{\tau}_{max}$ . The collapse thickness  $x(X_O, \hat{t}) - x(X_I, \hat{t})$  is normalised by dividing it by its original thickness  $X_O - X_I$ . The stress free configuration is defined as occurring when  $\nabla_x \cdot \hat{\tau} / \nabla_x \cdot \hat{\tau}_{max} = 0$ . This coincides with the inner radius obtaining a value of  $x(X_I, \hat{t}) = 1$ . Figure 31 illustrates that this condition is satisfied. However, the final thickness falls slightly short of its original stress free configuration's value.



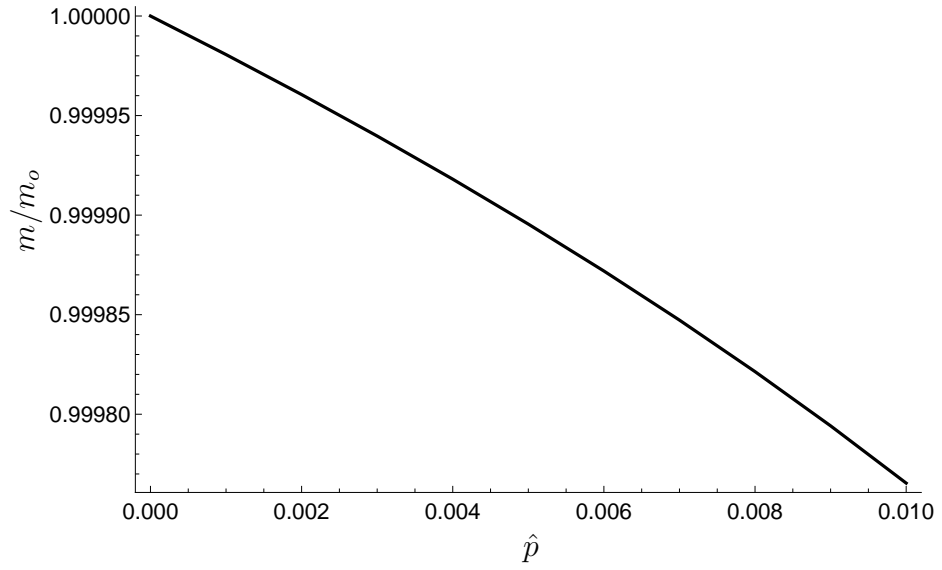


Figure 32: The normalised mass of the shell versus the inflationary stress for  $X_O = 1.02$  and  $\nu = 0.48$ . This is calculated using equations (190),(191) and (192), the volume =  $4/3\pi (x(X_O, \hat{t})^3 - x(X_I, \hat{t})^3)$ ,  $\rho = \rho_o/J$ , where  $J = x'x^2/X^2$  and mass =  $\rho \times$  volume.

Figure 32 illustrates the mass of a shelled microbubble (normalised with respect to the mass of the stress free shell) versus the nondimensionalised inflationary stress  $\hat{p}$ . The mass of the shell should of course remain constant due to the conservation of mass. Figure 32 confirms this and shows that it is effectively constant with a maximum error of 0.023%.

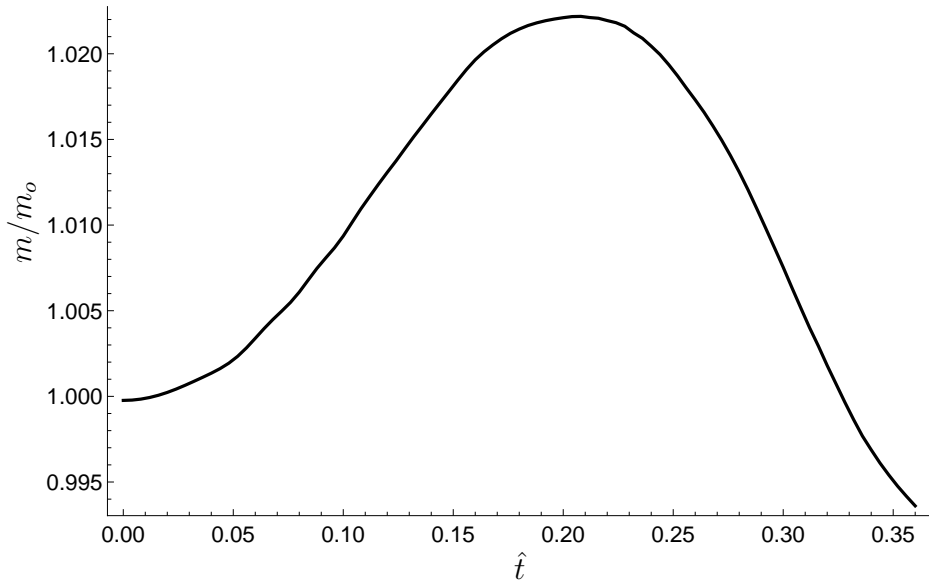


Figure 33: The normalised mass of the shell during the collapse phase versus time for  $X_O = 1.02$ ,  $\nu = 0.48$  and  $\hat{p} = 0.01$ . This is calculated using equations (190),(191) and (192), the volume =  $4/3\pi (x(X_O, \hat{t})^3 - x(X_I, \hat{t})^3)$ ,  $\rho = \rho_o/J$ , where  $J = x'x^2/X^2$  and mass =  $\rho \times$  volume.

Figure 33 plots the mass of a shelled microbubble (normalised with respect to the mass of a stress free shell) versus time as the shell collapses. The mass of the shell should once again be conserved during the collapse phase. Figure 33 highlights how the mass of the shell fluctuates slightly from the normalised value of one. The error in mass conservation at the stress free configuration's location is 0.6%. Explicit finite difference schemes possess both rounding and discretization errors in their solutions. The small deviation from the conservation of mass illustrated in Figure 33 is due to discretization and rounding errors and cannot be associated with hysteresis effects since the collapsing model does not possess any viscoelasticity.

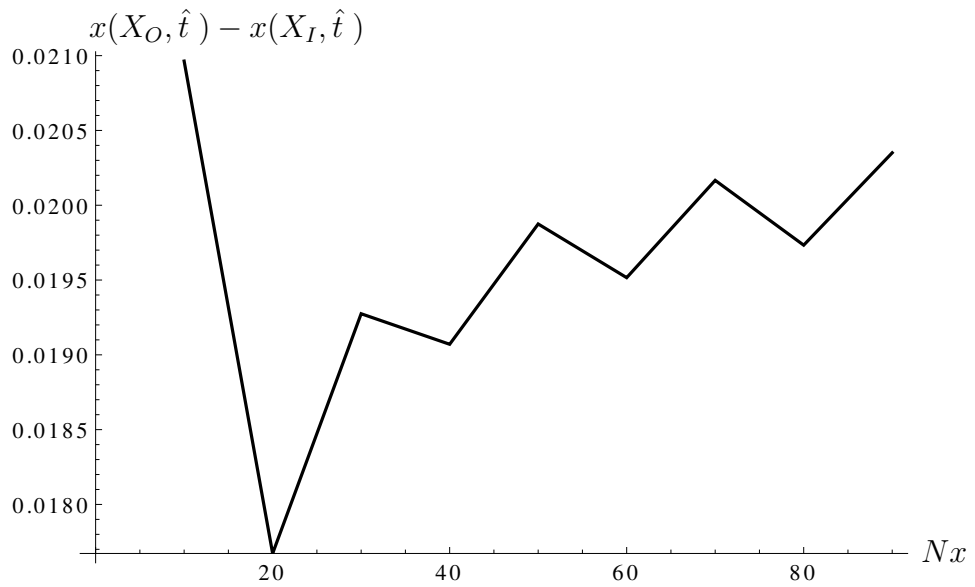


Figure 34: Collapse of the nondimensionalised shell's thickness versus the number of spatial steps  $Nx$  for  $X_O = 1.02$ ,  $\nu = 0.48$  and  $\hat{p} = 0.01$ . This is calculated using equations (190),(191) and (192).

Figure 34 illustrates the dependency of the final collapse thickness of the shelled microbubble on the number of spatial steps. As the number of discretized spatial steps increases the thickness converges to its initial stress free configuration value of  $x(X_O, \hat{t}) - x(X_I, \hat{t}) = 0.02$ .

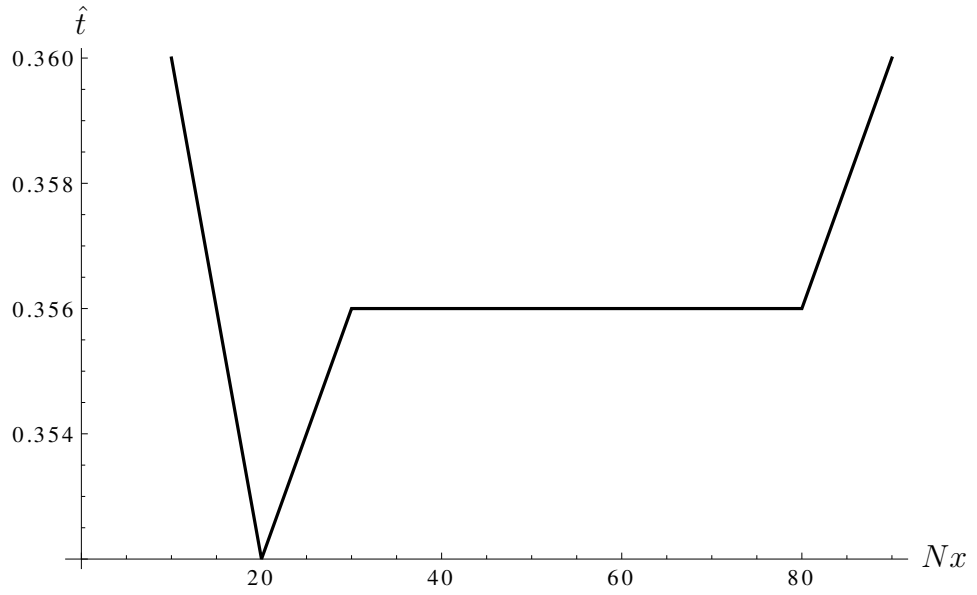


Figure 35: Nondimensionalised collapse time of the shell versus the number of spatial steps  $Nx$  for  $X_O = 1.02$ ,  $\nu = 0.48$  and  $\hat{p} = 0.01$ . This is calculated using equations (190),(191) and (192).

Figure 35 illustrates the dependency of the nondimensionalised collapse time (obtained when  $\text{div}_x \tau = 0$ ) as the number of discretized spatial steps is varied. As the number of discretized spatial steps increases the time converges but it can also be seen that there is very little variance ( $\approx 1\%$ ).

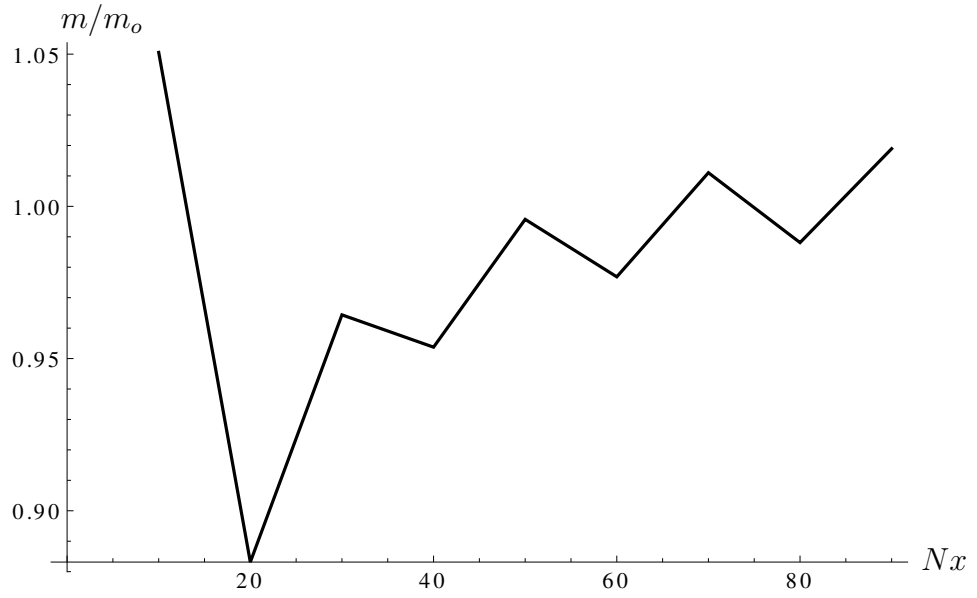


Figure 36: Normalised mass of the shell versus the number of spatial steps  $Nx$  for  $X_O = 1.02$ ,  $\nu = 0.48$  and  $\hat{p} = 0.01$ . This is calculated using equations (190),(191),(192),  $\text{volume} = 4/3\pi (x(X_O, \hat{t})^3 - x(X_I, \hat{t})^3)$ ,  $\rho = \rho_o/J$ , where  $J = x'x^2/X^2$  and  $\text{mass} = \rho \times \text{volume}$ .

Figure 36 illustrates how the normalised mass of the shell at the collapse stage (when  $\text{div}_x \tau = 0$ ) varies with the number of spatial steps  $Nx$ . The normalised mass is evaluated by dividing the mass of the shell at the collapse phase by its initial stress free mass. As the number of discretized spatial steps increases the normalised mass converges to one confirming that mass conservation is preserved.

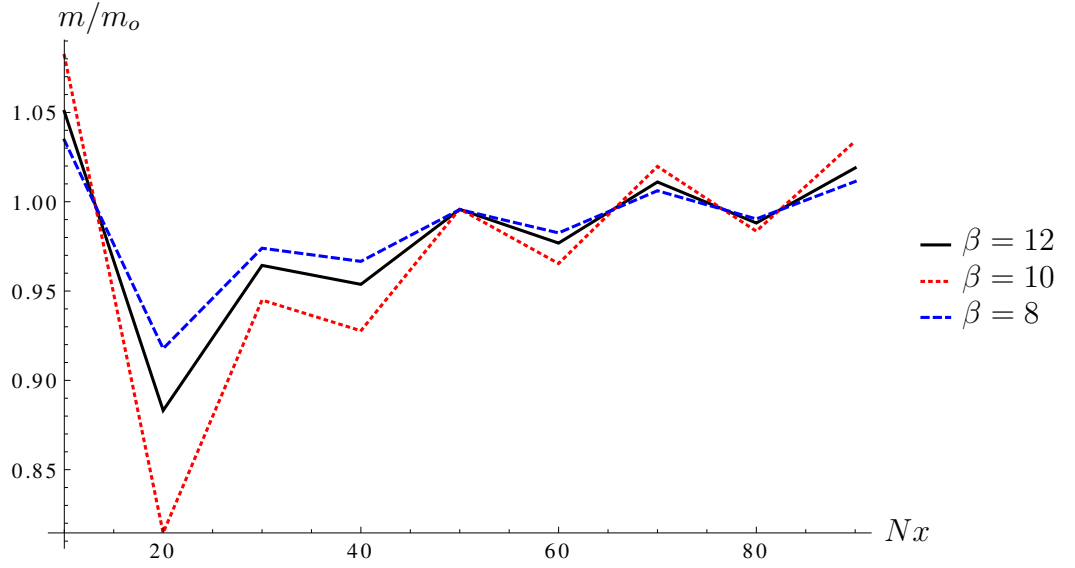


Figure 37: Normalised mass of the shell  $m/m_o$  versus the number of spatial steps  $Nx$  for various values of  $\beta$  with  $X_O = 1.02$ , and  $\hat{p} = 0.01$ . This is calculated using equations (190),(191) and (192), the volume =  $4/3\pi (x(X_O, \hat{t})^3 - x(X_I, \hat{t})^3)$ ,  $\rho = \rho_o/J$ , where  $J = x'x^2/X^2$  and mass =  $\rho \times$  volume.

Figure 37 illustrates how the normalised mass of the shell at the collapse stage (when  $\text{div}_x \tau = 0$ ) varies with the number of spatial steps  $Nx$  for a range of different values of  $\beta$ . As the number of discretized spatial steps increases the normalised mass converges to one. This supports the earlier statement that any difference between the initial stress free thickness and the final collapse thickness is due to discretization errors in the numerical scheme.

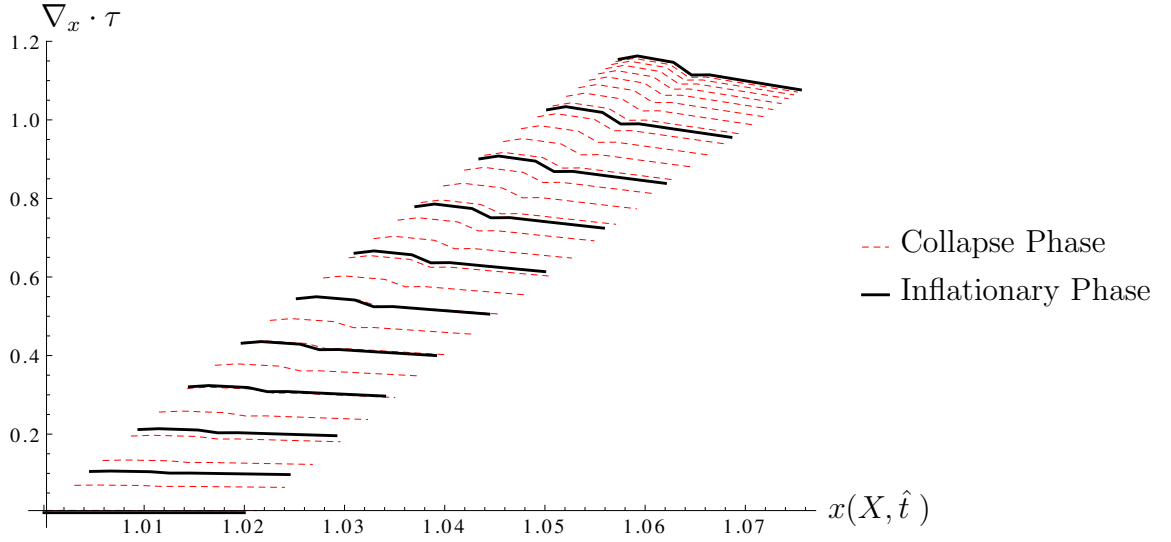


Figure 38: Graph of the divergence of the Cauchy stress versus the nondimensionalised radial displacement for the inflationary and collapse phases of the shell. The maximum stress is  $\hat{p} = 0.01$  with  $\nu = 0.48$  and an initial shell thickness of  $x(X_O, \hat{t}) - x(X_I, \hat{t}) = 0.02$ .

Figure 38 illustrates both the inflationary and collapse states of the shell. The stressed shell collapses to the stress free configuration when the total stress in the shell is zero ( $\nabla_x \cdot \tau = 0$ ). Figure 38 highlights that the inner radius for the collapsing shell coincides with the initial stress free inner radius. However, the outer radius for the collapsing shell is very slightly larger than the initial outer radius at the stress free configuration. The outer radius at this point exceeds its initial value (by a small amount) emphasising that the final thickness is greater than the initial, stress free configuration's thickness. Figure 38 shows that the collapse path for the shell is slightly different from its initial inflationary path.

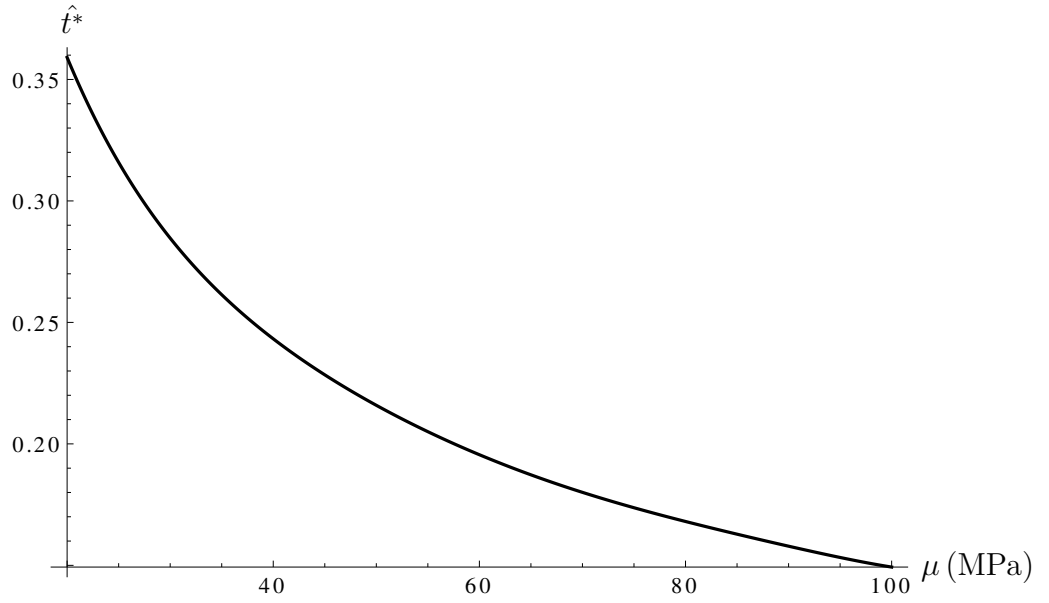


Figure 39: Graph of the nondimensionalised collapse time ( $\hat{t}^*$ ) versus the shear modulus for  $X_O = 1.02$  and  $\nu = 0.48$ . This is calculated using equations (190),(191) and (192).

Figure 39 illustrates how the nondimensionalised collapse time for a stressed shell varies with the shear modulus. The same magnitude of stress  $p$  is applied which results in different  $\hat{p}$  values as  $\mu$  changes. A larger shear modulus implies that the shell is stiffer and so will not strain as much for a particular stress value. This results in a smaller radial displacement when inflated. The smaller initial radial displacement means that the shell takes a shorter time to collapse down to its original stress free configuration. Therefore, as the shear modulus value increases there should be a reduction in the collapse time and this nonlinear behaviour is illustrated in Figure 39.



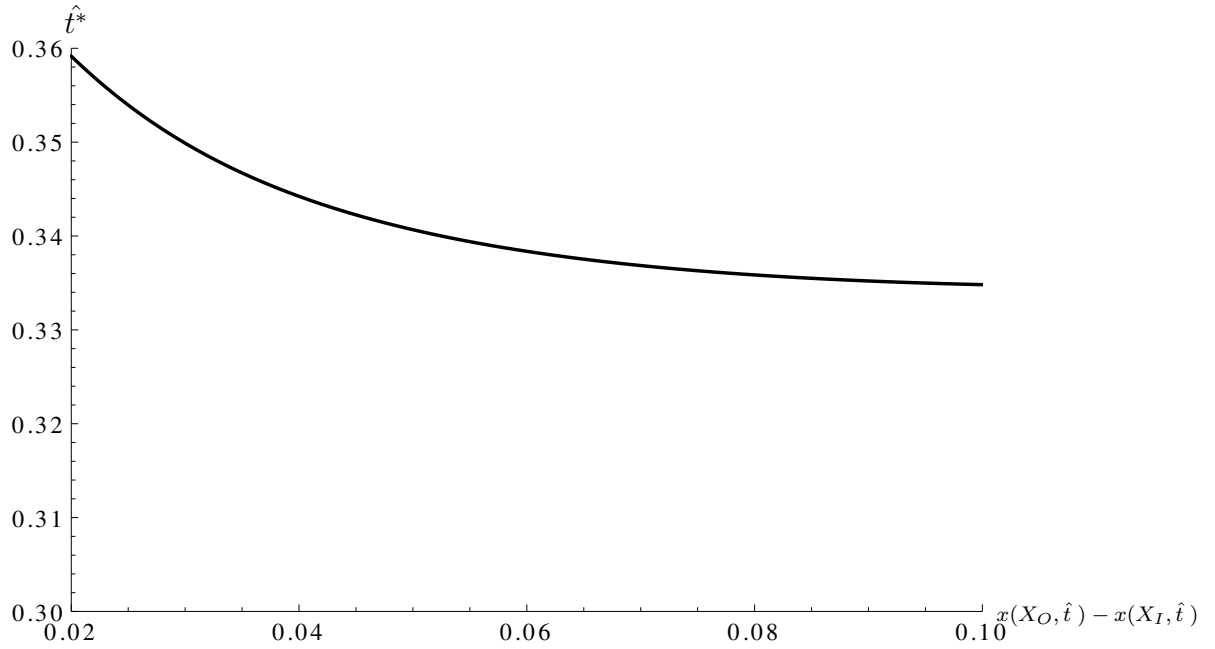


Figure 40: Graph of the nondimensionalised collapse time versus the nondimensionalised shell thickness for  $X_O = 1.02$ ,  $\nu = 0.48$ ,  $\mu = 20\text{MPa}$  and  $\hat{p} = 0.01$ . This is calculated using equations (190),(191) and (192).

Figure 40 illustrates how the nondimensionalised collapse time varies against the nondimensionalised thickness of the shell. Thin shells will experience a larger strain which will result in a greater radial displacement for a particular stress load. A greater radial displacement means that the collapse time will increase. Increasing the thickness of the shell will therefore result in a reduction in the collapse time of the shelled microbubble. This trend is illustrated in Figure 40. Notice that the trend is nonlinear and that the variation in collapse time is not that significant given the range of the thickness of shells that are considered in this particular study.

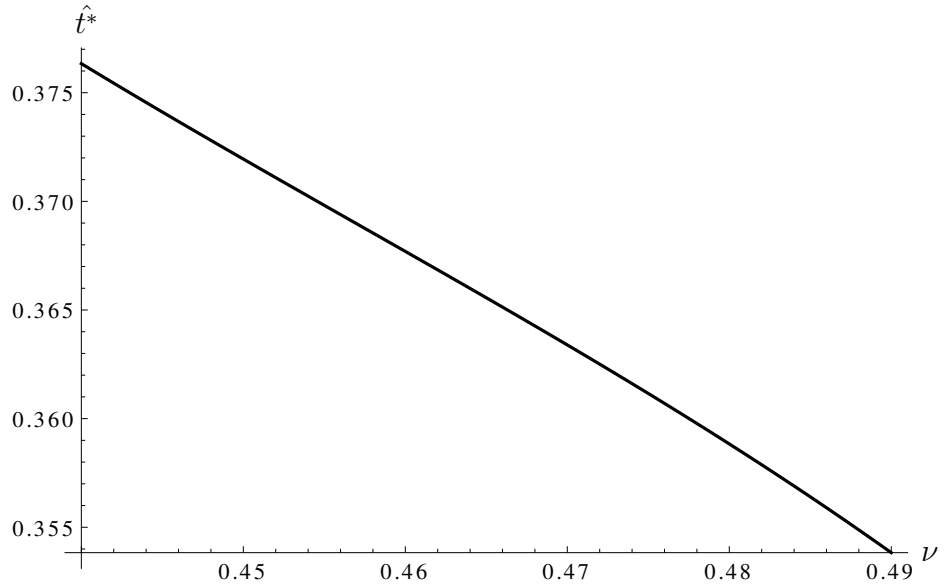


Figure 41: Graph of the nondimensionalised collapse time versus Poisson's ratio for  $X_O = 1.02$ ,  $\mu = 20\text{MPa}$  and  $\hat{p} = 0.01$ . This is calculated using equations (190),(191) and (192).

Figure 41 highlights the linear relationship between the nondimensionalised collapse time and the shell's Poisson ratio for an applied stress of  $\hat{p} = 0.01$ . Poisson's ratio dictates how the material strains in the axial direction relate to the strain in the transverse direction [35]. The smaller Poisson ratios therefore result in a larger radial displacement for a given stress which then results in a longer collapse time. Figure 41 confirms this but again it can be seen that there is very little change in the collapse time.

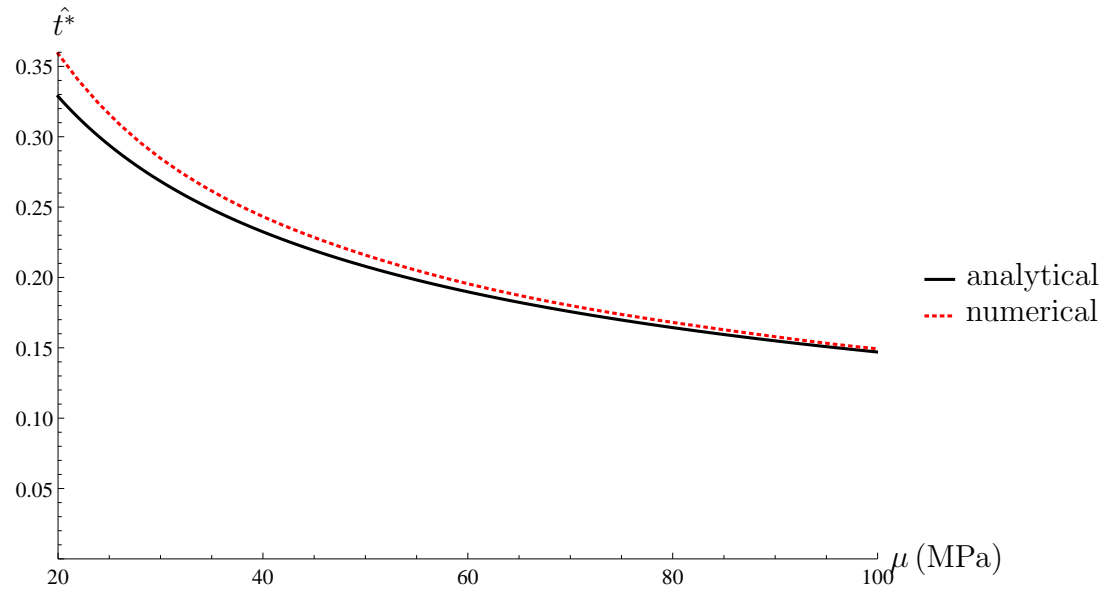


Figure 42: Graph comparing the analytical and numerical approaches for the nondimensionalised collapse time versus the shear modulus with  $X_O = 1.02$  and  $\nu = 0.48$ .

Figure 42 compares the relationship between the collapse time of the shell and its shear modulus value  $\mu$  for both the numerical and analytical approaches for the same initial stress value. There is a nonlinear relationship between the collapse time of the shell and its shear modulus with larger shear modulus values displaying faster collapse times. Note that the analytical approach possesses slightly faster collapse times than the numerical technique but exhibits the same characteristic trend. These faster collapse times are due to the analytical scheme adopting the approach of linearisation which results in the removal of various nonlinear higher order terms.

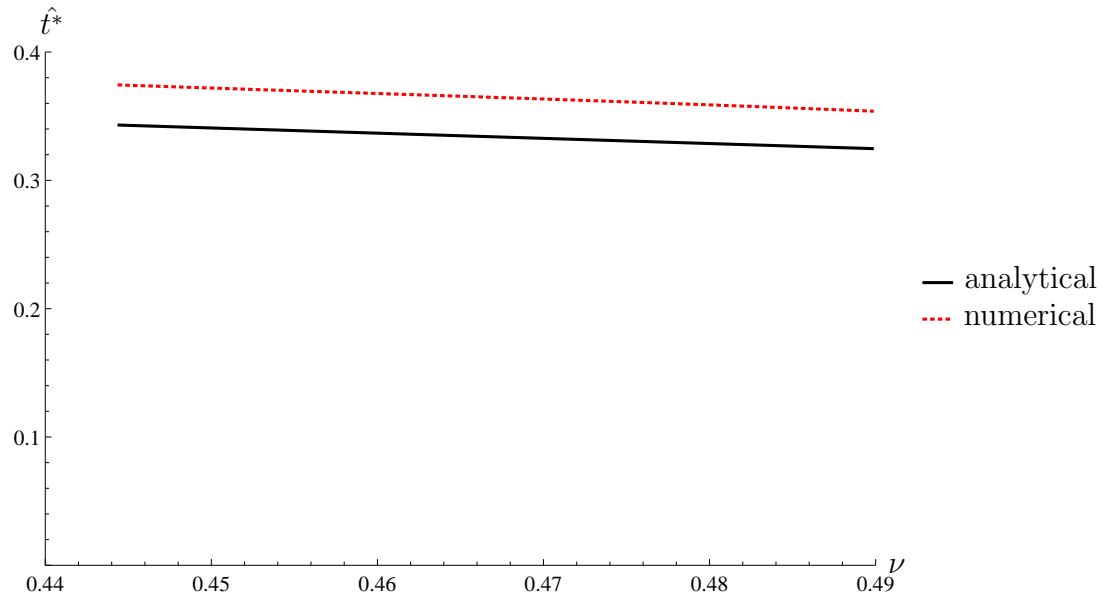


Figure 43: Graph comparing the analytical and numerical approaches for the nondimensionalised collapse time versus the Poisson ratio with  $X_O = 1.02$ ,  $\mu = 20\text{MPa}$  and  $\hat{p} = 0.01$ .

Figure 43 highlights the linear relationship between the Poisson ratio and the collapse time of the shell for both the analytical and numerical approaches. Both techniques display the same characteristic behaviour with faster collapse times for increasing Poisson ratios but the analytical approach displays quicker collapse times. The Poisson ratio is varied over a limited range of values that are typical for UCA protein polymers [44].

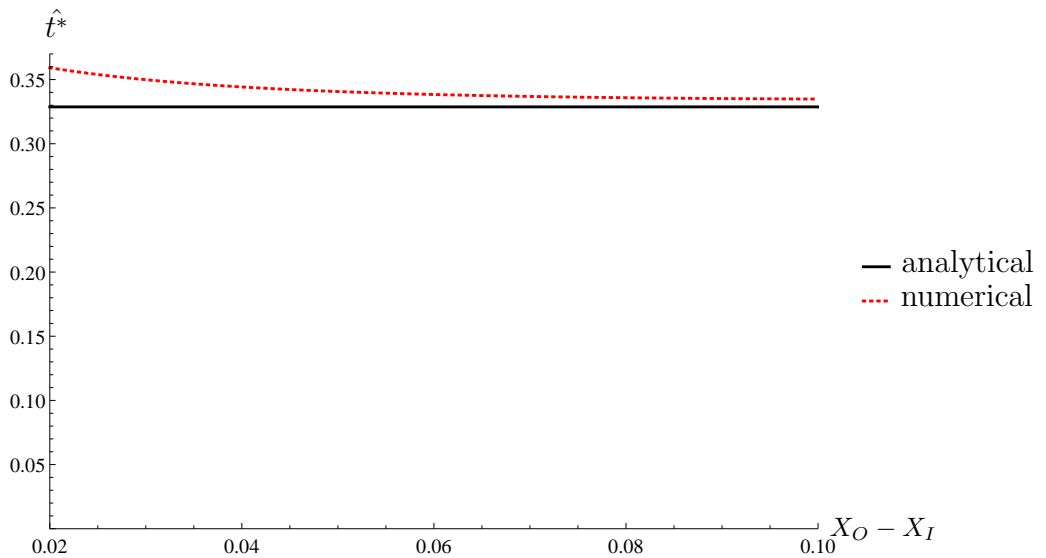


Figure 44: Graph comparing the analytical and numerical approaches for the nondimensionalised collapse time versus the initial thickness of the shell with  $\mu = 20\text{MPa}$ ,  $\nu = 0.48$  and  $\hat{p} = 0.01$ .

Figure 44 illustrates the nonlinear relationship between the shell's original, stress free thickness and its collapse time. The collapse time of the shell is faster as the thickness increases with the analytical approximation exhibiting a very small variation in collapse times compared to the numerical scheme. The convective derivative in the momentum is a second order term that possesses a spatial derivative and links the Lagrangean frame to the Eulerian picture. The removal of the convective derivative that occurs in the linearisation influences the physical behaviour of the shell particularly in the scenario where there is a variation associated with length scale (such as varying the thickness of the shell) since there is no longer a term which possesses a derivative with respect to the spatial parameter  $x(X, \hat{t})$ . Removing the convective derivative also has implications for mass conservation thus limiting the use of asymptotic expansion.

## 13 Experimental v theoretical results

This section compares the theoretical model with the published experimental results. The Müller experiment [50] illustrates how the collapsing shelled millibubble's displacement varies linearly with time. This linear relationship allows us to extrapolate Müller's experimental results and also supports the use of linearisation for the analytical model in Chapter 2. The theoretical model was compared to the Müller experiment [50] with a shear modulus of  $\mu = 20\text{MPa}$  and a density  $\rho = 1100\text{kgm}^{-3}$  [44]. A 4.5mm stressed ( $\hat{p} = 0.0002$ ) shelled millibubble of thickness 1460nm with a Poisson ratio of  $\nu = 0.48$  has a theoretical collapse time of  $t^* = 1.1 \times 10^{-5}\text{s}$  with an experimental collapse time from Müller of  $t^* = 4.9 \times 10^{-5}\text{s}$ . There are several reasons as to why the theoretical model's collapse time differs from the experimentally observed value. The theoretical model has no viscoelastic characteristics; there is no damping term in the model which could account for the effect of viscosity acting on the shell. In the model there are no external loads on the shell as it collapses whereas in the experiment the surrounding air will affect the collapsing shell dynamics. The theoretical model preserves the spherical topology of the shelled millibubble as it collapses; there are no ripping or tearing effects. The material parameters used for the theoretical model may not exactly match the experimental values in [50]. For example the experimental values for the shear modulus and the Poisson ratio were not measured and so were estimated [44]. The experimental results will also have errors associated with the measurements in the thickness of the shell and in the measurement of the collapse time. The strain energy density function used in this study may not accurately describe the smectic A dynamics.

## 13.1 Conclusion

A neo-Hookean strain energy density function has been used to derive a nonlinear elasticity model of a stressed shelled microbubble. The shelled microbubble was stressed by applying a radial stress load to the inner surface of an initially stress free shelled microbubble. The shell was then collapsed from its stressed configuration to its stress free configuration. Finite differences were used to solve numerically the model and derive the collapse times for the shell. The material parameters were then varied to assess their effects on this collapse time. Spatial profiles for the Cauchy radial and hoop stresses were constructed for the inflationary phase of the shell. A series of plots were constructed illustrating the collapse phase of the stressed shell's inner radius, outer radius and the shell's thickness versus time. A typical shell subjected to a nondimensionalised stress of  $\hat{p} = 0.01$  with a Poisson ratio of  $\nu = 0.48$  has a nondimensionalised collapse time of  $\hat{t}^* \approx 0.36$ . The analytical approach exploits an asymptotic expansion approximation exhibits slightly faster collapse times. This study considered the influence of varying the shear modulus and the shell thickness on the collapse phase of a shelled microbubble and it was found that the collapse time decreases significantly with increasing shear modulus. Thicker shells displayed a relatively consistent collapse time.

## References

- [1] P. Narayan and M. A. Wheatley. Preparation and characterization of hollow microcapsules for use as ultrasound contrast agents. *Polymer Engineering and Science*, 39:2242–2255, 1999.
- [2] M. Bazan Peregrino, B. Rifai, R. C. Carlisle, J. Choi, C. D. Arvanitis, L. W. Seymour, and C. C. Coussios. Cavitation-enhanced delivery of a replicating

- oncolytic adenovirus to tumors using focused ultrasound. *Journal of Controlled Release*, 169:40–47, 2013.
- [3] D. Gourevich, A. Volovick, O. Dogadkin, L. Wang, H. Mulvana, Y. Medan, A. Melzer, and S. Cochran. In vitro investigation of the individual contributions of ultrasound-induced stable and inertial cavitation in targeted drug delivery. *Ultrasound in Medicine & Biology*, 41:1853–1864, 2015.
- [4] J.M. Escoffre, C. Mannaris, B. Geers, A. Novell, I. Lentacker, M. Averkion, and A. Bouakaz. Doxorubicin liposome-loaded microbubbles for contrast imaging and ultrasound triggered drug delivery. *IEEE Transactions on Ultrasonics, Ferroelectrics and frequency control*, 60:78–87, 2013.
- [5] Ching-Hsiang Fan, Chien-Yu Ting, Hao-Li Liu, Chiung-Yin Huang, Han-Yi Hsieh, Tzu-Chen Yen, Kuo-Chen Wei, and Chih-Kuang Yeh. Antiangiogenic-targeting drug-loaded microbubbles combined with focused ultrasound for glioma treatment. *Biomaterials*, 34:2142–2155, 2013.
- [6] F. Yan, L. Li, Z. Deng, Q. Jin, J. Chen, W. Yang, C. K. Yeh, J. Wu, R. Shandas, X. Liu, and H. Zheng. Paclitaxel-liposome-microbubble complexes as ultrasound-triggered therapeutic drug delivery carriers. *Journal of Controlled Release*, 166:246–255, 2013.
- [7] C. Niu, Z. Wang, G. Lu, T. M. Krupka, Y. Sun, Y. You, W. Song, H. Ran, P. Li, and Y. Zheng. Doxorubicin loaded superparamagnetic PLGA-iron oxide multifunctional microbubbles for dual-mode US/MR imaging and therapy of metastasis in lymph nodes. *Biomaterials*, 34:2307–2317, 2013.



- [8] E. Stride and N. Saffari. Microbubble ultrasound contrast agents: a review. *Proceedings of the Institution of Mechanical Engineers Part H*, 217:429–447, 2003.
- [9] D. Cosgrove. Ultrasound contrast agents: An overview. *European Journal of Radiology*, 60:324–330, 2006.
- [10] E. Stride and C. C. Coussios. Cavitation and contrast: The use of bubbles in ultrasound imaging and therapy. *Proceedings of the Institute of Mechanical Engineers Part H*, 224:171–191, 2010.
- [11] J. McLaughlan, N. Ingram, P.R. Smith, S. Harput, P.L. Coletta, S. Evans, and S. Freear. Increasing the sonoporation efficiency of targeted polydisperse microbubble populations using chirp excitation. *IEEE Transactions on ultrasonics, Ferroelectrics and frequency control*, 60:2511–2520, 2013.
- [12] O. Falou, A.J. Sojahrood, J.C. Kumaradas, and M.C. Kolios. Modelling the effect of shell thickness on high frequency ultrasound scattering from ultrasound contrast agents. *Canadian Acoustics*, 38:38–39, 2010.
- [13] G. A. Sotiriou, F. Starsich, A. Dasargyri, M. C. Wurnig, F. Krumeich, A. Boss, Jean-Christophe Leroux, and S. E. Pratsinis. Photothermal killing of cancer cells by the controlled plasmonic coupling of Silica-coated Au/Fe<sub>2</sub>O<sub>3</sub> nanoaggregates. *Advanced Functional Materials*, 24:2818–2827, 2014.
- [14] M.J.K. Blomley, J.C. Cooke, E.C. Unger, M.J. Monaghan, and D.O. Cosgrove. Microbubble contrast agents: a new era in ultrasound. *British Medical Journal*, 322:1222–1225, 2001.
- [15] I. Lentacker, S. C. De Smedt, and N. N. Sanders. Drug loaded microbubble design for ultrasound triggered delivery. *Soft Matter*, 5:2161–2170, 2009.

- [16] P.A. Dijkmans, L.J.M. Juffermans, R.J.P. Musters, A. Van Wamel, F.J. ten Cate, W. van Gilst, C.A. Visser, N. de Jong, and O. Kamp. Microbubbles and ultrasound: from diagnosis to therapy. *European Journal of Echocardiography*, 5:245–256, 2004.
- [17] M. Cochran, T. Bustamante, J. Eisenbrey, and M. Wheatley. In vitro characterization of docetaxel loaded microbubbles for ultrasound triggered drug delivery. *Pharmaceutical Engineering*, 32:1–10, 2012.
- [18] J. McLaughlan, P. Smith, N. Ingram, L. Coletta, S. Evans, and S. Freear. Chirp excitation of polydisperse microbubble populations for increasing sonoporation efficiency. *IEEE International Symposium Proceedings of Ultrasonics*, pages 2298–2301, 2012.
- [19] G. A. Sotiriou, F. Starsich, A. Dasargyri, M. C. Wurnig, F. Krumeich, A. Boss, Jean-Christophe Leroux, and S. E. Pratsinis. Photothermal killing of cancer cells by the controlled plasmonic coupling of Silica-coated Au/Fe<sub>2</sub>O<sub>3</sub> nanoaggregates. *Advanced Functional Materials*, 24:2818–2827, 2014.
- [20] A.A. Doinikov and A. Bouakaz. Theoretical investigation of shear stress generated by a contrast microbubble on the cell membrane as a mechanism for sonoporation. *Journal Acoustical Society of America*, 128:11–19, 2010.
- [21] A.A. Doinikov, L. Aired, and A. Bouakaz. Dynamics of a contrast agent microbubble attached to an elastic wall. *IEEE Transactions on Medical Imaging*, 31:654–662, 2012.
- [22] J. Wu. Shear stress in cells generated by ultrasound. *Progress in Biophysics and Molecular Biology*, 93:363–373, 2007.

- [23] P. Prentice, A. Cuschieri, K. Dholakia, M. Prausnitz, and P. Campbell. Membrane disruption by optically controlled microbubble cavitation. *Nat. Phys.*, 1:107–110, 2005.
- [24] K. Kooiman, M. Foppen-Harteveld, A.F.W. van der Steen, and N. de Jong. Sonoporation of endothelial cells by vibrating targeted microbubbles. *Journal of Controlled Release*, 154:35–41, 2011.
- [25] H. Dewitte, K. Vanderperren, H. Haers, E. Stock, L. Duchateau, M. Hesta, J. H. Saunders, S. C. De Smedt, and I. Lentacker. Theranostic mrna-loaded microbubbles in the lymphatics of dogs: implications for drug delivery. *Theranostics*, 5:97–109, 2015.
- [26] Ching-Hsiang Fan, Chien-Yu Ting, Hao-Li Liu, Chiung-Yin Huang, Han-Yi Hsieh, Tzu-Chen Yen, Kuo-Chen Wei, and Chih-Kuang Yeh. Antiangiogenic-targeting drug-loaded microbubbles combined with focused ultrasound for glioma treatment. *Biomaterials*, 34:2142–2155, 2013.
- [27] Lord Rayleigh. On the pressure developed in a liquid during the collapse of a spherical bubble. *Philosophical Magazine, Series 6*, 34:94–98, 1917.
- [28] M.S. Plesset. The dynamics of cavitation bubbles. *ASME Journal of Applied Mechanics*, 16:277–282, 1949.
- [29] A.A. Doinikov and A. Bouakaz. Review of shell models for contrast agent microbubbles. *IEEE Transactions on Ultrasonics, Ferroelectrics and Frequency Control*, 58:981–993, 2011.
- [30] P. Marmottant, S. Van der Meer, M. Emmer, M. Versluis, N. de Jong, S. Hilgenfeldt, and D. Lohse. A model for large amplitude oscillations of

- coated bubbles accounting for buckling and rupture. *Journal Acoustical Society of America*, 118:3499–3505, 2005.
- [31] S. Paul, A. Katiyar, K. Sarkar, D. Chatterjee, W.T. Shi, and F. Forsberg. Material characterization of the encapsulation of an ultrasound contrast microbubble and its subharmonic response: Strain-softening interfacial elasticity model. *Journal Acoustical Society of America*, 127:3846–3857, 2010.
- [32] C.C. Church. The effects of an elastic solid surface layer on the radial pulsations of gas bubbles. *Journal Acoustical Society of America*, 97:1510–1521, 1995.
- [33] A.A. Doinikov and P.A. Dayton. Maxwell rheological model for lipid-shelled ultrasound microbubble contrast agents. *Journal Acoustical Society of America*, 121:3331–3340, 2007.
- [34] A.A. Doinikov, J.F. Haac, and P.A. Dayton. Modeling of nonlinear viscous stress in encapsulating shells of lipid-coated contrast agent microbubbles. *Ultrasonics*, 49:269–275, 2009.
- [35] Y. Gorb and J.R. Walton. Dependence of the frequency spectrum of small amplitude vibrations superimposed on finite deformations of a nonlinear, cylindrical elastic body on residual stress. *International Journal of Engineering Science*, 48:1289–1312, 2010.
- [36] Y. C. Fung. *Biomechanics: Motion, Flow, Stress and Growth*. Springer, New York, 1990.
- [37] Y. C. Fung. *Biomechanics: Mechanical Properties of Living Tissues*. Springer, New York, 1993.

- [38] Y. C. Fung. *Biomechanics*. Springer, New York, 1996.
- [39] G.A. Holzapfel. *Nonlinear Solid Mechanics*. Wiley, Wiltshire, 2000.
- [40] G. A. Holzapfel and R. W. Ogden. *Biomechanics of Soft Tissue in Cardiovascular Systems*. Springer, New York, 2004.
- [41] K.A. Lazopoulos and R.W. Ogden. Spherically symmetric solutions for a spherical shell in finite pseudo-elasticity. *European Journal of Mechanics - A/Solids*, 18:617–632, 1999.
- [42] K. Efthymiou, K. Tsiglifis, S. Serpetzi, and N. Pelekasis. Static and dynamic analysis of contrast agents-parameter estimates and the effect of constitutive law. *9th EUROMECH Fluid Mechanics Conference*, 2012.
- [43] K. Tsiglifis and N.A. Pelekasis. Nonlinear radial oscillations of encapsulated microbubbles subject to ultrasound: The effect of membrane constitutive law. *Journal Acoustical Society of America*, 123:4059–4070, 2008.
- [44] J. Tu, J. Guan, Y. Qiu, and T.J. Matula. Estimating the shell parameters of sonovue microbubbles using light scattering. *Journal Acoustical Society of America*, 126:2954–2962, 2009.
- [45] R.W. Ogden. *Nonlinear Elastic Deformations*. Dover, New York, 1997.
- [46] K. Gou, S. Joshi, and J.R. Walton. Recovery of material parameters of soft hyperelastic tissue by an inverse spectral technique. *International Journal of Engineering Science*, 56:1–16, 2012.
- [47] J.C. Daniel, A. Tongen, D.P. Warne, and P.G. Warne. A 3D nonlinear anisotropic spherical inflation model for intracranial saccular aneurysm elastodynamics. *Mathematics and Mechanics of Solids*, 15:279–307, 2010.

- [48] D. J. Acheson. *Elementary Fluid Dynamics*. Oxford University Press, New York, 1990.
- [49] Wolfram Research Inc. Mathematica. Version 9.0, 2012. Champaign, Illinois.
- [50] F. Müller and R. Stannarius. Comparison of the rupture dynamics of smectic bubbles and soap bubbles. *Liquid Crystals*, 36:133–145, 2009.